



FLOW ASSURANCE IN OFFSHORE PIPELINES: KINETIC AND
THERMODYNAMIC ASPECTS OF HYDRATE FORMATION AND DISSOCIATION
IN OIL-DOMINATED SYSTEMS

Tamires de Souza Alves da Silva

Dissertação de Mestrado apresentada ao Programa de Pós-graduação em Engenharia Química, COPPE, da Universidade Federal do Rio de Janeiro, como parte dos requisitos necessários à obtenção do título de Mestre em Engenharia Química.

Orientadores: Argimiro Resende Secchi
Príamo Albuquerque Melo Jr.

Rio de Janeiro
Fevereiro de 2023

FLOW ASSURANCE IN OFFSHORE PIPELINES: KINETIC AND
THERMODYNAMIC ASPECTS OF HYDRATE FORMATION AND DISSOCIATION
IN OIL-DOMINATED SYSTEMS

Tamires de Souza Alves da Silva

DISSERTAÇÃO SUBMETIDA AO CORPO DOCENTE DO INSTITUTO ALBERTO
LUIZ COIMBRA DE PÓS-GRADUAÇÃO E PESQUISA DE ENGENHARIA
DA UNIVERSIDADE FEDERAL DO RIO DE JANEIRO COMO PARTE DOS
REQUISITOS NECESSÁRIOS PARA A OBTENÇÃO DO GRAU DE MESTRE EM
CIÊNCIAS EM ENGENHARIA QUÍMICA.

Orientadores: Argimiro Resende Secchi
Príamo Albuquerque Melo Jr.

Aprovada por: Prof. Príamo Albuquerque Melo Jr.
Prof. Argimiro Resende Secchi
Prof. Frederico Wanderley Tavares
Prof. Luiz Augusto da Cruz Meleiro

RIO DE JANEIRO, RJ – BRASIL
FEVEREIRO DE 2023

de Souza Alves da Silva, Tamires

Flow assurance in offshore pipelines: kinetic and thermodynamic aspects of hydrate formation and dissociation in oil-dominated systems/Tamires de Souza Alves da Silva. – Rio de Janeiro: UFRJ/COPPE, 2023.

XX, 95 p.: il.; 29, 7cm.

Orientadores: Argimiro Resende Secchi

Príamo Albuquerque Melo Jr.

Dissertação (mestrado) – UFRJ/COPPE/Programa de Engenharia Química, 2023.

Referências Bibliográficas: p. 89 – 95.

1. gas hydrates. 2. multi-phase flow. 3. phase equilibria.
I. Resende Secchi, Argimiro *et al.* II. Universidade Federal do Rio de Janeiro, COPPE, Programa de Engenharia Química.
III. Título.

*Em memória de Filippe da Silva
Gonçalves*

Agradecimentos

Agradeço ao Programa de Engenharia Química da COPPE-UFRJ por ser meu lar nos últimos anos.

Em especial, agradeço aos professores Argimiro e Príamo por orientarem meu desenvolvimento pessoal e profissional. Todo o apoio e conselhos foram essenciais para que eu realizasse todos os meus sonhos e, agora, buscasse por novos desafios.

Eu agradeço aos meus amigos, Giovanna Ronzé, Daniel Tinôco, Neanderson Galvão, Many Cacau, Luelen Barbosa, Juliana Ronzé e Débora Miranda do projeto de extensão Bora Fazer Ciência, pelo companheirismo na luta de causas que valem a pena viver.

Por fim, agradeço a Deus e a minha família por serem a base para que eu chegasse até aqui.

Resumo da Dissertação apresentada à COPPE/UFRJ como parte dos requisitos necessários para a obtenção do grau de Mestre em Ciências (M.Sc.)

FLOW ASSURANCE IN OFFSHORE PIPELINES: KINETIC AND
THERMODYNAMIC ASPECTS OF HYDRATE FORMATION AND DISSOCIATION
IN OIL-DOMINATED SYSTEMS

Tamires de Souza Alves da Silva

Fevereiro/2023

Orientadores: Argimiro Resende Secchi

Príamo Albuquerque Melo Jr.

Programa: Engenharia Química

Os hidratos são um problema central na garantia de escoamento, pois esses sólidos podem se formar e bloquear tubulações mais rapidamente do que outros tipos de depósitos sólidos. As simulações computacionais combinam conhecimentos em modelagem de escoamento e caracterização de fluidos para desenvolver estratégias que garantam a taxa de produção e a segurança durante as operações. O modelo *Drift-Flux*, definido como um sistema de equações algébrico-diferenciais, foi utilizado para realizar simulações de escoamento multifásico em estado estacionário, em concordância com o conhecido simulador comercial *OLGA*[®]. O modelo de van der Waals e Platteuw e a simulação composicional obtiveram resultados que correspondem aos obtidos pelo software *Multiflash*TM para curvas de formação de hidratos e caracterização de fluidos. A inclusão da equação de conservação de hidratos e sua fração nas propriedades de mistura do fluido, utilizando o modelo *Drift-Flux*, permitiu observar a formação de hidratos na região do *riser*. Os modelos de agregação e dissociação previram comportamentos que estão em concordância com a literatura. Os resultados sugerem o potencial de desenvolvimento de uma ferramenta que efetue simulações para fins de garantia de escoamento, compreendendo aspectos termodinâmicos e cinéticos da formação e dissociação de hidratos em sistemas dominados por óleo sem a presença de inibidores.

Abstract of Dissertation presented to COPPE/UFRJ as a partial fulfillment of the requirements for the degree of Master of Science (M.Sc.)

FLOW ASSURANCE IN OFFSHORE PIPELINES: KINETIC AND
THERMODYNAMIC ASPECTS OF HYDRATE FORMATION AND DISSOCIATION
IN OIL-DOMINATED SYSTEMS

Tamires de Souza Alves da Silva

February/2023

Advisors: Argimiro Resende Secchi

Príamo Albuquerque Melo Jr.

Department: Chemical Engineering

Gas hydrates are a central issue in flow assurance because these solids can form and block pipes more quickly than other types of solid deposits. Computational simulations combine expertise in flow modeling and fluid characterization to develop strategies for ensuring optimal production rates and monitoring operations. The Drift-Flux Model, set as a differential-algebraic equations system, was used to perform steady-state multiphase flow simulations that were consistent with the well-known commercial simulator, *OLGA*[®]. The van der Waals and Platteeuw model, along with compositional simulation techniques, were used to obtain results for hydrate formation curves and fluid characterization that were consistent with those obtained from *Multiflash*TM software. By incorporating the hydrate conservative equation and fraction into the fluid mixture properties in the Drift-Flux Model, it was possible to observe crystal formation in the riser section. The aggregation and dissociation models predicted behaviors that were consistent with the literature. These results suggest the potential to develop a flow assurance simulating tool that includes the thermodynamic and kinetic aspects of hydrate formation and dissociation in oil-dominated systems without inhibitors.

Contents

List of Figures	x
List of Tables	xv
List of Symbols	xvii
List of Abbreviations	xix
1 Introduction	1
1.1 General motivations	2
1.2 Objectives and contribution	3
1.3 Structure of the text	4
2 Gas hydrates in the O&G industry	5
2.1 Gas hydrates characteristics	7
2.1.1 Hydrate structure	7
2.1.2 Guest molecules in natural gas	9
2.2 Thermodynamics of gas hydrates	10
2.2.1 Hydrates equilibrium curves	11
2.3 Kinetics of gas hydrates	16
2.3.1 Oil-dominated systems	17
2.3.2 Water properties and hydrate formation	19
2.3.3 Nucleation	20
2.3.4 Hydrate growth	21
2.3.5 Hydrate slurry	27
2.4 Multi-phase flow in pipelines	29
2.4.1 Multi-phase flow models	29
2.4.2 Hydrodynamic models with hydrates	34
2.5 Fluid characterization	37
2.5.1 Three-phase flash calculations	37

3	Methodology	43
3.1	Thermodynamic aspects	43
3.1.1	Methodology for calculating hydrate stability curve	43
3.1.2	Methodology for calculating fluid properties	46
3.1.3	Case studies for hydrate stability curve	47
3.1.4	Case study for fluid properties	49
3.2	Kinetic aspects	51
3.2.1	Modifications to include hydrates in the DFM	51
3.2.2	DAE system used in DASSLC	53
3.2.3	Modification in gas consumption equation	55
3.2.4	Hydrates properties	56
3.2.5	Agglomeration model	57
3.2.6	Flow regimes	58
3.2.7	Case studies for kinetics of hydrate formation	59
4	Result and discussion	62
4.1	Case Study 1	62
4.2	Case Study 2	63
4.3	Case Study 3	69
4.4	Case Study 4	75
4.5	Case Study 5	79
5	Conclusion	83
A	vdW-P model parameters	84
B	Complementary equations	85
B.1	Frictional loss	85
B.2	Phase velocities	86
C	Modified fluid complementary data	87
	References	89

List of Figures

1.1	Schematic representation of the steps involved in predicting hydrate formation and dissociation in pipelines. The highlighted box emphasizes the contribution of this work to the continued research aimed at improving the understanding of multi-phase flow in production pipelines.	3
2.1	Flow assurance techniques commonly employed in strategies for gas hydrate control. The gray boxes separate the techniques according to their application in hydrate prevention, management, and remediation. Adapted from KINNARI <i>et al.</i> (2014).	6
2.2	Phase diagrams of two-component systems, showing (a) methane–water or nitrogen–water system, a phase diagram with one quadruple point (Q_1) and (b) hydrocarbon–water system, which presents an upper quadruple point (Q_2). The diagrams illustrate the following phases: ice (I), liquid (L_W for water and L_{HC} for hydrocarbon), vapor (V), and hydrate (H), as well as their equilibria. The intersection points between the lines represent quadruple points (Q_1 and Q_2) where four phases coexist. Adapted from SLOAN e KOH (2008).	11
2.3	Operational conditions of subsea pipelines and hydrate stability regions. The solid gray line represents pipeline operational conditions from a deepwater wellhead to the processing facility. The shaded envelope indicates the hydrate stability curve. Each shaded curve represents the equilibrium conditions containing different amounts of thermodynamic hydrate inhibitors. Adapted from SLOAN e KOH (2008).	13
2.4	Schematic representation of hydrate formation in oil-dominated systems, including water droplet dispersion in the continuous oil phase, hydrate shell formation, followed by extensive agglomeration and plugging. Adapted from ZERPA <i>et al.</i> (2012).	18
2.5	Schematic representation of an oil-dominated system commonly found in young wells, showing the movement of saturated fluid from the reservoir to the processing facility. The diagram highlights the riser region, where multi-phase flow occurs and hydrate formation can be observed.	18

2.6	A comparison of hydrate formation and crystallization phenomena. (a) The crystallization process of a solution with a general concentration ($C_{solution}$) is shown by the dashed horizontal line. The solid black line represents the saturation curve, which separates the dissolved solute (right side) from the metastable region (left side). (b) The hydrate formation process, the solid black line represents the hydrate stability curve, and the zone within the hydrate domain is thermodynamically favorable for hydrate formation. Adapted from SLOAN e KOH (2008).	19
2.7	Mechanisms involved in hydrate growth according to the Shrinking Core Model. The arrows indicate where each mechanism exerts a significant influence on the hydrate growth process. Adapted from ZERPA <i>et al.</i> (2012).	23
2.8	Schematic representation of the sponge-like structure of hydrate particles, as proposed by BASSANI <i>et al.</i> (2019). The classification of particles as "wet" and "dry" depends on whether water fills the capillaries.	26
2.9	Illustration of the accumulation process in the sponge-like structure model. The figure shows the formation of a water bridge between particles after the collision.	26
2.10	Conceptual illustration comparing the predicted particle diameter (d_p) and agglomerate diameter (d_A) using the agglomeration model for a methane hydrate system.	28
2.11	Representation of a unit cell and the mechanistic depiction of slug flows as applied in the Slug Flow Model.	33
3.1	Bi-phase flash flowsheet for a known temperature, pressure, and overall composition. The dashed arrow indicates the interactive internal algorithm to solve Rachford-Rice for ζ	45
3.2	Flowsheet to obtain agglomeration diameter and effective hydrate volume fraction from agglomeration model proposed by CAMARGO e PALERMO (2002).	57
4.1	Study Case 1 Result: A comparison of hydrate formation curves obtained from previous studies and the present work, using an algorithm implemented in <i>MATLAB</i> [®] . The fluid considered contained a low concentration of CO ₂ and was suitable for sII structure. The solid black line represents the prediction from <i>Multiflash</i> [™] , the black asterisks denote the results of GUEDES (2023), and the black circles show the results obtained from this work. The dash-dotted line represents the bubble point curve predicted by <i>Multiflash</i> [™] , corresponding to the transition between the liquid and biphasic regions.	63

4.2	Case Study 2 Result: Sour natural gas containing 1.74% of CO ₂ and 0.84% of N ₂ . The black and red solid lines respectively represent the hydrate stability curves predicted by the C-G model (MEKALA e SANGWAI, 2014) and the vdW-P model (this work). The circles indicate the experimental data reported in MEKALA e SANGWAI (2014).	65
4.3	Case Study 2 Result: Sour natural gas containing 0.51% of CO ₂ and 0.43% of N ₂ . The black and red solid lines respectively represent the hydrate stability curves predicted by the C-G model (MEKALA e SANGWAI, 2014) and the vdW-P model (this work). The circles indicate the experimental data reported in MEKALA e SANGWAI (2014).	65
4.4	Case Study 2 Result: Sour natural gas containing 31.4% of CO ₂ . The black and red solid lines respectively represent the hydrate stability curves predicted by the C-G model (MEKALA e SANGWAI, 2014) and the vdW-P model (this work). The circles indicate the experimental data reported in MEKALA e SANGWAI (2014).	66
4.5	Case Study 2 Result: Sour natural gas containing 3.19% of CO ₂ and 9.59% of N ₂ . The black and red solid lines respectively represent the hydrate stability curves predicted by the C-G model (MEKALA e SANGWAI, 2014) and the vdW-P model (this work). The circles indicate the experimental data reported in MEKALA e SANGWAI (2014).	67
4.6	Case Study 2 Result: Sour natural gas containing 12.6% of CO ₂ and 5.4% of H ₂ S. The black and red solid lines respectively represent the hydrate stability curves predicted by the C-G model (MEKALA e SANGWAI, 2014) and the vdW-P model (this work). The circles indicate the experimental data reported in MEKALA e SANGWAI (2014).	68
4.7	Case Study 2 Result: Sour natural gas containing 12% of CO ₂ and 8% of H ₂ S. The black and red solid lines respectively represent the hydrate stability curves predicted by the C-G model (MEKALA e SANGWAI, 2014) and the vdW-P model (this work). The circles indicate the experimental data reported in MEKALA e SANGWAI (2014).	68
4.8	Comparison of the vapor void fraction profile along the pipeline for the steady-state flow simulation based on Caratinga field well geometry and fluid properties. The solid black line represents the gas phase fraction obtained from <i>OLGA</i> [®] using fluid properties data from <i>Multiflash</i> [™] . The solid red line shows the result obtained from this work implementing the proposed methodology in <i>MATLAB</i> [®]	70

4.9	Comparison of vapor phase (a) viscosity profile, (b) density profile, (c) velocity profile, and (d) enthalpy profile along the pipeline for the steady-state flow simulation based on Caratinga field well geometry and fluid properties. The solid black line represents the results obtained from <i>OLGA</i> [®] using fluid properties data from <i>Multiflash</i> TM . The solid red line shows the results obtained from this work implementing the proposed methodology in <i>MATLAB</i> [®]	71
4.10	Comparison of oil phase (a) fraction, (b) viscosity profile, (c) density profile, and (d) enthalpy profile along the pipeline for the steady-state flow simulation based on Caratinga field well geometry and fluid properties. The solid black line represents the results obtained from <i>OLGA</i> [®] using fluid properties data from <i>Multiflash</i> TM . The solid red line shows the results obtained from this work implementing the proposed methodology in <i>MATLAB</i> [®]	73
4.11	Comparison of aqueous phase ((a) fraction, (b) viscosity profile, (c) density profile, and (d) enthalpy profile along the pipeline for the steady-state flow simulation based on Caratinga field well geometry and fluid properties. The solid black line represents the results obtained from <i>OLGA</i> [®] using fluid properties data from <i>Multiflash</i> TM . The solid red line shows the results obtained from this work implementing the proposed methodology in <i>MATLAB</i> [®]	74
4.12	Comparison between the steady-state operational conditions of Caratinga field reported in ZERPA (2013) and the pressure vs. temperature profile for the modified fluid obtained from <i>OLGA</i> [®] and <i>MATLAB</i> [®] . The dash-dotted line represents bubble point curve obtained from <i>Multiflash</i> TM for the modified fluid. The asterisk indicates the operational conditions reported in ZERPA (2013) for the original Caratinga fluid using the software <i>OLGA</i> [®] . The black and red solid lines represent the operational conditions of the modified fluid obtained, respectively, from <i>OLGA</i> [®] and <i>MATLAB</i> [®] . The black and red dashed lines represent the hydrate stability obtained, respectively, from <i>Multiflash</i> TM and <i>MATLAB</i> [®]	75
4.13	Temperature profile along the pipeline obtained for steady-state simulation. The asterisk indicates the temperature along the pipeline reported in ZERPA (2013) for the original Caratinga fluid using the software <i>OLGA</i> [®] . The red solid and dashed lines represent, respectively, the fluid temperature profile and the equilibrium temperature for hydrate formation, both obtained from this work using <i>MATLAB</i> [®] . The blue solid curve highlights the section where the nucleation exceeds 3.5K and where positive subcooling is observed.	77

4.14	Operational conditions and the hydrate stability curve were obtained from this work, implemented in <i>MATLAB</i> [®] , for the modified fluid and Caratinga field geometry. The red solid and dashed lines represent the pressure vs. temperature profile along the pipeline and the hydrate formation curve, respectively. The dash-dotted line indicates the bubble point curve for the modified fluid obtained from <i>Multiflash</i> TM . The blue line highlights the pipeline section where the kinetics of hydrate formation satisfy the activation criteria.	78
4.15	Comparison between temperature profiles in steady-state simulations with and without hydrate formation in the riser section, obtained from this work using the methodology implemented in <i>MATLAB</i> [®] . The black and red solid lines represent the temperature profiles along the riser, respectively, without and with hydrate formation. The red dashed line shows the hydrate formation equilibrium temperature and the blue dashed line refers to the hydrate volumetric fraction.	79
4.16	Comparison between the hydrate volumetric fraction derived from the mass conservation equations (black solid line) and the effective hydrate volume fraction obtained from the agglomerate model (red dashed line) in the riser section.	81
4.17	Effects of hydrate volumetric fraction in relative viscosity observed in the riser section. The solid black line show the relative viscosity and the dashed red line refer to the effective hydrate volumetric fraction.	81

List of Tables

2.1	Typical gas hydrate structures in the O&G industry (sI and sII) and their characteristics, including the Jeffrey (1984) nomenclature, number of cages per structure, average cage radius, number of water molecules per cavity, cage types (small and large), and volume of unit cell. Adapted from GUEDES (2023).	8
2.2	Ratio of molecular diameter to cavity diameter and frequency of principal natural gas components according to the cavities they fill in hydrate structures sI and sII. Adapted from CARROL (2009).	10
3.1	Composition of light oil fluid and pure component properties data obtained from <i>Multiflash</i> TM . Reproduced from GUEDES (2023).	46
3.2	Molar composition of sour natural gas used in Case Study 2, containing varying amounts of CO ₂ , H ₂ S, and H ₂ . Adapted from MEKALA e SANGWAI (2014).	48
3.3	Saturates, aromatics, asphaltenes, and resins fractions from the SARA analysis and density of Caratinga crude oil. Adapted from SJÖBLOM <i>et al.</i> (2010).	49
3.4	Pure component properties and composition of the pseudo-fluid based on crude oil from Caratinga field without resins. Data obtained from <i>Multiflash</i> TM	50
3.5	Intrinsic formation and dissociation kinetic constants for the first-order rate kinetic model used in Eq. (3.19). Adapted from (RAO, 2013).	56
3.6	Caratinga well geometry data ZERPA (2013)	60
3.7	Pipeline material properties	60
3.8	Caratinga case study description.	60
4.1	Summary of relative error for the hydrate equilibrium curve in Case Study 2, comparing the result from this work, C-G model, and the experimental data reported in MEKALA e SANGWAI (2014).	64
A.1	A_{ki} and B_{ki} parameters from MUNCK <i>et al.</i> (1988) for Eq. (2.5).	84

A.2	Reference values of a physical constant from MUNCK <i>et al.</i> (1988) to Eq. (2.6).	84
C.1	Binary interaction parameters obtained from <i>Multiflash</i> TM library.	88

List of Symbols

A_{ki}, B_{ki}	Langmuir parameters (K/Pa, K), p. 15
C_{ki}	Langmuir coefficient (1/Pa), p. 15
F_{mw}	Frictional loss of pressure (kg/m ² /s ²), p. 31
N_{ava}	Avogadro's number (molecules/mol), p. 56
Q_{fn}	Heat exchange rate between the fluid and the neighborhood (W/m ³), p. 31
R	Universal gas constant (J/mol/K) , p. 14
T	Temperature (K), p. 14
Y_{ki}	Fractional occupancies (dimensionless), p. 14
ΔT_{sub}	Subcooling (K), p. 21
Δh_{hyd}	Enthalpy change of hydrate formation (J/kg of gas), p. 53
Γ_v	Vapor mass transfer rate (kg/m ³ /s), p. 31
α_{hyd}	Hydrate volumetric fraction (dimensionless), p. 29
β_w	Vaporized mass fraction (dimensionless), p. 32
\hat{v}_v^{dft}	Slip velocity of vapor phase (m/s), p. 31
μ	Viscosity (Pa.s), p. 27
ρ	Density (kg/m ³), p. 27
σ	Oil-water interfacial tension (N/m), p. 27
θ	Angle (°), p. 58
n_H	Hydration number (kg of gas/kg of water), p. 26
u	Chemical potential (J/mol), p. 14

v_i	Cavity per water molecules ratio (dimensionless), p. 14
τ	Shear rate (1/s), p. 28
A_s	Particle surface area (m ² /m ³), p. 21
D_p	Pipe inner diameter (m), p. 27
Fa	Cohesion force (mN/m), p. 28
P	Pressure (Pa), p. 15
U_{heat}	Overall heat transfer coefficient (W/m ² /K), p. 33
U	Velocity (m/s), p. 27
V	Molar volume (m ³ /mol), p. 15
WC	Water cut (%), p. 26
cp	Heat capacity (J/mol/K), p. 15
d_A	Particle agglomerate diameter (m), p. 27
d_p	Particle diameter (m), p. 27
e	Roughness (m), p. 59
f	Fugacity (Pa), p. 14
h	Enthalpy (J/mol), p. 15

List of Abbreviations

C-G	Chen-Guo, p. 12
CAPEX	Capital expenditure, p. 1
CPA	Cubic-Plus Association, p. 14
CSM	Colorado School of Mines, p. 22
DAE	Differential-algebraic equation, p. 36
DEH	Direct electrical heating, p. 5
DFM	Drift-Flux Model, p. 31
EoS	Equation of state, p. 14
FA	Flow assurance, p. 5
HEN	Heterogeneous Nucleation, p. 20
HON	Homogeneous Nucleation, p. 20
HSM	Hydrodynamic Slug Flow Model, p. 33
K-S	Klauda-Slander, p. 12
LDHI	Low-dosage hydrate inhibitors, p. 6
OPEX	Operating expenditure, p. 5
PR	Peng-Robinson, p. 14
PVT	Pressure, volume, and temperature, p. 4
SAFT	Statistical Associating Fluid Theory, p. 14
SRK	Soave-Redlich-Kwong, p. 14
TFM	Two-Fluid Model, p. 29

THI	Thermodynamic hydrate inhibitors, p. 6
WC	Water cut, p. 17
vdW-P	van der Waals and Platteeuw, p. 12

Chapter 1

Introduction

Gas hydrates are the central issue in flow assurance because these solid formations and blockages occur faster than other solid deposits. Hydrate formation can occur in production lines, wells, and other equipment; however, this work studied their appearance in offshore production pipelines. The industry manages hydrate formation by avoiding thermodynamic conditions that are favorable for their crystallization.

To achieve this, the combination of several techniques significantly impacts the CAPEX. Furthermore, hydrate remediation is even more expensive due to the production stop time and the equipment required to unblock the lines.

Consequently, petroleum industry efforts have intensified to describe hydrates' formation and dissociation for flow assurance purposes. The petroleum industry generally uses the term “gas hydrate” to refer to a crystalline solid – that resembles ice – compound of natural gas and water at high pressures and temperatures greater than 0°C (CARROL, 2009).

The literature on hydrates formation equilibrium (*i.e.*, pressure, temperature, and composition) with and without inhibitors is well-established, while the kinetics remains challenging.

Offshore pipelines are designed to operate outside the hydrate formation zone, mainly using insulation and injection of thermodynamic hydrate inhibitors (KOH *et al.*, 2011a, SLOAN e KOH, 2008). However, avoidance management can be uneconomical and technically unfeasible in subsea conditions due to the long tie-back (KOH *et al.*, 2011a).

As an alternative, risk management strategies look to control the time-dependent properties of gas hydrates. That means using kinetics aspects to allow the particle to form, but preventing the hydrate blockage in the pipeline (KOH *et al.*, 2011b). Three effects may influence the kinetics of hydrate formation: intrinsic kinetic, mass transfer, and heat transfer phenomena.

The prediction of hydrates formation in the pipeline require some expertise, such as: (1) fluid characterization, (2) design of hydrate stability curves, (3) knowledge of flow conditions (*i.e.*, pressure, temperature, and velocity), and (4) a suitable model that de-

scribes the hydrate formation and dissociation mechanism.

The hydrate formation in pipelines is a time-dependent phenomenon and is more significant in start-up and shutdown processes (KOH *et al.*, 2011a). Closed-source software programs perform steady-state and dynamic flow simulations, which are essential for designing and monitoring production processes. These tools usually are combined with others, to obtain the fluid properties and hydrate stability curves.

The literature presents hydrate formation models developed for oil-dominated systems (BASSANI, 2017, BASSANI *et al.*, 2019, FERREIRA, 2018, SHI *et al.*, 2011, TURNER *et al.*, 2005, ZERPA, 2013). However, due to the challenge of modeling several coexisting phenomena, the previous works neglected the combination of mechanisms that describe gas hydrate kinetics.

Model validation typically involves experimental data from flow loop facilities, due to the lack of blockage data from production pipelines. In addition, the description of fluid properties is inadequate to reproduce real scenarios. Finally, most kinetics models are limited to a single methane hydrate, which has a structure and properties inconsistent with natural gas hydrates – which contain a mixture of gases.

TEIXEIRA (2016) suggests that the Drift-Flux Model – using a differential-algebraic system – has potential to outperform the well-known Two-Fluid Model for simulating multi-phase flow in pipelines. This suggestion is supported by the successful application of Drift-Flux Model in an iterative algorithm to fit operational conditions to measure data from offshore fields in real-time applications (GÓES *et al.*, 2023).

Furthermore, the Drift-Flux Model was used in a steady-state hydrate avoidance strategy, combining three-phase flash calculations and hydrate stability analyses (GUEDES, 2023). Finally, Drift-Flux Model can also predict the liquid-gas slip velocity independent of the flow pattern correlations. (GUEDES, 2023, GÓES *et al.*, 2023).

This work aimed to incorporate the hydrate phase and its properties into the steady-state Drift-Flux Model to predict multi-phase flow in offshore pipelines susceptible to natural gas hydrate formation in oil-dominated systems. To achieve this, the model integrated the thermodynamic and kinetic aspects of hydrate formation and dissociation within pipelines in the absence of inhibitors.

The objectives of this work were twofold: (1) to quantify the impact of crystallization on flow properties, and (2) to investigate whether this approach could reproduce the behavior observed in both academic literature and well-established software programs.

1.1 General motivations

The Campos and Santos Basins comprise 95% of the Brazilian proved reservoirs (ANP, 2021). The pre-salt reservoirs in these basins have a high concentration of CO₂, which can create favorable conditions for hydrate formation. Additionally, the Santos Basin has

a higher fraction of CO₂ compared to the Campos Basin. In the Santos Basin, the levels can reach up to 80% while the Campos Basin has a lower CO₂ content of around 5%.

Hydrate formation poses significant issues such as production loss and expensive remediation strategies. To mitigate these problems, the O&G industry implements avoidance strategies, particularly through the use of thermodynamic hydrate inhibitors. However, the industry aims to reduce both the volume and cost of inhibitor injection to ensure safe exploration operations within the hydrate formation domain.

In this context, kinetic models play a fundamental role in risk management and remediation strategies. Despite this, the kinetics of hydrates in relation to thermodynamics appears to be ill-defined (CARDOSO *et al.*, 2015, SLOAN e KOH, 2008, ZHANG *et al.*, 2022).

1.2 Objectives and contribution

Figure 1.1 summarizes the aspects and steps required to predict hydrate formation in pipelines. First, a multi-phase flow model describes the interaction between phases in equilibrium and provides information about pressure, temperature, and mass flow rates. Then, thermodynamic and kinetic aspects are incorporated to support prevention, control, and remediation strategies against hydrate blockages.

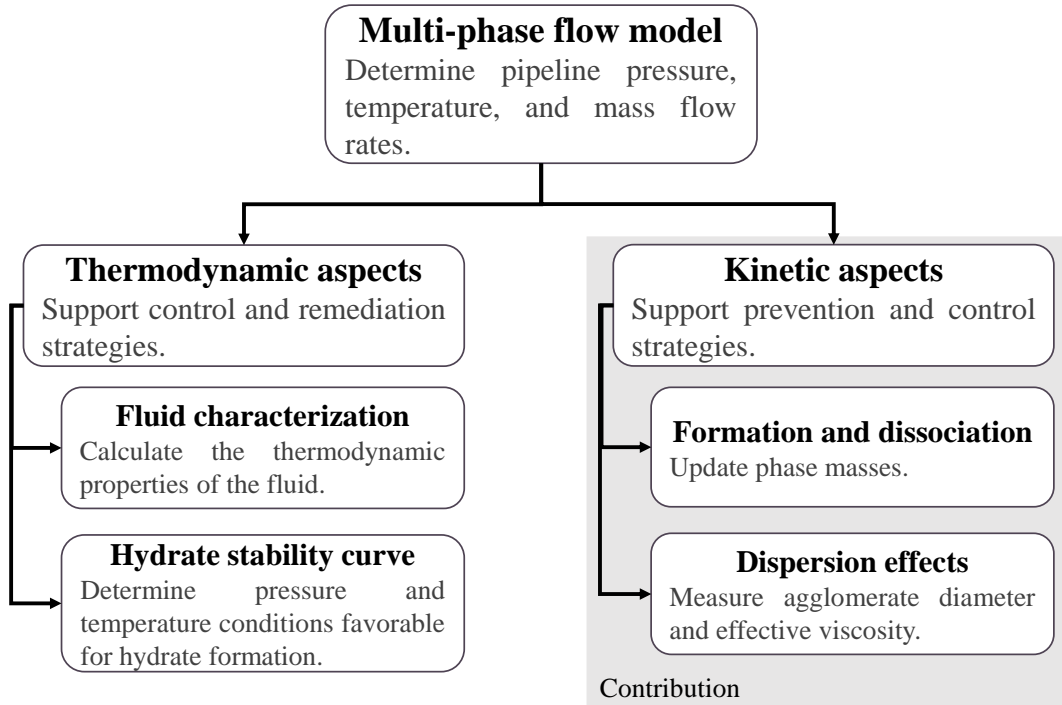


Figure 1.1: Schematic representation of the steps involved in predicting hydrate formation and dissociation in pipelines. The highlighted box emphasizes the contribution of this work to the continued research aimed at improving the understanding of multi-phase flow in production pipelines.

Thermodynamic aspects determine the fluid PVT properties and estimate the hydrate stability curve. Kinetic aspects describe the rate at which the formation and dissociation phenomena occur, while the effects of dispersion on fluid properties are predicted by a rheology model. The kinetic model varies depending on the type of emulsion in which the hydrate particle growth occurs, typically classified as oil-, water-, or gas-dominated systems.

This work continues the research aimed at developing a flow assurance simulation tool that can describe the multi-phase flow in production pipelines (GUEDES, 2023, GUEDES *et al.*, 2020, GÓES *et al.*, 2023, TEIXEIRA, 2016, TEIXEIRA *et al.*, 2015). The previous works determined a simple, but accurate, model to simulate the multi-phase flow in pipelines in agreement with the well-known software *OLGA*®.

The hydrodynamic model includes a thermodynamic model which characterizes a Newtonian and compressible fluid. In addition, the hydrate stability curve is evaluated simultaneously with the flow conditions to verify whether the pipe section is within the hydrate formation domain.

This work proposes combining kinetic and thermodynamic aspects of hydrates into a steady-state multi-phase flow simulator. To achieve this, a kinetics model and hydrate conservative equations were included into the Drift-Flux Model.

The modified model was able to identify the sections of the pipeline prone to blockages and quantify the amount of crystals formed. Finally, to ensure the accuracy of the results, several case studies were conducted to analyze the agreement of the results with the literature and commercial software programs.

1.3 Structure of the text

A review of the stages required to model gas hydrates in pipelines is presented in Chapter 2. Chapter 3 describes the methods, equations, and algorithms used to model hydrate formation and dissociation into the Drift-Flux Model. This chapter also presents planned case studies to investigate the limitations of this work and to suggest improvements. The results are discussed in Chapter 4, and the conclusions are presented in Chapter 5.

Chapter 2

Gas hydrates in the O&G industry

The Second World War impacted the fluid transport logistics and the demand for natural gas, leading to a shift in exploration towards offshore fields (SLOAN e KOH, 2008). Simultaneously, the flow dynamics for production and transport of fluids became increasingly complex, providing opportunities for flow assurance (FA) science to find room for improvement (BOMBA *et al.*, 2018).

Flow assurance is an engineering discipline focused on ensuring the safe and uninterrupted production of fluids from the reservoir to the point of delivery. The optimal structure and production conditions for each system are based on designing, controlling, and monitoring the flow processes (BOMBA *et al.*, 2018), taking into account the following areas:

- (a) Operational, focusing on steady-state and dynamic multi-phase flow simulations,
- (b) Integrity, addressing issues such as erosion, fatigue, and corrosion,
- (c) Blockage or increased frictional losses due to emulsions and solids deposition (*i.e.*, wax precipitation, asphaltene deposition, scaling, sand deposition, and hydrate formation), and
- (d) Design and operation procedures.

Regarding solid deposits, controlling gas hydrates constitutes a significant part of the CAPEX and OPEX for a subsea exploration project (CARDOSO *et al.*, 2015, ZHANG *et al.*, 2022). Predicting and controlling gas hydrates formation in a flowline is essential for field design and production.

Five strategies are usually applied for gas hydrates control: (1) process solutions, (2) hydraulic methods, (3) thermal methods, (4) chemical methods, and (5) no hydrate control measures. Figure 2.1 presents a list of FA techniques commonly used in each strategy for gas hydrate control (KINNARI *et al.*, 2014).

The insulation design and injecting thermodynamic hydrate inhibitors (THI) are the typical techniques to ensure operation outside the hydrate stability domain. However, the

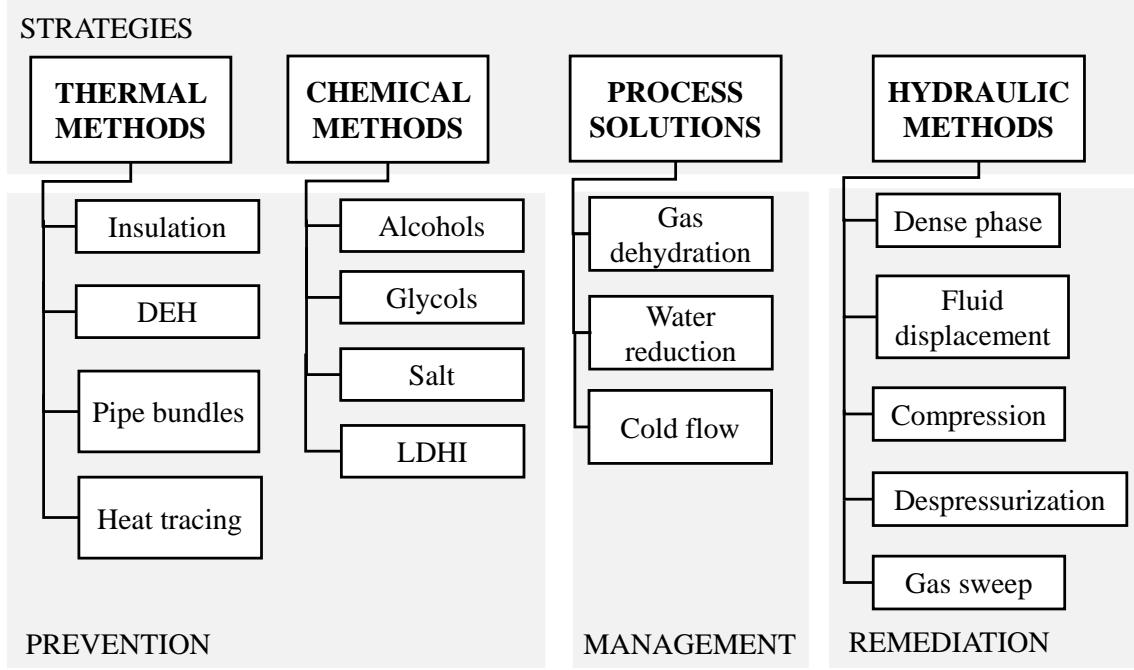


Figure 2.1: Flow assurance techniques commonly employed in strategies for gas hydrate control. The gray boxes separate the techniques according to their application in hydrate prevention, management, and remediation. Adapted from KINNARI *et al.* (2014).

THI injection may be technically unfeasible in offshore pipelines (KOH *et al.*, 2011a, ZHANG *et al.*, 2022). Thus, the insulation requires another complementary method.

Instead of avoiding hydrate formation, the new FA approach focuses on risk management strategies that allow safe operation within the hydrate stability domain by preventing blockages using time-dependent properties (CARDOSO *et al.*, 2015).

To achieve this, risk management strategies aim to use low-dosage hydrate inhibitors (LDHIs) that require a lower volume of inhibitor injection to prevent hydrate blockages compared to THI (KOH *et al.*, 2011a, ZHANG *et al.*, 2022).

There are two categories of LDHIs: kinetic hydrate inhibitors and anti-agglomerate. The first prevents the nucleation stage, while the second functions similarly to a surfactant, leading to a suspension of water drops.

In the present work, the focus was on implementing the following stages required to simulate hydrate formation in production pipelines: (1) obtaining fluid composition and characterization, (2) describing the flow conditions within the pipeline (*i.e.*, pressure, temperature, and velocity), (3) designing hydrate equilibrium diagrams, and (4) conducting crystallization analysis. For this reason, the application of control methods is beyond the scope of this work but can be included in future studies.

In relation to the first and second stages, commercial software programs, such as *MultiflashTM* and *PVTsim[®]*, typically organize fluid properties in tables for a range of pressures and temperatures. This information is then fed into another software, such as *OLGA[®]*, which simulates multi-phase flow within the pipeline, either dynamically or in a

steady state.

Conversely, the literature presents studies employing simplified hydraulic and thermal equations, with fluid properties determined under assumptions of incompressible fluid or ideal gas behavior.

Details about the stages to simulate hydrate formation in production pipelines are presented in this chapter, which is structured with the following sections:

- Section 2.1 presents the main information about gas hydrate structure and the component found in the O&G industry.
- Section 2.2 reviews the theory used to obtain the hydrate stability curve, which is used to predict temperature and pressure favorable for hydrate formation according to the components, fluid composition, and type of hydrate structure.
- Section 2.3 reviews the kinetic models available in the literature to measure gas hydrates formation.
- Section 2.4 presents the hydrodynamic models found in the literature to simulate multi-phase flow in pipes and their application in predicting hydrate formation and dissociation.
- Section 2.5 presents the literature performing three-phase flash calculations to obtain the fluid composition and support the analysis of the hydrate stability curve.

2.1 Gas hydrates characteristics

Understanding guest and host molecules is essential for analyzing hydrate formation and dissociation. Such data is necessary to predict the type of crystal structure, which affect the shape of the hydrate stability curve.

This section presents the theory of hydrate structures and their main components in the petroleum and natural gas industry. This information leads to properties that impact flow simulations, which are among the objectives of this work.

2.1.1 Hydrate structure

Clathrates are substances formed by two components: host molecules and guest molecules. Host molecules form stabilized structures by enclosing a guest molecule within them (CARROL, 2009).




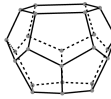


In gas hydrates structures, the host molecules refer to water molecules, while the compounds stabilizing the crystal are called “guest molecules” or “formers” (CARROL, 2009). This crystal formation occurs due to the unusual behavior of water molecules at low temperatures.

The hydrogen bonds between water molecules enable the formation of non-linear structures, known as cages or cavities. These cavities are larger compared to those found in ice structures. Consequently, the hydrate lattice remains intact, not collapsing due to repulsive forces, even after the occupation by guest molecules (SLOAN e KOH, 2008).

The composition of hydrates is non-stoichiometric; the degree of saturation is determined by pressure and temperature (CARROL, 2009, KOH *et al.*, 2011a, SLOAN e KOH, 2008). As a consequence, gas hydrates can form even without guest molecules occupying all the cavities in the hydrate lattice. However, if there are not enough filled cages, the lattice collapses and does not form crystals (CARROL, 2009, KOH *et al.*, 2011a).

Three well-known hydrate structures exist: sI or Type I, sII or Type II, and sH or Type H (CARROL, 2009, KOH *et al.*, 2011a, SLOAN e KOH, 2008). Each structure has different cages and formers involved, and the arrangement of the crystal determines the gas hydrate properties (SLOAN e KOH, 2008). Table 2.1 shows the typical gas hydrates structures and their characteristics.

Table 2.1: Typical gas hydrate structures in the O&G industry (sI and sII) and their characteristics, including the Jeffrey (1984) nomenclature, number of cages per structure, average cage radius, number of water molecules per cavity, cage types (small and large), and volume of unit cell. Adapted from GUEDES (2023).

Properties	sI structure		sII structure	
				
	Small cavity	Large cavity	Small cavity	Large cavity
Polyhedral structure				
Nomenclature Jeffrey (1984) ^a	5 ¹²	5 ¹² 6 ²	5 ¹²	5 ¹² 6 ⁴
Cages per unit cell ^a	6	2	16	8
Average cavity radius ^a (Å)	3.95	4.33	3.91	4.73
Variation in radius (%) ^a	3.4	14.4	5.5	1.73
Number of H ₂ O/cavity ^b	46		136	
Volume of unit cell (m ³) ^b	1.728x10 ⁻²⁷		5.178x10 ⁻²⁷	

^a Data available in SLOAN e KOH (2008).

^b Data available in CARROL (2009).

The sI and sII structures are typically encountered in the O&G industry because their formers are commonly found in natural gas (KOH *et al.*, 2011a). Knowledge about hy-

hydrate structure is essential to predict the hydrate formation curve and apply suitable management techniques.

Usually, natural gas in offshore pipelines forms sII hydrates (SLOAN e KOH, 2008). The sH structure requires two sizes of formers to stabilize the crystal, and the larger guest molecule is uncommon in natural gas. As a result, the sH structure is not included in the scope of this work.

The combination of guest molecule size and cavity diameter determines the crystal structure (KOH *et al.*, 2011a). The structure sI is constructed of 46 water molecules, and is composed of dodecahedron (small) and tetrakaidecahedron (large) cages. The structure sII consists of 136 water molecules, and is composed of dodecahedron (small) and hexakaidecahedron (large) cages.

The Jeffrey (1984) terminology, $n_i^{m_i}$, represents the polyhedral structures of hydrate cavities. For these polyhedra, n_i is the number of edges in face type 'i', and m_i is the number of faces with n_i edges (SLOAN e KOH, 2008). The small cavity (5^{12}) is a dodecahedron, a polyhedron with twelve pentagonal faces. This cage is present in all hydrate types.

The dodecahedron structure requires twenty water molecules connected through hydrogen bonds, with oxygen atoms in each vertex. Table 2.1 shows that 5^{12} is almost spherical because it has a low percentage variation in radius (SLOAN e KOH, 2008). This cavity will be filled if the guest molecules have a proper size – a radius around 3.95 Å and 3.91 Å in structures sI and sII, respectively. Molecules with a radius less than 3.0 Å are too small to fill any cavity (SLOAN e KOH, 2008).

The large cavity in sI, $5^{12}6^2$, is a tetrakaidecahedron with twelve pentagonal faces and two hexagonal faces. The tetrakaidecahedron is similar to an ellipsoid and features the most non-spherical (14.4%) geometry in sI or sII (SLOAN e KOH, 2008). This cavity has an average radius of 4.33 Å and can accommodate molecules smaller than 6.0 Å in diameter.

The large cavity in sII, $5^{12}6^4$, is a hexakaidecahedron with twelve pentagonal faces and four hexagonal faces. Therefore, the hexakaidecahedron can be stabilized with molecules as large as 6.6 Å in diameter, even if the small cavities remain empty (CARROL, 2009, SLOAN e KOH, 2008).

2.1.2 Guest molecules in natural gas

The principal molecules that comprise natural gas are nitrogen (N_2), carbon dioxide (CO_2), hydrogen sulfide (H_2S), methane (CH_4), ethane (C_2H_6), propane (C_3H_8), and butane (i- C_4H_{10} and n- C_4H_{10}) (SLOAN e KOH, 2008). All of these substances may form gas hydrates and fill specific cages.

Table 2.2 shows the molecular diameter of these formers and which cavity each

molecule fills. The structures sI and sII can be formed with only one type of guest molecule. Nitrogen, carbon dioxide, hydrogen sulfide, and methane can occupy large and small cavities in both structures (CARROL, 2009).

Table 2.2: Ratio of molecular diameter to cavity diameter and frequency of principal natural gas components according to the cavities they fill in hydrate structures sI and sII. Adapted from CARROL (2009).

Guest molecule	Diameter ¹ (Å)	D _{molecular} /D _{free cavity}				Frequency in cavity			
		sI structure		sII structure		sI structure		sII structure	
		5 ¹²	5 ¹² 6 ²	5 ¹²	5 ¹² 6 ⁴	Small	Large	Small	Large
N ₂	4.1	0.804	0.700	0.817*	0.616*	✓	✓	✓	✓
CO ₂	5.12	1.00*	0.834*	1.02	0.769	✓	✓	✓	✓
H ₂ S	4.58	0.898*	0.782*	0.912	0.687	✓	✓	✓	✓
CH ₄	4.36	0.855*	0.744*	0.868	0.655	✓	✓	✓	✓
C ₂ H ₆	5.5	1.08	0.939*	1.10	0.826	✗	✓	✗	✓
C ₃ H ₈	6.28	1.23	1.07	1.25	0.943*	✗	✗	✗	✓
i-C ₄ H ₁₀	6.5	1.27	1.11	1.29	0.976*	✗	✗	✗	✓
n-C ₄ H ₁₀	7.1	1.39	1.21	1.41	1.07	✗	✗	✗	✓

¹ Molecular diameter.

* Cavities filled by one type of hydrate former.

Usually, molecules larger than n-butane cannot form hydrates. However, as an exception, n-butane in the presence of another guest molecule can fill the large cavity in the Type II structure (CARROL, 2009). More information about guest molecules is available in CARROL (2009).

Guest molecules like carbon dioxide, hydrogen sulfide, and nitrogen bring non-idealities to gas hydrate stability prediction. More details are provided in the following section.

2.2 Thermodynamics of gas hydrates

Accurate predictions of phase equilibrium are crucial for the safe and efficient design of process facilities in the O&G industry, as well as for the development of effective safety hazard strategies.

Because hydrate equilibrium temperature and pressure are predictable, operational risk conditions can be avoided, serving as the primary safety approach. This section presents the methods for obtaining a hydrate stability curve, reviews the characteristics of these phase diagrams, and discusses widely used software programs.

2.2.1 Hydrates equilibrium curves

Eq. (2.1) shows the Gibbs Phase's Rule, which represents a criterion for determining the equilibrium phases coexisting in a phase diagram.

$$F = C - P + 2 \quad (2.1)$$

where F is the number of intensive variables needed to specify the system, C is the number of components in the system, and P is the number of phases in the system. Usually, the phase equilibrium is represented in terms of pressure and temperature because these variables are commonly measured in processes.

Phase diagrams are helpful for flow assurance because they predict the conditions that favor the guest molecules – of adequate size – to become entrapped in a crystal structure formed by water molecules (CARROL, 2009, KOH *et al.*, 2011a). In addition, the hydrate stability curve is essential for predicting whether operational conditions are inside or outside the hydrate zone.

Figure 2.2 shows phase diagrams containing two components. Figure 2.2 (a) presents a phase diagram with one quadruple point (Q_1) and Figure 2.2 (b) presents a system with an upper quadruple point (Q_2).

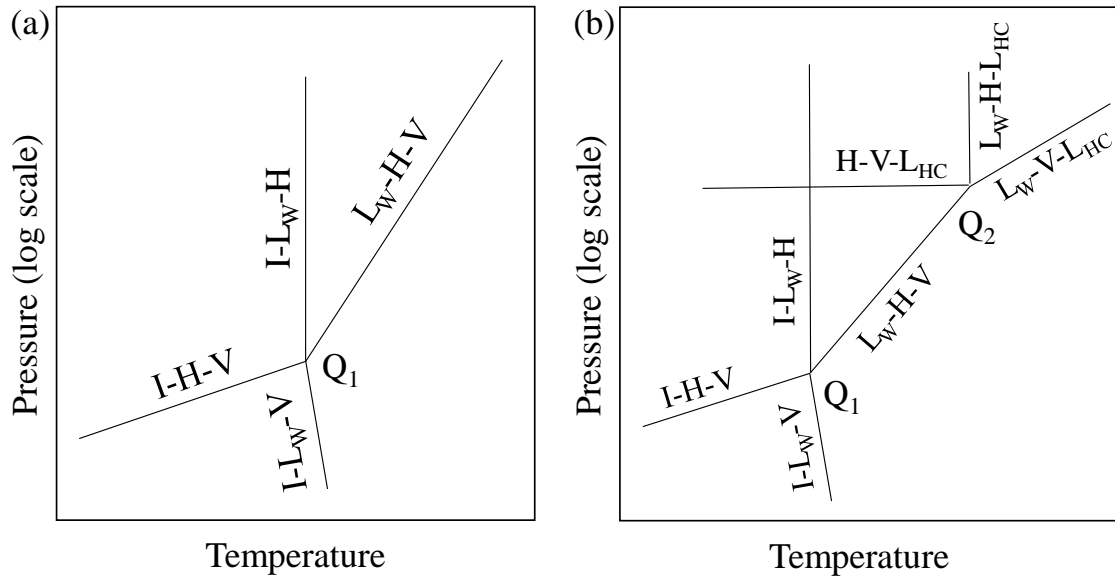


Figure 2.2: Phase diagrams of two-component systems, showing (a) methane–water or nitrogen–water system, a phase diagram with one quadruple point (Q_1) and (b) hydrocarbon–water system, which presents an upper quadruple point (Q_2). The diagrams illustrate the following phases: ice (I), liquid (L_W for water and L_{HC} for hydrocarbon), vapor (V), and hydrate (H), as well as their equilibria. The intersection points between the lines represent quadruple points (Q_1 and Q_2) where four phases coexist. Adapted from SLOAN e KOH (2008).

By Gibbs Phase's Rule, the number of phases will set the number of intensive variables

needed to specify the system ($F = 4 - P$). The pressure versus temperature diagram contains four phases: ice (I), liquid (L_W for water and L_{HC} for hydrocarbon), vapor (V), and hydrate (H).

The surface region illustrates the bi-phase equilibrium, the lines represent three-phase equilibrium, and the intersection point between the lines shows the quadruple point, where four phases coexist. Methane and nitrogen gas hydrates have only one quadruple point (Q_1), while other formers in natural gas also have an upper quadruple point (Q_2). The Q_1 temperature approximates $273K$ for all gas hydrates (SLOAN e KOH, 2008).

The lines connected to these points have different inclinations, so the prediction of phase equilibrium requires a suitable method according to the component, composition, and type of hydrate structure. The hydrate equilibrium curve divides the P vs. T diagram into two regions: to the right of the curve is the hydrate-free region; to the left is the hydrate-formation area.

The curve's shape may change with the fluid composition, the type of hydrate structure, and the percentage of inhibitors. This work did not incorporate hydrate avoidance strategies involving thermodynamic or kinetic inhibitors, but such aspects can be included in future studies.

Figure 2.3 illustrates the fluid pressure vs. temperature profile in the subsea pipeline and the hydrate stability regions. The solid gray line represents pipeline operational conditions from a deepwater wellhead to the processing facility. The shaded envelopes are the hydrate-formation curves for different amounts of THI. Any fluid within the pipeline section in the hydrate-formation domain may form gas hydrates, resulting in plugging.

The combination of hydrates structures and statistical thermodynamics knowledge allowed the development of phenomenological models to describe the thermodynamics of gas hydrates. Only the stable hydrate phase (sI or sII) results in a minimum of Gibbs energy (CARROL, 2009). In the O&G pipelines, type II structure is expected due to natural gas components (KOH *et al.*, 2011a, SLOAN e KOH, 2008).

There are three main thermodynamic models to predict gas hydrates equilibrium: (1) the van der Waals and Platteeuw model (vdW-P), (2) the Chen-Guo model (C-G), and (3) the Klauda-Sandler model (K-S). The second and third models are derivations from the vdW-P model but do not consider the reference state of the empty hydrate lattice.

The hypothesis of this empty hydrate lattice requires reference parameters and empirical correlations, which are obtained from the regression analysis of experimental data. In the vdW-P model, the hydrate formation conditions occur under the equality of water and hydrate phases' chemical potentials; instead, the C-G and K-S models use equality of fugacity.

The fugacity-based approach eliminated the need for reference parameters, thus minimizing the use of empirical relations (KLAUDA e SANDLER, 2000, WANG *et al.*, 2021). In addition, the K-S model simplified some parameters related to equilibrium phases and

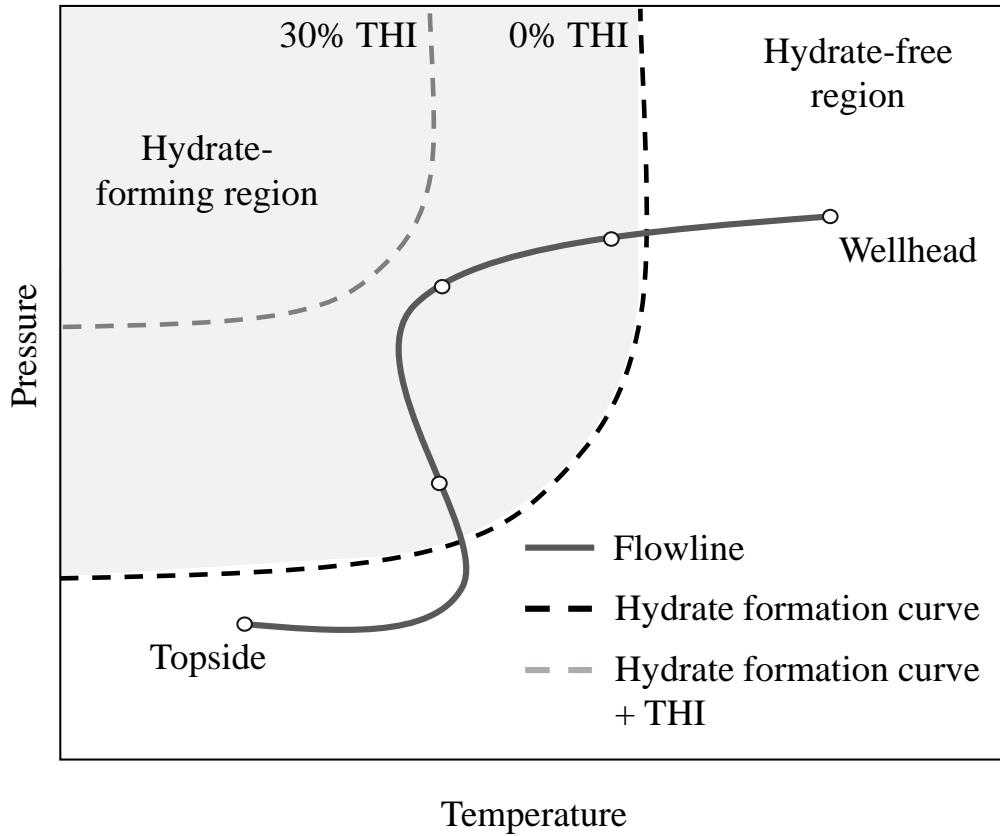


Figure 2.3: Operational conditions of subsea pipelines and hydrate stability regions. The solid gray line represents pipeline operational conditions from a deepwater wellhead to the processing facility. The shaded envelope indicates the hydrate stability curve. Each shaded curve represents the equilibrium conditions containing different amounts of thermodynamic hydrate inhibitors. Adapted from SLOAN e KOH (2008).

improved the accuracy of the previous models over a wide temperature range; however, it is limited to single guest hydrates (KLAUDA e SANDLER, 2000).

The C-G model applies a two-step mechanism, first a quasi-equilibrium reaction and then equilibrium adsorption, also used in vdW-P theory. This method connects the hydrate properties with guest molecule – a limitation on vdW-P. The equilibrium diagram derived from this method can be applied to the kinetics of hydrate formation, using the difference in fugacity as a driving force (SHI *et al.*, 2011).

The C-G model considers complexities in the formation and dissociation of sour gases (MEKALA e SANGWAI, 2014, ZARENEZHAD e ZIAEE, 2013). The literature shows applications of the C-G model for phase equilibrium containing organic inhibitors (LI *et al.*, 2021), salts, and ionic liquid inhibitors (WANG *et al.*, 2021).

For this work, complex scenarios involving inhibitors or components that cause inaccuracies are out of scope. However, the vdW-P model has seen extensive improvement over the years (MEDEIROS *et al.*, 2020) and is applied to well-known commercial software programs that support industrial operations and training (BALLARD e SLOAN,

2004b).

Several modifications demonstrated that the vdW-P model could be suitable for phase equilibrium and stability analysis (KHAN *et al.*, 2018, SEGTOVICH *et al.*, 2016), even in the presence of organic inhibitors (BALLARD e SLOAN, 2004b, CHIN *et al.*, 2013) and electrolytic additives (CHIN *et al.*, 2013).

The vdW-P model applies the following assumption in statistical thermodynamics (MEDEIROS *et al.*, 2020):

- The host molecules have a separate contribution to the free energy of clathrate from the rest of the system.
- Guest molecules are located individually within the cage in the lattice.
- Host molecules surround the guest molecule, but the interaction between guest molecules in different cages is negligible.

The approach to describe the thermodynamics of hydrates formation includes two steps: first, pure water (ω , liquid or ice phase) forms an empty hydrate lattice (\varkappa , a hypothetical state), and then this structure is filled to produce the hydrate phase (H). The equilibrium of hydrate formation occurs when the chemical potential of water (u_w) between the existing phases (ω and H) is equal, as shown in Eq. (2.2):

$$u_w^H - u_w^\omega = (u_w^H - u_w^\varkappa) + (u_w^\varkappa - u_w^\omega) \quad (2.2)$$

The first term on the right side of Eq. (2.2) can be described by the van der Waals and Platteuw model (PLATTEEUW e VAN DER WAALS, 1958). This model corresponds to the relationship between the chemical potential of water in the gas hydrate structure and the hypothetical empty hydrate lattice phases.

For a mixture of gas hydrates, PARRISH e PRAUSNITZ (1972) modified the vdW-P model as shown in Eq. (2.3):

$$u_w^H - u_w^\varkappa = RT \sum_{i=1} v_i \ln \left(1 - \sum_{k=1} Y_{ki} \right) \quad (2.3)$$

where v_i is the number of cavities of type i (see Table 2.1) and Y_{ki} is the probability of guest molecule k occupies the cavity type i . The fractional occupancy, Y_{ki} , can be obtained using Eq. (2.4):

$$Y_{ki} = \frac{C_{ki} f_k}{1 + \sum_{j=1} C_{ji} f_j} \quad (2.4)$$

where f_k is the component's fugacity and C_{ki} is the Langmuir coefficient of guest molecule k in the cage type i . The fluid phase fugacity can be calculated using an equation of state (EOS) such as Soave-Redlich-Kwong (SRK), Peng-Robinson (PR), Cubic-Plus Association (CPA), Statistical Associating Fluid Theory (SAFT), *etc.*

The Langmuir coefficient quantifies the guest-host molecule interactions used to obtain fractional occupancies in Eq. (2.4). The coefficient varies with temperature and gas composition. Moreover, it depends on the lattice volume and the number of host molecules of the lattice (SEGTOVICH *et al.*, 2016). The temperature correlation given by Eq. (2.5) can be used to determine the Langmuir coefficient.

$$C_{ki} = \frac{A_{ki}}{T} \exp\left(\frac{B_{ki}}{T}\right) \quad (2.5)$$

where A_{ki} and B_{ki} are the Langmuir parameters of a single or a mixture of gas hydrates.

The second term on the right side of Eq. (2.2) is determined by the classical thermodynamics of pure water (*i.e.*, liquid or ice phase) in a transition from ω to \varkappa condition, as shown in Eq. (2.6):

$$\begin{aligned} \frac{\Delta u_w^{\varkappa-\omega}}{RT} = & \frac{\Delta u_w^{\varkappa-\omega}(P_0, T_0)}{RT_0} + \frac{\Delta V^{\varkappa-\omega}}{RT} \Delta P \\ & - \left(\frac{\Delta h^{\varkappa-\omega,0} - T_0 \Delta c_p^{\varkappa-\omega,0}}{R} \right) \left(-\frac{1}{T} + \frac{1}{T_0} \right) + \left(\frac{\Delta c_p^{\varkappa-\omega,0}}{R} \right) \ln\left(\frac{T}{T_0}\right) \end{aligned} \quad (2.6)$$

where u is the chemical potential, P is the pressure, T is the temperature, h is the enthalpy, cp is the heat capacity, R is the universal gas constant, and V is the molar volume. $\varkappa - \omega$ represents the change from a pure water phase to a hydrate phase, and the subscripts 0 and w represent the reference state and water, respectively.

Considering the vdW-P model assumptions, two factors describe the phenomenon of a guest molecule in the lattice (MEDEIROS *et al.*, 2020): (1) the degree of freedom of the enclosed molecule, and (2) the interaction between the guest and the host molecules.

The vdW-P model's main limitations occur due to assumptions that do not account for the following effects (KHAN *et al.*, 2018, MEDEIROS *et al.*, 2020, MEKALA e SANGWAI, 2014):

- (a) The interactions between guest molecules,
- (b) The effect of hydrogen bonding,
- (c) Electrolyte contributions, and
- (d) Variations in lattice volume and radius of the cages.

Quadrupolar or polar formers, such as CO_2 and H_2S , lead to complexities in predicting the hydrate formation and dissociation conditions due to: (1) their solubility in water, which increases the inaccuracy in predicting hydrate dissociation (ZARENEZHAD e ZIAEE, 2013), and (2) the polarity, which affects the interaction between guest molecules in the hydrate lattice (MEKALA e SANGWAI, 2014).

As a result, these components remain stable in hydrate structure at higher temperatures and lower pressures than other guest molecules in natural gas (MEKALA e SANGWAI, 2014). Another inaccuracy occurs related to multiple occupations of N_2 molecules in the lattice, which is a limitation of vdW-P assumptions.

Modifying the Langmuir coefficient's calculations is a common way to deal with inaccuracy (MEDEIROS *et al.*, 2020). The calculation methods for Langmuir coefficient's, C_{ki} , may use statistical techniques and potential models. The original vdW-P model accounted for the pairwise interaction of molecules using the Lenard-Jones and Devonshire equation, which presents better results for spherical molecules.

Kihara potential varied the previous spherical symmetrical potential, adding more parameters capable of considering the shapes of different molecules. Next, the Langmuir parameters would be obtained using the square well potential function (MEDEIROS *et al.*, 2020). In 1988, the parameters were obtained from experimental data applicable to natural gas and oil (MUNCK *et al.*, 1988).

There are commercial software programs designed for industrial analyses, which are capable of predicting fluid properties as well as hydrate formation curves. Then, flow simulators use this information as input to perform FA studies, for example.

Regarding the design of hydrate formation conditions, the following well-known software are used to predict the thermodynamic stable hydrate structures and cage occupancy: *PVTsim*[®] (Calsep A/S), *Multiflash*TM (Infochem Computer Services Ltd.), and *CSMGem* (Colorado School of Mines) (BALLARD e SLOAN, 2004b, BOMBA *et al.*, 2018, KOH *et al.*, 2011b).

They all use the van der Waals and Platteuw theory to predict hydrate formation. The performance of the software programs above was compared with experimental data of hydrate formation for uninhibited and inhibited systems (*i.e.*, methanol and salts) (BALLARD e SLOAN, 2004b). The authors reported significant errors for the vdW-P model related to higher amounts of inhibitors, salts, and H_2S (BALLARD e SLOAN, 2004b).

According to BALLARD e SLOAN (2004b), *Multiflash*TM provided good temperature equilibrium predictions compared to experimental data for uninhibited systems of multi-components hydrates, conditions which are the subject of this work. The literature also suggests that *Multiflash*TM provided acceptable results in systems containing a low concentration of H_2S or pure H_2S hydrate in sI structure (BALLARD e SLOAN, 2004b, KHAN *et al.*, 2018).

2.3 Kinetics of gas hydrates

Favorable thermodynamic conditions do not guarantee the immediate formation of hydrates. The current trend and challenge in the O&G industry involve operating with solid formation, but avoiding blockages using risk management strategies rather than avoidance

management.

Kinetics describes the time-dependent properties that govern the processes of nucleation, growth, massive agglomeration, and eventual plugging by hydrates. The mechanism of hydrate formation is intrinsically connected to the emulsion where hydrate particles form and grow. The following section provides an overview of the general concept of the kinetics of gas hydrate formation.

2.3.1 Oil-dominated systems

There are three domains in which hydrate formation may be observed in pipelines: oil-, water-, and gas-dominated systems (ZERPA *et al.*, 2012). The first is related to low gas-to-liquid ratios, forming water-in-oil (W/O) emulsions. The second system is characterized by high water cut (WC), leading to oil-in-water (O/W) emulsions. In such scenarios, mass transfer models are usually applied to describe the gas diffusion in the liquid phase (DUAN *et al.*, 2021, SAKURAI *et al.*, 2022, SHI *et al.*, 2011, ZERPA *et al.*, 2012).

Finally, the last system has high gas-to-liquid ratios and requires more fundamental work to understand the mechanism governing hydrate growth (ZERPA *et al.*, 2012). The present work focuses on modeling hydrates formation in oil-dominated systems because our fluid characterization methodology is limited to low WC. Thus, water- and gas-dominated systems are outside the scope of this work.

Three phases (*i.e.*, gas, water, and oil) coexist in the pipeline, adding complexity to hydrate formation models. It is important to highlight that gas and water phases must be present for hydrate formation. Figure 2.4 illustrates the following steps of hydrate formation in oil-dominated systems (KOH *et al.*, 2011a, ZERPA *et al.*, 2012):

1. First, water droplets are dispersed in the continuous oil phase (W/O emulsions),
2. Gas is consumed, forming a hydrate film between the water and oil interface,
3. The water droplet is fully converted to gas hydrate particles that may begin to agglomerate, and
4. The plug formed can block the pipeline, requiring remediation methods.

Figure 2.5 illustrates the hydrate formation in oil-dominated systems, which are common in young wells. In this picture, a saturated fluid flows from the wellhead to the floating production storage and offloading (FPSO) at the surface. The multi-phase flow usually occurs close to the riser region due to a decrease in temperature and pressure.

In oil-dominated systems, it is assumed that water is dispersed within the continuous oil phase, typically accounting for less than 50% WC (CARDOSO *et al.*, 2015, KOH *et al.*, 2011a). Hydrate formation can occur at nucleation sites, such as changes in pipe geometry, control devices, or sand deposits, where free water tends to accumulate. In

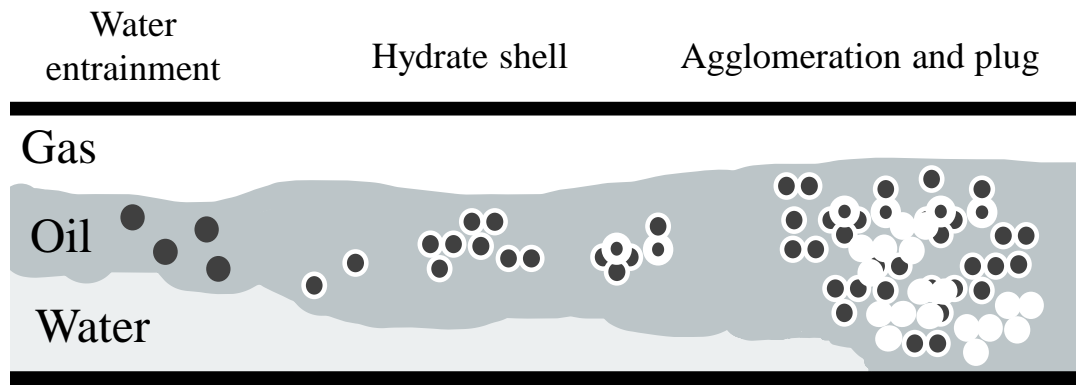


Figure 2.4: Schematic representation of hydrate formation in oil-dominated systems, including water droplet dispersion in the continuous oil phase, hydrate shell formation, followed by extensive agglomeration and plugging. Adapted from ZERPA *et al.* (2012).

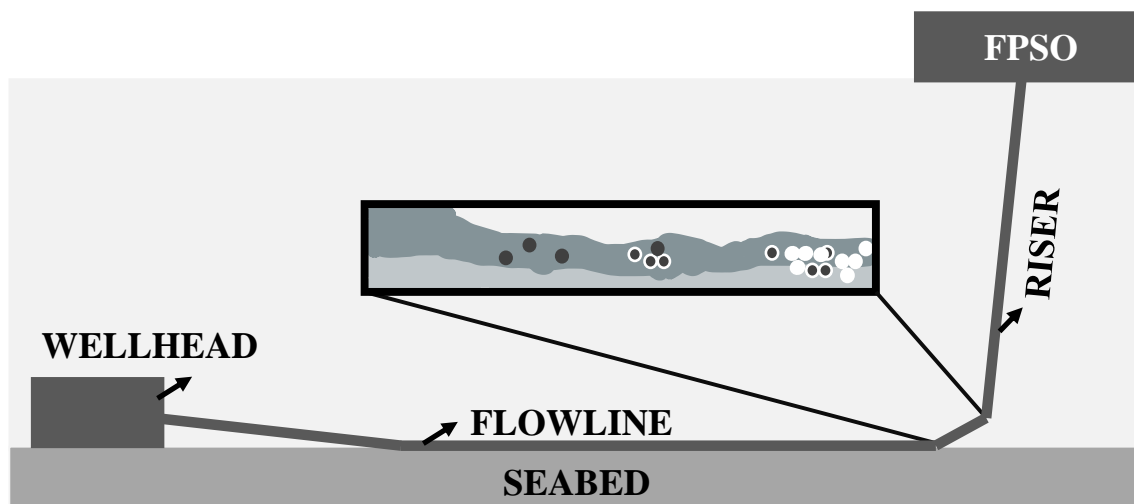


Figure 2.5: Schematic representation of an oil-dominated system commonly found in young wells, showing the movement of saturated fluid from the reservoir to the processing facility. The diagram highlights the riser region, where multi-phase flow occurs and hydrate formation can be observed.

general, production operations within oil-dominated systems have a low risk of hydrate blockage. This is because hydrates often dissociate during depressurization in the riser section.

In production operations, blockage scenarios are common during start-ups and shut-downs when free water accumulates and temperature decreases (CARROL, 2009, KOH *et al.*, 2011a). An elevated water cut (WC) can also raise the risk of hydrate formation (WANG *et al.*, 2018a, ZERPA *et al.*, 2012). A dynamic study is required to measure the risk of blockage during production stops.

The literature contains growth models involving intrinsic kinetics, heat, and mass transfer mechanisms inside and outside the water droplets (GONG *et al.*, 2010, SHI *et al.*, 2011, ZERPA *et al.*, 2012). Each mechanism plays a role at different times during hydrate formation.

2.3.2 Water properties and hydrate formation

Figure 2.6 illustrates a typical comparison between hydrate formation and crystallization phenomena. Figure 2.6 (a) displays the crystallization process of a solution containing a general concentration, indicated by the dashed horizontal line labeled $C_{solution}$.

The thermodynamics of crystal nucleation and growth in the crystallization process depend on the degree of supersaturation and temperature. On the right side of the equilibrium curve, represented by the solid black line called saturation, the solute is fully dissolved.

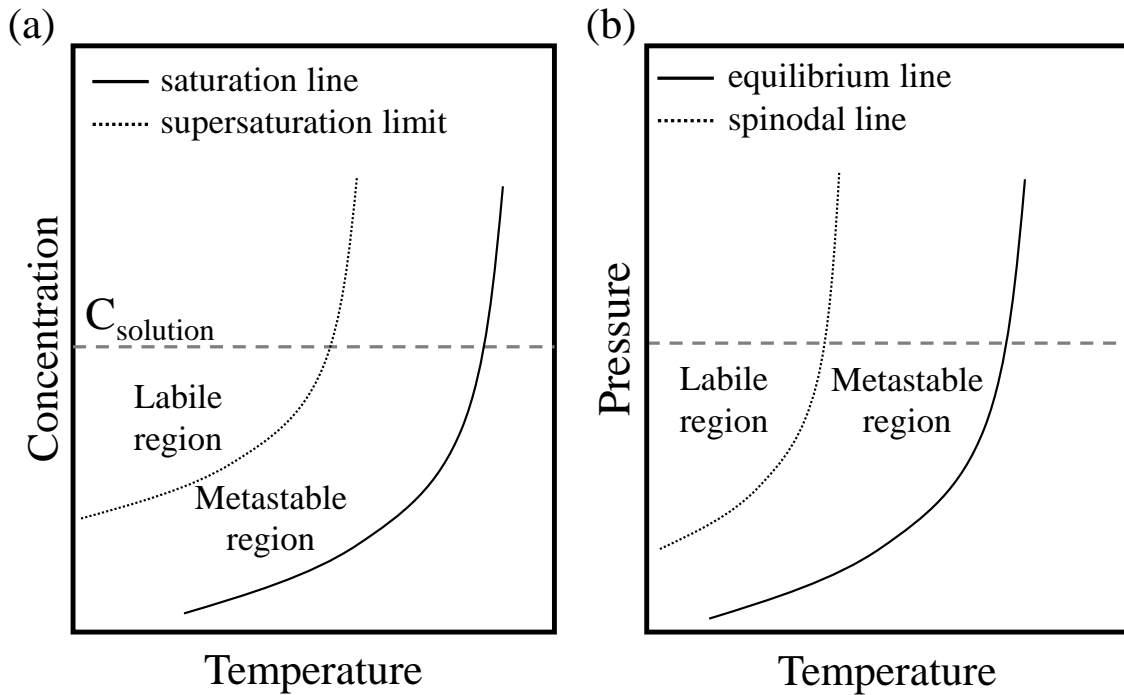


Figure 2.6: A comparison of hydrate formation and crystallization phenomena. (a) The crystallization process of a solution with a general concentration ($C_{solution}$) is shown by the dashed horizontal line. The solid black line represents the saturation curve, which separates the dissolved solute (right side) from the metastable region (left side). (b) The hydrate formation process, the solid black line represents the hydrate stability curve, and the zone within the hydrate domain is thermodynamically favorable for hydrate formation. Adapted from SLOAN e KOH (2008).

However, if the solution is cooled to the region left of the equilibrium line, the solvent contains more dissolved solute than can be accommodated. This zone between the saturation curve and supersaturated limit curves is called the metastable or supersaturated region.

Spontaneous crystallization is unlikely in the supersaturated region; however, growth may occur in the case of a disturbance (SLOAN e KOH, 2008). Beyond the supersaturation limit, spontaneous salt precipitation from the solution occurs in the unstable or labile region. Hydrates do not have a spinodal line as illustrated by Figure 2.6 (b), but the

literature suggests that nucleation occurs in the labile region due to the high driving force (SLOAN e KOH, 2008).

Similarly, hydrate formation comprises nucleation and growth stages, which are described in this chapter. The concept of subcooling as a driving force is crucial in understanding hydrate formation. Subcooling refers to the temperature difference between hydrate equilibrium and the current operating condition, maintaining a constant pressure ($\Delta T_{sub} = T_{eq}^{hyd} - T$) (ARJMANDI *et al.*, 2005, VYSNIAUSKAS e BISHNOI, 1983).

Under subcooling conditions, water molecules display unusual behavior. The water is considered subcooled when it exists in the liquid phase at temperatures below the freezing point. In such conditions, water is called metastable, which means a non-equilibrium condition that exists for an extended period (SLOAN e KOH, 2008).

At low temperatures, water molecules exhibit reduced entropy and increased volume, unlike other substances. Furthermore, natural gas solubility experiments in water demonstrate a decrease in entropy (SLOAN e KOH, 2008).

These observations relate to water molecules not forming bonds with guest components, causing local disruptions in the solution. As a result, the water molecules reorganize into small cages surrounding the solute (KE *et al.*, 2019, SLOAN e KOH, 2008).

The degree of lattice structuring and the solubility of guest molecules are influenced by temperature and pressure. According to MAKOGON (2010), one volume of methane hydrate at 0°C and 26bar contains 164 volumes of gas. This information supports the reason why the solubility of guest molecules increase in water solutions.

2.3.3 Nucleation

The nucleation stage is a dynamic and stochastic process occurring at a molecular level, which makes it challenging to observe experimentally (CUI *et al.*, 2019, KE *et al.*, 2019, SLOAN e KOH, 2008). During nucleation, the crystal nuclei overcome the free energy barrier and reach a critical size that is energetically favorable for continuous growth.

There are two types of nucleation: homogeneous (HON) and heterogeneous (HEN). HON is a solidification process without impurities, involving only the solute and nuclei crystals. On the other hand, HEN occurs in the presence of impurities, interfaces, and foreign particles or surfaces.

Consequently, HEN requires fewer molecules to reach the critical site and has a lower free energy barrier than HON (KE *et al.*, 2019, SLOAN e KOH, 2008). The literature suggests that HEN occurs more frequently in industrial processes (SANZ *et al.*, 2013, SLOAN e KOH, 2008).

Two methodologies are usually employed to study hydrate nucleation: (1) maintaining constant temperature and degree of subcooling, and (2) conducting constant cooling experiments. The subcooling is the usual nucleation's driving force (ARJMANDI *et al.*,

2005, VYSNIAUSKAS e BISHNOI, 1983); however, some studies have also used free Gibbs energy (ANKLAN e FIROOZABADI, 2004, SLOAN e KOH, 2008) and saturation degree (KASHCHIEV e FIROOZABADI, 2002) as alternatives.

Concerning hydrates formation in offshore pipelines, the nucleation stage within the hydrate domain is assumed to be instantaneous once the critical subcooling is achieved – a reported value above 3.5K (BOXALL *et al.*, 2009, TURNER *et al.*, 2005, ZERPA *et al.*, 2012). Given this assumption, the modeling description of nucleation falls outside the scope of this work. More details on the nucleation mechanism and other aspects can be found in KE *et al.* (2019).

2.3.4 Hydrate growth

After nucleation, the crystals that have formed initiate the growth stage. During this stage, a massive accumulation of nuclei can potentially lead to hydrate plugging. This phenomenon may be governed by surface mechanisms such as kinetic rates (AL-OTAIBI *et al.*, 2010, BASSANI *et al.*, 2019, CLARKE e BISHNOI, 2005, ENGLEZOS *et al.*, 1987a,b, LEKVAM e RUOFF, 1993, TURNER *et al.*, 2005, VYSNIAUSKAS e BISHNOI, 1983, 1985), mass transfer, heat transfer (GONG *et al.*, 2010, SHI *et al.*, 2011, ZERPA *et al.*, 2012), or a combination of these mechanisms.

The growth of hydrates was investigated through pioneer studies that carried out isothermal and isobaric experiments in semi-batch stirred tank reactors (ENGLEZOS *et al.*, 1987a,b, VYSNIAUSKAS e BISHNOI, 1983, 1985). These experiments were conducted in water-dominated systems, utilizing methane and ethane gas hydrates or a mixture of both.

Eq. (2.7) presents the semi-empirical kinetic model proposed by VYSNIAUSKAS e BISHNOI (1983, 1985). This model is based on an Arrhenius-type reaction rate, which is described as a function of the total surface area of the gas-water interface, the water and gas monomers at the interface, and the concentration of the critical clusters:

$$r = LA_s \exp\left(-\frac{\Delta E_a}{RT}\right) \exp\left(-\frac{c_1}{\Delta T_{sub}^{c_2}}\right) P^\gamma \quad (2.7)$$

where L is a lumped pre-exponential constant, A_s is the surface area, ΔE_a is the activation energy, c_1 and c_2 are arbitrary constants to account for the effects of subcooling on the rates, ΔT_{sub} is the subcooling temperature, and γ represents the overall reaction order concerning the pressure of the system.

The second exponential term in Eq. (2.7) represents the concentration of the critical cluster, which is based on a Boltzmann distribution relation applicable to any crystallization process. The concentration of water and gas monomers at the interface depends on temperature and pressure.

The model prediction was limited to the experimental pressure and temperature ranges (VYSNIAUSKAS e BISHNOI, 1983, 1985). Lower experimental rates presented the most significant errors, suggesting that the reaction was controlled by forming clusters at the interface.

Further, ENGLEZOS *et al.* (1987a,b) proposed a model based on the crystallization theory coupled with the two-film theory for gas absorption into the liquid bulk phase. The authors assumed that the growth of hydrate particles is composed of two steps: (1) the transportation of gas molecules to the bulk liquid phase, and (2) gas molecules are incorporated into the cages through an absorption process at the hydrate interface.

The model's driving force is the difference between the gas fugacity and the three-phase equilibrium fugacity. The rate of growth per particle is shown in Eq. (2.8):

$$\left(\frac{dn_i}{dt}\right)_p = K^* A_s (f_i^b - f_i^{eq}) \quad (2.8)$$

and

$$\frac{1}{K^*} = \frac{1}{k_r} + \frac{1}{k_d} \quad (2.9)$$

where dn_i/dt is the number of gas molecules consumed per second, K^* is the hydrate formation growth constant, f_i^b is the fugacity of component i in the bulk liquid, f_i^{eq} is the equilibrium fugacity of component i in the liquid at the hydrate interface, k_r is the reaction rate constant (absorption process), and k_d is the mass transfer coefficient through the film around the particle (diffusion process).

The Center for Hydrates Research at the Colorado School of Mines (CSM) developed two models for oil-dominated systems (CSMHyK), which were incorporated into the standard multi-phase flow simulator *OLGA*® (BOXALL *et al.*, 2009, TURNER *et al.*, 2005, ZERPA *et al.*, 2012). The first CSMHyK model utilizes first-order kinetics defined by Eq. (2.10) (TURNER *et al.*, 2005):

$$\frac{dm_{gas}}{dt} = -uk_1 \exp\left(\frac{k_2}{T_{sys}}\right) A_s (\Delta T_{sub}) \quad (2.10)$$

where $\frac{dm_{gas}}{dt}$ is the gas consumption rate during hydrate formation, u is the scaling factor parameter, k_1 and k_2 are the intrinsic kinetic rate constants, T_{sys} is the system temperature, and A_s is the surface area between the water and oil phases.

The values for reaction constants were regressed from experimental data for methane and ethane gas consumption rates (ENGLEZOS *et al.*, 1987a,b, VYSNIAUSKAS e BISHNOI, 1983, 1985). The reaction rate calculated from laboratory data differed from the results obtained in flow loop facilities. This discrepancy arose because the data were obtained in water-dominated systems and assumed sI structure.

The scaling factor parameter adjusted the consumption rate from a water-dominated

to an oil-dominated system (TURNER *et al.*, 2005). Furthermore, the literature suggested that the oil-water interface introduces mass and heat transfer resistance to the process (TURNER *et al.*, 2005).

Despite these limitations, the first-order rate kinetic model was effectively applied to validate experimental data on hydrate formation in both water- (RAO, 2013) and gas-dominated systems (WANG *et al.*, 2018b). The simplicity of this model makes it an attractive starting point for incorporating hydrate formation prediction into multi-phase flow models for various system dominances.

Multi-phase and multi-component systems bring additional relevance to heat transfer and mass transfer resistances. The second model developed by CSM, known as the Shrinking Core Model, is illustrated in Figure 2.7.

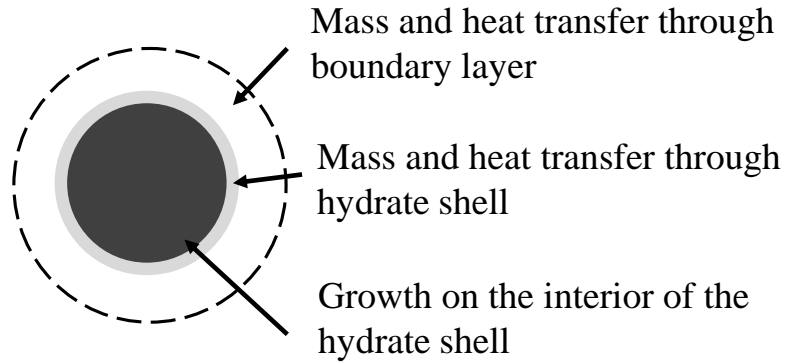


Figure 2.7: Mechanisms involved in hydrate growth according to the Shrinking Core Model. The arrows indicate where each mechanism exerts a significant influence on the hydrate growth process. Adapted from ZERPA *et al.* (2012).

After the nucleation stage, a hydrate shell forms and hydrate growth can be governed by either mass or heat transfer within the shell, or by the boundary layer surrounding the particle (ZERPA *et al.*, 2012). The slowest driving force in the process determines the rate of hydrate growth.

There are four equations to calculate the external and internal mass and heat resistances in oil-dominated systems (ZERPA *et al.*, 2012):

1. External heat particle resistance:

$$\left(\frac{dm_{gas}}{dt}\right)_{ext,heat} = h_{heat}A_s\Delta T_{sub} \left(\frac{HYDX_{gas}MA}{HYDX_{gas}MA + HYDX_{water}MA}\right) \quad (2.11)$$

2. Internal heat diffusion across hydrate shell:

$$\left(\frac{dm_{gas}}{dt}\right)_{int,heat} = \frac{k_{comp}A_s\Delta T_{sub}}{\delta(r_p/r_w)\Delta H} \left(\frac{HYDX_{gas}MA}{HYDX_{gas}MA + HYDX_{water}MA}\right) \quad (2.12)$$

where k_{comp} is the hydrate shell heat transfer coefficient with porosity ε , given by

the following equation, which assumes the pores are filled with water:

$$k_{comp} = \varepsilon k_{water} + (1 - \varepsilon)k_{hyd} \quad (2.13)$$

3. External mass particle resistance:

$$\left(\frac{dm_{gas}}{dt} \right)_{ext, mass} = k_{mass} A_s (C_{bulk} - C_{eq}) \quad (2.14)$$

4. Internal mass diffusion across hydrate shell:

$$\left(\frac{dm_{gas}}{dt} \right)_{ext, mass} = \frac{D_A A_s}{\delta (r_p / r_w)} (C_{bulk} - C_{eq}) \quad (2.15)$$

where k_{mass} is the mass transfer coefficient, h_{heat} is the heat transfer coefficient, C_{bulk} is the guest hydrate concentration in the bulk phase, C_{eq} is the guest hydrate concentration in the water phase in the presence of hydrates, $HYDX_{gas}$ and $HYDX_{water}$ are the concentration of gas and water in the hydrate phase, respectively, D_A is the gas molecules' diffusivity in the hydrate shell, δ is the shell thickness, r_p and r_w are the particle and water core radius, respectively.

These models do not combine the formation mechanisms and only consider methane hydrate formation. The Shrinking Core Model also presents an inconsistency in the mass balance. The quasi-equilibrium hypothesis assumes that the methane concentration at the water-hydrate and hydrate-oil interfaces is the same (FERREIRA, 2018). Nevertheless, the solubility of gas differs between oil and aqueous solutions.

An analogous Hydrate Shell Model utilized the previous mass transfer resistances. However, the mathematical equation for heat transfer in this model is not well-described (GONG *et al.*, 2010, SHI *et al.*, 2011). The internal and external mass resistances were combined into the intrinsic kinetic rate (GONG *et al.*, 2010, SHI *et al.*, 2011).

The gas consumption rate, in the Hydrate Shell Model, is calculated using the difference in fugacity as the driving force. The methane fugacity is redefined as a function of the gas concentration and Henry's law constant (GONG *et al.*, 2010). The gas consumption at the interface is given by Eq. (2.16):

$$\left(\frac{dn_{gas}}{dt} \right) = 4\pi R_c^2 K H \frac{(C_c - C_{eq})}{C_{wo}} \quad (2.16)$$

where $\frac{dn_{gas}}{dt}$ is the consumed gas molar rate, R_c is the radius of the water droplet, H is the Henry constant, K is the a combined rate parameter given by ENGLEZOS *et al.* (1987a,b), C_c , C_{eq} , and C_{wo} are, respectively, the concentration of methane in the aqueous phase, the concentration of methane in the hydrate phase, and water concentration in the aqueous

phase.

Alternatively, for a mixture of methane, ethane, and propane hydrates, the fugacity was rewritten in terms of the concentration parameter given by Eq. (2.17) (SHI *et al.*, 2011):

$$f_i = \frac{\phi_i y_i P}{C_i^o} C_i^w = \Omega_i C_i^w \quad (2.17)$$

where ϕ_i is the fugacity coefficient of the gas i , y_i is the molar fraction of gas i ; C_i^w and C_i^o are, respectively, the concentration of gas i in the aqueous and oil phase. Then, the intrinsic rate was combined with the internal mass transfer as follows (SHI *et al.*, 2011):

$$\left(\frac{dn_{gas}}{dt} \right) = 4\pi R_c^2 \sum_{i=1}^N [k_i (\Omega_i C_i^w - \Omega_i^{eq} C_i^{eq})] \quad (2.18)$$

where k_i is the rate constant of i component. The rate constant and diffusivity values were obtained from experimental data and assumed to be equal for all components.

The author adopted a quasi-equilibrium assumption for the mass balance at the surface (GONG *et al.*, 2010, SHI *et al.*, 2011). With this assumption, it becomes possible to express the inner diameter in terms of diffusivity and concentration given a specific external diameter. The external consumption presumes that internal and external shell diameters are interconnected through capillaries filled with water, which is instantaneously converted into hydrates (SHI *et al.*, 2011).

All previous models consider the formation of a hydrate shell around water droplets. Furthermore, the accumulation process occurs through a water bridge between the hydrate particle or nuclei, as illustrated in Figure 2.4. BASSANI *et al.* (2019) considered the hydrate shell model as “static” because it neglects the rotation and vibration movement of particles within the flow.

Using a new interpretation of experimental observations involving hydrate formation, BASSANI *et al.* (2019) proposed a sponge-like structure, rather than a shell, to explain the hydrate growth stage. This model suggests that a “dynamic” continuous flow forms a highly porous and hydrophilic hydrate particle, also called a sponge-like structure, as illustrated in Figure 2.8.

The classification of particles as “wet” and “dry” depends on whether water fills the capillaries. Without surfactant, water is expelled from the porous particle (wet) due to capillary forces; however, in the presence of surfactant, the oil phase penetrates the capillaries, preventing interaction between particles (dry).

For wet particles, the accumulation process occurs on a particle scale, as shown in Figure 2.9. After the collision, a water bridge is formed between the porous particles. If they remain together for a sufficient time, the connecting bridge crystallizes, resulting in particle agglomeration.

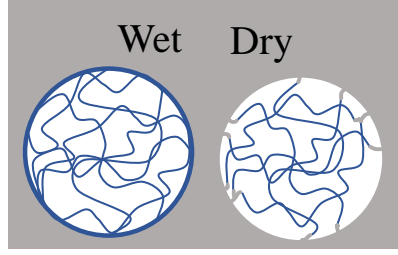


Figure 2.8: Schematic representation of the sponge-like structure of hydrate particles, as proposed by BASSANI *et al.* (2019). The classification of particles as "wet" and "dry" depends on whether water fills the capillaries.

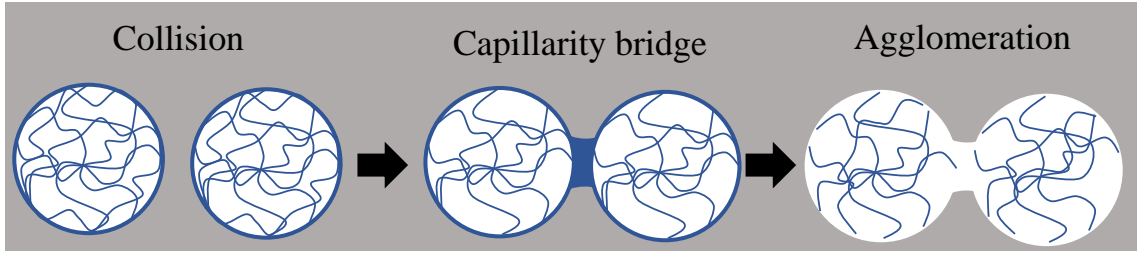


Figure 2.9: Illustration of the accumulation process in the sponge-like structure model. The figure shows the formation of a water bridge between particles after the collision.

The phenomenological model for water- and oil-dominated systems is limited by gas consumption in the capillary walls and a decrease in porosity over time, as demonstrated in Eq. (2.19). The authors assumed an sI structure and a single methane hydrate. The model was validated using flow loop data from a mixture containing methane, with a 32% WC, and light oil.

$$-\frac{dn_{gas}}{dt} = k_1 \frac{WC V_l}{r_p} \sqrt{H_w D_w} (f_g - f_{eq}) \exp \left[-k_2 (n_H + 1) \frac{M_{hyd}}{\rho_{hyd}} (f_g - f_{eq}) t \right] \quad (2.19)$$

where WC is the water cut, V_l is the liquid volume (*i.e.*, water and oil), r_p is the particle size, H_w is the Henry constant of the gas inside water, D_w is the gas diffusivity in water, $(f_g - f_{eq})$ is the driving force, f_g is the gas fugacity at system temperature and pressure, f_{eq} is the gas fugacity at the equilibrium pressure related to system temperature, ρ_{hyd} is the hydrate density, n_H is the hydration number, M_w is the average molar mass of water, and t is the time.

The parameters k_1 and k_2 are given by Eq. (2.20) and Eq. (2.21). They include microscale parameters related to: gas distribution inside the continuous phase (∞_p), initial porosity of hydrates (ϵ_{in}), proportionality constant of crystallization law (k_i), capillary radius (r_c), and birth-to-death ratio of capillaries (λ).

$$k_1 = 6\infty_p \epsilon_{in} \sqrt{\frac{k_i}{2r_c}} \quad (2.20)$$

$$k_2 = (1 - \lambda) \frac{k_i}{r_c} \quad (2.21)$$

These parameters are obtained from the asymptote and curve of experimental data on gas consumption over time. The values for a light oil continuous flow, reported by BAS-SANI *et al.* (2020), were $k_1 = 7.76 \times 10^{-4} \text{ (mol/(m}^2\text{sPa))}^{1/2}$ and $k_2 = 1.56 \times 10^{-6} \text{ mol/(m}^2\text{sPa)}$.

2.3.5 Hydrate slurry

An agglomeration model proposed by CAMARGO e PALERMO (2002) is based on a balance between cohesion and shear forces. The first is an attractive force that promotes an increase in the size of hydrate aggregates, while the latter is a disruptive force that acts to break up these aggregates.

Initially, it was assumed that the particle was spherical with a diameter of $40 \mu\text{m}$ (ZERPA *et al.*, 2012). Further, BOXALL *et al.* (2012) proposed a method to predict the particle diameter from Reynolds and Weber numbers, given by Eq. (2.22) and Eq. (2.23), respectively:

$$Re = \frac{D_p U \rho_o}{\mu_o} \quad (2.22)$$

$$We = \frac{D_p U^2 \rho_o}{\sigma} \quad (2.23)$$

The particle diameter is determined by Eq. (2.24) depending on the type of flow sub-range:

$$d_p = \begin{cases} 0.063 D_p We^{-3/5}, & We < 0.067 Re^{5/4}, \text{ inertial sub-range} \\ 0.016 D_p^{1/2} We^{-1}, & \text{otherwise, viscous sub-range} \end{cases} \quad (2.24)$$

where Re is the Reynolds number, We is the Weber number, D_p pipe internal diameter, U is the fluid velocity, ρ_o is the density of the oil phase, μ_o is the oil viscosity, σ is the oil-water interfacial tension, and d_p is the particle diameter.

Once hydrate particles form in the oil phase via water droplets, these particles can agglomerate and form high hydrate masses. The diameter of the aggregated particle can be calculated using Eq. (2.25) (CAMARGO e PALERMO, 2002):

$$\left(\frac{d_A}{d_p}\right)^{(4-f)} = - \frac{F_a \left[1 - \frac{\alpha_{hyd}}{\alpha_{hyd}^{max}} \left(\frac{d_A}{d_p}\right)^{(3-f)} \right]^2}{d_p^2 \mu_0 \tau \left[1 - \alpha_{hyd} \left(\frac{d_A}{d_p}\right)^{(3-f)} \right]} \quad (2.25)$$

where d_A is the particle agglomerate diameter, F_a is the inter-particle cohesion force (assumed to be equal to 50 mN/m (ZERPA *et al.*, 2012)), α_{hyd} is the hydrate particle volume fraction, α_{hyd}^{max} is the maximum volume fraction (assumed to be equal to 4/7 (TURNER

et al., 2005, ZERPA *et al.*, 2012)), τ is the shear rate, and f is the fractal dimension – assumed to be equal to 2.5 (TURNER *et al.*, 2005, ZERPA *et al.*, 2012).

Figure 2.10 compares the size of the particle diameter (d_p) and the agglomerate diameter (d_A). The particle diameter is assumed to be equal to the water droplet diameter dispersed in the oil continuous phase, and the agglomerate diameter is the result of the balance between cohesion and shear forces during the massive accumulation of hydrate particles formed and reacting nuclei.

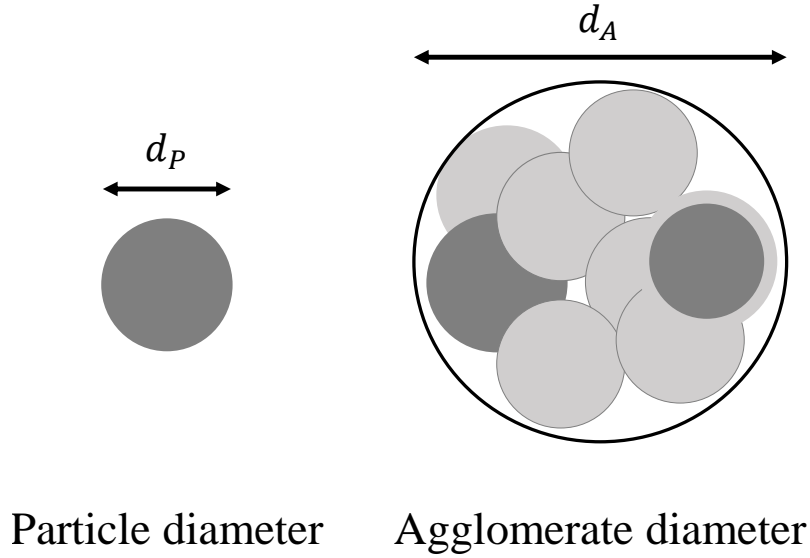


Figure 2.10: Conceptual illustration comparing the predicted particle diameter (d_p) and agglomerate diameter (d_A) using the agglomeration model for a methane hydrate system.

For the Shrinking Core Model, a correlation given by Eq. (2.26) calculates the cohesion force as a function of the temperature:

$$Fa = \frac{d_p}{2} [0.0017 - \Delta T_{sub} + 0.0007] \quad (2.26)$$

The plugging phenomenon occurs when the maximum viscosity is reached. Beyond this point, a plug may form, potentially blocking a production line. This phenomenon was calculated using the model of relative viscosity of the suspension (BOXALL *et al.*, 2009, TURNER *et al.*, 2005, ZERPA *et al.*, 2012), as shown in Eq. (2.27):

$$\mu_r = \frac{1 - \alpha_{hyd}^{eff}}{\left(1 - \frac{\alpha_{hyd}^{eff}}{\alpha_{hyd}^{max}}\right)^2} \quad (2.27)$$

where μ_r is the relative viscosity of the hydrate slurry, and α_{hyd}^{eff} is the effective hydrate

volume fraction obtained from Eq. (2.28):

$$\alpha_{hyd}^{eff} = \alpha_{hyd} \left(\frac{d_A}{d_P} \right)^{(3-f)} \quad (2.28)$$

Analysis of hydrate slurry rheology, drawing upon both experimental data and modeling, has observed a significant increase in relative viscosity for hydrate volume fractions up to 40%–50% (MAJID *et al.*, 2018), a phenomenon not predicted by Eq. (2.25).

This observation indicates potential areas of improvement, including the incorporation of particle shape and roughness effects, as well as the development of a more precise method for estimating the particle effective volume fraction (MAJID *et al.*, 2018).

2.4 Multi-phase flow in pipelines

Modeling hydrate formation in pipelines requires predicting the interaction between gas, liquid, and solid phases in flow. This is complex due to the number of co-occurring phenomena.

Mass, momentum, and energy conservation equations are combined with constitutive equations to describe the essential effects of the multi-phase flow. A suitable tool must be able to predict pressure, temperature, and velocity variables in the pipeline using governing and constitutive equations.

The multi-phase flow model can be applied for both steady-state and transient analyses. Steady-state analysis enables the investigation of a system's production performance and operation. In contrast, transient analysis involves monitoring operations and developing strategies to ensure optimal production levels.

The following section reviews the main multi-phase flow models available in the literature and their application in predicting hydrate formation in pipelines. This work only applies steady-state analyses; none of the following equations include the transient terms.

2.4.1 Multi-phase flow models

Two-Fluid Model (TFM) comprises six differential conservation equations and three algebraic equations. It is considered the most detailed bi-phase flow model (GUEDES, 2023). Each phase (*i.e.*, liquid and gas) has mass, momentum, and energy equations, as shown in Eq. (2.29) – Eq. (2.34):

Liquid phase conservation equation:

$$\frac{d(\alpha_l \rho_l U_l)}{dx} = -\Gamma_v \quad (2.29)$$

Vapor phase conservation equation:

$$\frac{d(\alpha_v \rho_v U_v)}{dx} = \Gamma_v \quad (2.30)$$

Liquid phase momentum equation:

$$\frac{d(\alpha_l \rho_l U_l^2)}{dx} = -\alpha_l \frac{dP}{dx} - \alpha_l \rho_l \sin(\theta) - F_{lw} + \Gamma_v U_{li} - F_i + F_{MV} \quad (2.31)$$

Vapor phase momentum equation:

$$\frac{d(\alpha_v \rho_v U_v^2)}{dx} = -\alpha_v \frac{dP}{dx} - \alpha_v \rho_v \sin(\theta) - F_{vw} - \Gamma_v U_{vi} + F_i - F_{MV} \quad (2.32)$$

Liquid phase energy equation:

$$\frac{d(\alpha_l \rho_l U_l h_l)}{dx} = -\Gamma_v h_l + Q_{lw}(1 - \gamma_l) + \alpha_l U_l \frac{dP}{dx} \quad (2.33)$$

Vapor phase energy equation:

$$\frac{d(\alpha_v \rho_v U_v h_v)}{dx} = \Gamma_v h_v + Q_{vw}(1 - \gamma_v) + \alpha_v U_v \frac{dP}{dx} \quad (2.34)$$

where α is the phase void fraction, ρ is the density, U is the velocity, θ is the inclination angle, Γ_v is the vapor mass transfer rate, F_{lw} and F_{vw} are the friction volumetric forces, F_{li} and F_{vi} are the frictional and interfacial drag volumetric forces, F_{lMV} and F_{vMV} are the virtual mass forces, h is the enthalpy, γ_l and γ_v are the fraction of heat exchange with the wall that results in the heat transfer Q_{lw} and Q_{vw} , respectively. The subscripts l , v , li , lv refer, respectively, to liquid phase, vapor phase, liquid interface, and vapor interface.

The model is completed by interfacial balance equations shown in Eq. (2.35) – Eq. (2.37):

$$\Gamma_l + \Gamma_v = 0 \quad (2.35)$$

$$-\Gamma_l U_{li} + \Gamma_v U_{vi} = 0 \quad (2.36)$$

$$-\gamma_v Q_{vw} - \gamma_l Q_{lw} + \Gamma_v (h_v - h_l) = 0 \quad (2.37)$$

The heat exchange between the phases and the wall (Q_{lw} and Q_{vw}) are calculated as shown in Eq. (2.38):

$$Q_{fn} = \begin{cases} Q_{lw}, & \Gamma_v > 0 \\ Q_{vw}, & \Gamma_v < 0 \end{cases} \quad (2.38)$$

The variable γ_l and γ_v are calculated based on the value of Γ_v , as shown in Eq. (2.39) and Eq. (2.40), which uses the energy interfacial balance equation.

$$\gamma_l = \begin{cases} \frac{\Gamma_v(h_v - h_l)}{Q_{lw}}, & \Gamma_v > 0 \\ 0, & \text{otherwise} \end{cases} \quad (2.39)$$

$$\gamma_v = \begin{cases} \frac{\Gamma_v(h_v - h_l)}{Q_{vw}}, & \Gamma_v < 0 \\ 0, & \text{otherwise} \end{cases} \quad (2.40)$$

The interfacial average velocities, U_{li} and U_{vi} , are described by Eq. (2.41):

$$U_{vi} = U_{li} = U_i = \begin{cases} U_l, & \Gamma_v > 0 \\ U_v, & \Gamma_v < 0 \end{cases} \quad (2.41)$$

The Drift-Flux Model (DFM) consists of four differential conservation equations and one constitutive kinematic equation concerning the mean drift velocity. The mixture of liquid and gas phases has equations for mass, momentum, and energy balances, represented respectively by Eq. (2.42), Eq. (2.44), and Eq. (2.45). Additionally, there is a mass equation for the vapor phase and a constitutive kinematic equation, represented respectively in Eq. (2.43) and Eq. (2.46).

Mixture mass balance:

$$\frac{d(\rho_m U_m)}{dx} = 0 \quad (2.42)$$

Vapor phase mass balance:

$$\frac{d(\alpha_v \rho_v U_m)}{dx} = \Gamma_v - \frac{d}{dx} \left(\frac{\alpha_v \rho_v \rho_l}{\rho_m} \hat{v}_v^{dft} \right) \quad (2.43)$$

Mixture momentum balance:

$$\frac{d(\rho_m U_m^2)}{dx} = -\frac{dP}{dx} - \rho_m g \sin(\theta) - F_{mw} - \frac{d}{dx} \left(\frac{\alpha_v \rho_v \rho_l}{\alpha_l \rho_m} (\hat{v}_v^{dft})^2 \right) \quad (2.44)$$

Mixture energy balance:

$$\frac{d(\rho_m U_m h_m)}{dx} = Q_{fn} - \frac{d}{dx} \left[\frac{\alpha_v \rho_v \rho_l}{\rho_m} (h_v - h_l) \hat{v}_v^{dft} \right] + \frac{dP}{dx} \left[U_m + \frac{\alpha_v (\rho_l - \rho_v)}{\rho_m} \hat{v}_v^{dft} \right] \quad (2.45)$$

Empirical constitutive equation:

$$\hat{v}_v^{dft} = \langle \hat{v}_v^{dft} \rangle_\alpha + (C_0 + 1) U_m \quad (2.46)$$

where F_{mw} is the frictional pressure loss, Q_{fn} is the heat exchange rate between the fluid and the neighborhood, \hat{v}_v^{dft} is the slip velocity of the vapor phase in relation to the mixture,

the subscript m refers to the mixture, and $\langle \hat{v}_v^{dft} \rangle_\alpha$, and C_0 are model parameters.

The relationships between phase velocities, mixture velocity, and drift slip velocity are shown in Appendix B. Frictional loss is described by an empirical model commonly found in the literature (RAO, 2013, ZERPA, 2013); detailed equations can be found in Appendix B. A detailed description of the TFM and DFM can be found in TEIXEIRA (2016).

A single-phase liquid flow is expected in oil-dominated pipelines (*i.e.*, wellhead and flowline) because the pressure is higher than the fluid bubble point. Multi-phase flow occurs near the riser region due to decreased temperature and pressure. Since the flow starts monophasic, a single-flow model should be incorporated (GUEDES, 2023, GÓES *et al.*, 2023). Eq. (2.47) – Eq. (2.49) present the mass, momentum, and energy conservation equations for a single liquid flow:

Single liquid mass balance:

$$\frac{d(\rho_l U_l)}{dx} = 0 \quad (2.47)$$

Single liquid momentum balance:

$$\frac{d(\rho_m U_m^2)}{dx} = -\frac{dP}{dx} - \rho_l g \sin(\theta) - F_{mw} \quad (2.48)$$

Single liquid energy balance:

$$\frac{d(\rho_l U_l h_l)}{dx} = Q_{fn} + U_l \frac{dP}{dx} \quad (2.49)$$

The transition between single- and two-phase flow models is governed by the vaporized mass fraction, β_w (GUEDES, 2023, GÓES *et al.*, 2023). β_w is obtained in the flash calculations by multiplying the vapor separation factor and the mixture molar weight ratio (GUEDES, 2023).

Eq. (2.50) summarizes the shift condition applied in the constitutive kinetic equation:

$$\hat{v}_v^{dft} = \begin{cases} \langle \hat{v}_v^{dft} \rangle_\alpha + (C_0 + 1), & \beta_w > 0 \\ 0, & \beta_w \leq 0 \end{cases} \quad (2.50)$$

Eq. (2.51) summarizes the shift condition applied in friction loss calculation (see Appendix B):

$$F_{mw} = \begin{cases} \phi_v^2 \left(\frac{dP}{dx} \right)_v, & \beta_w > 0 \\ \left(\frac{dP}{dx} \right)_l, & \beta_w \leq 0 \end{cases} \quad (2.51)$$

The heat exchange between the fluid and its neighborhood is described by Eq. (2.52) (GUEDES, 2023, GÓES *et al.*, 2023):

$$Q_{fn} = 4 \frac{U_{heat}(T_{neigh} - T)}{D_p} \quad (2.52)$$

where T is the temperature, U_{heat} is the overall heat transfer coefficient, and the subscript *neigh* refers to neighborhood temperature (for seawater, we assumed T_{neigh} equal 277.15K).

The vapor mass generation is evaluated by Eq. (2.53) (GUEDES, 2023, GÓES *et al.*, 2023):

$$\Gamma_v = \rho_m U_m \frac{d\beta_w}{dx} \quad (2.53)$$

Most literature on multi-phase flow with hydrates applies the Hydrodynamic Slug Flow Model (HSM). This model considers an intermittent flow of unit cells, as illustrated in Figure 2.11. Unit cells take into account a periodic flow in time and space, comprising two zones: liquid slug (L_S) and elongated bubble (L_B). The combination of each unit cell's zone and three phases (*i.e.*, gas, liquid, and hydrate) can model different aspects of multi-phase flow in the pipeline.

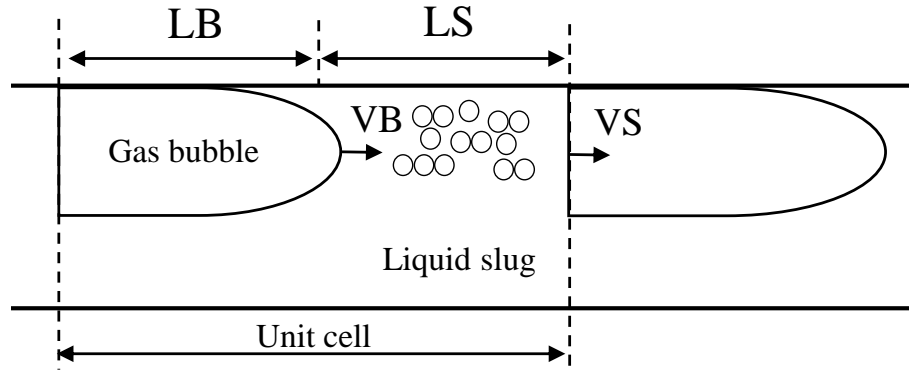


Figure 2.11: Representation of a unit cell and the mechanistic depiction of slug flows as applied in the Slug Flow Model.

The TFM and DFM described above balance the conservative equations through the phase void fraction. In HSM, the conservation equations are balanced using the holdup – the volume fraction occupied by the liquid or gas phase. This approach rewrites the equations by adding the sectional pipe area and the phase holdup.

BASSANI (2017) provides a comprehensive evaluation and application of HSM, which was classified based on the following factors: (1) the approach employed to achieve the modeling solution, (2) the use of steady-state or dynamic simulations, and (3) the pipe inclination, which was considered in the application.

TFM, DFM, and HSM require correlations that describe the phases' flow patterns. The flow pattern represents the type of interaction between liquid and gas phases. Empirical correlations and mechanistic models predict the flow pattern and complete the equations system of multi-phase models. However, the models' validity depends on pipe inclination

and the experimental conditions of obtained data for the flow pattern (TEIXEIRA, 2016).

The TFM is suitable for predicting dispersed flow regimes and is useful for studying hydrate growth in these types of flow regimes. The HSM, on the other hand, accounts for the complex interaction between liquid and gas phases in slug flow. It is particularly helpful in studying the risk of hydrate formation and deposition in an intermittent slug flow. Meanwhile, the DFM is a simplified model compared to the others and is ideal for homogeneous flow regimes where the phases are well-mixed.

Despite its simplicity, this work aims to apply the DFM to predict hydrate formation, taking into account its advantages such as requiring fewer equations and assumptions, making it easier to implement and solve numerically. It also requires less computational effort than other complex models and uses fewer parameters, making it more robust for practical applications.

Additionally, although the DFM is suitable for homogeneous flow regimes, the distribution parameter and drift velocity can be adjusted to predict the dispersed flow. Finally, the kinetic model can be integrated with mass- and heat-transfer terms in the mixture conservation equations.

2.4.2 Hydrodynamic models with hydrates

OLGA[®] is the O&G industry-standard tool for transient multi-phase flow simulation (KOH *et al.*, 2011b). It uses the TFM and applies a numerical solution scheme that spatially discretizes the pipeline into multiple control volumes. This well-known software program applies the rigorous bi-phase model and contains a separate module that analyzes hydrate formation in oil- and water-dominated systems using the CSM models.

In GONG *et al.* (2010), the one-dimensional TFM applied the holdup to measure hydrate formation using the Hydrate Shell Model shown in Eq. (2.16). The research was limited to a horizontal pipe and stratified flow simulation, considering only methane hydrate formation.

An extension of this work included the mixture of gas hydrates consumed during hydrate formation and defined the concentration parameter as shown in Eq. (2.17) (SHI *et al.*, 2011). The results suggest that the diffusivity parameter in the mass transfer mechanism is critical in predicting hydrate formation. The authors did not apply agglomeration or deposition models.

The HSM was applied using slip velocity to complete the equation describing the dynamic multi-phase model with hydrate formation in oil- (ZERPA, 2013) and water-dominated systems (RAO, 2013). ZERPA (2013) considered only the liquid-gas slip velocity, assuming no slip between the liquid-hydrate phases.

In contrast, RAO (2013) used a flow pattern to describe the solid-particle interaction with the liquid phase and obtained the liquid-hydrate slip velocity as a function of hydrate

holdup. ZERPA (2013) and RAO (2013) used tables of fluid properties generated from thermodynamic software programs in their multi-phase models.

The first-order intrinsic kinetic rate shown in Eq. (2.10) was used to measure hydrate formation in ZERPA (2013) and RAO (2013). In ZERPA (2013), plugging risks were analyzed by considering pressure drop, hydrate volume fraction, and relative viscosity resulting from the agglomeration model mentioned in Section 2.3.3. RAO (2013) included the gas hydrate layer deposition on the pipeline surface in water-dominated systems.

The authors emphasized that reasonable multi-phase hydrodynamic and kinetic models are necessary to measure the hydrate fraction and its effects on flow temperature, pressure, and velocity. Their research was limited to methane gas hydrate and sI structure. Their work suggested the importance of mass and heat transfer in the model to predict the growth and deposition phenomena.

On the other hand, BASSANI (2017) presented a steady-state mechanical approach in HSM to simulate hydrate formation in oil-dominated systems. The simulation was limited to a horizontal pipe and slug flow patterns. Analytic expressions described the temperature, pressure, and heat transfer coefficient along the pipeline. This research only accounted for mass and heat transfer related to hydrate formation, ignoring vaporization. The liquid phase was assumed to be incompressible, and the gas phase used a real gas model.

BASSANI (2017) predicted the hydrate formation using the intrinsic kinetic model; the associated hydrodynamic model did not incorporate accumulation and deposition phenomena. It was assumed that water and hydrate phases were dispersed in the oil phase, thereby forming a homogeneous dispersion. The authors suggested that heterogeneous dispersion is required to analyze pressure drop induced by hydrate formation for hydrate volumetric fractions exceeding 13% (BASSANI, 2017).

In FERREIRA (2018), the TFM coupled with a population balance model, dynamically predicted hydrate formation in oil-dominated systems. The prediction was limited to the pipe section favorable to hydrate formation and not along the pipeline (FERREIRA, 2018).

The methodology assumed all phases were incompressible and neglected mass transfer between phases. This approach, using particle population, observed variation in pressure drops of around 170% due to hydrate formation (FERREIRA, 2018). The author did not include deposition prediction.

None of the available models were capable of combining intrinsic kinetic, heat, and mass resistances. However, they clarified the coexistence of mechanisms (GONG *et al.*, 2010, SHI *et al.*, 2011, ZERPA *et al.*, 2012), expanded the model for former mixtures in natural gas (SHI *et al.*, 2011), and suggested that higher WCs (ZERPA *et al.*, 2012) and diffusivity (GONG *et al.*, 2010, SHI *et al.*, 2011) strongly affect hydrate formation in oil-dominated systems.

Concerning FA steady-state analysis, TEIXEIRA (2016) compared different one-dimensional multi-phase flow models. The phase equilibrium conditions were calculated for a hydrocarbon mixture without hydrate formation. Regularization functions addressed the existing discontinuities in the transitions between the flow patterns (TEIXEIRA, 2016).

In TEIXEIRA (2016), a differential-algebraic equation (DAE) approach was used for the numeric solution rather than the usual marching algorithm. The Drift-Flux Model demonstrated superiority over the TFM, making the DFM an attractive option due to its simpler equations and faster performance (GÓES *et al.*, 2023, TEIXEIRA, 2016).

The authors proposed a dynamic solution using the transverse method of lines with the two-point backward method. A preliminary study indicated that the DAE proposal could provide efficient dynamic simulation (TEIXEIRA, 2016). However, the method for estimating the integration step requires improvement.

In the study by GUEDES *et al.* (2020), a one-dimensional homogeneous model was employed in conjunction with fluid characterization to design pipelines avoiding the hydrate-formation domain. The correlation used to calculate the pressure drop incorporated regularization functions proposed by TEIXEIRA *et al.* (2015). The pipeline insulation design strategies, applied to full-scale industrial conditions, demonstrated excellent concurrence with a standard software program commonly used in the O&G industry (GUEDES *et al.*, 2020).

DFM was applied in an iterative algorithm to fit operational conditions from offshore field data. Using fluid data and pipeline geometry information, the algorithm returns the pipe wall roughness, which fits the pressure and temperature drop corresponding to real-time operational conditions (GÓES *et al.*, 2023). Other works fitted the temperature profile by adjusting the overall heat transfer coefficient (RAO, 2013, ZERPA, 2013).

In GUEDES (2023), the DFM assisted the steady-state analysis that evaluated the temperature difference between the hydrate equilibrium and pipeline sections. The hydrodynamic model considered compressible phases, and the fluid properties were calculated using a methodology that agreed with the commercial software *Multiflash*TM. In addition, the three-phase flash calculation included hydrate stability analysis (GUEDES, 2023).

The kinetics of hydrate is a time-dependent phenomenon; the steady-state approach cannot observe the temporal deposition of hydrate in pipelines. However, this work aims to evaluate if the Drift-Flux Model set as a DAE system in steady state can predict the local effects of hydrate formation in oil-dominated pipelines. This work aims to contribute to the previous research, including the crystallization of gas hydrate under kinetic and thermodynamic aspects reviewed in this chapter.

The approach proposed in this work first obtained the fluid composition and hydrate stability curve using the methodology proposed in GUEDES (2015) and GUEDES (2023), respectively. The hydrodynamic model included the mass and heat phase transfer, allow-

ing a shift from single- to two-phase flow along the pipeline (GUEDES, 2023, GÓES *et al.*, 2023). This included the mass and heat effects due to vaporization, which are usually neglected in the literature simulating hydrate formation.

Modifications in the steady-state DFM were proposed to include the hydrate phase and properties. The DAE system was solved using the same methodology employed in TEIXEIRA (2016), GUEDES (2023), and GÓES *et al.* (2023). More details of the methodology applied are provided in the next chapter.

2.5 Fluid characterization

There are two pillars of FA: production chemistry and multi-phase flow modeling (BOMBA *et al.*, 2018). Production chemistry includes simulations and modeling techniques to obtain fluid characterization. Fluid characterization is required to perform any analyses in FA. This section presents the literature on flash calculations and methods to obtain the separation factors and composition of gas, aqueous, and oil phases.

This work required bi- and three-phase flash algorithms. The bi-phase flash, involving the oil liquid and gas phase, was combined with the hydrate equilibrium diagram mentioned in Section 2.2, while the three-phase flash returns the component compositions for each phase (*i.e.*, gas, aqueous, and oil), which are needed to obtain fluid properties.

2.5.1 Three-phase flash calculations

A three-phase flash algorithm was needed to obtain the component compositions for each phase, the vapor fraction, and the liquid ratio between the oil and aqueous phases. Phase equilibrium procedures available in the literature provide algorithms to obtain the fluid composition and each phase fraction from a known overall system composition, temperature, and pressure (ANDRADE, 1991, BALLARD e SLOAN, 2004a, GUEDES, 2023, GUPTA *et al.*, 1991, SEGTOVICH *et al.*, 2016).

Flash algorithms described the equilibrium condition using equality of fugacity of components in each phase (ANDRADE, 1991, GUEDES, 2023) or minimization of free Gibbs energy (BALLARD e SLOAN, 2004a, GUPTA *et al.*, 1991, SEGTOVICH *et al.*, 2016).

The free Gibbs energy criterion guarantees the global minimum, thereby facilitating the identification of stable phases in equilibrium. Although it is somewhat complex, the fugacity criterion is often preferred due to its rapid computation, making it an attractive alternative. On the other hand, additional criteria to analyze single and two-phase equilibrium remain indispensable (NELSON, 1987).

Both approaches used mass balance equations to describe the fractions of each component and phase. The vapor and liquid fractions can be included using separation factors

that inform the phases' volumetric fractions (ANDRADE, 1991, GUEDES, 2015).

The Rachford-Rice equations were used to couple the phase composition with separation factors (ANDRADE, 1991, GUEDES, 2023) or stability variables (BALLARD e SLOAN, 2004a, GUPTA *et al.*, 1991, SEGTOVICH *et al.*, 2016). The Newton-Raphson method is frequently used to accelerate convergence (BALLARD e SLOAN, 2004a, NELSON, 1987).

The mass balance, including separation factors to perform three-phase flash calculations, is described below for an oil-, aqueous-, and vapor-phase equilibrium (EL_oL_wV). The vapor phase is represented as V , and the liquid oil and aqueous phases are represented as L – the subscript o and w identify the phase rich in hydrocarbon and water, respectively.

Overall material balance:

$$L_o + L_w + V = F \quad (2.54)$$

Material balance for a three-phase flash:

$$x_i^o L_o + x_i^w L_w + y_i V = z_i F \quad (2.55)$$

Phases mole fractions relations:

$$\sum_{i=1}^n x_i^o = \sum_{i=1}^n x_i^w = \sum_{i=1}^n y_i = 1 \quad (2.56)$$

Relation between molar fractions and equilibrium constants:

$$y_i = K_i^o x_i^o = K_i^w x_i^w \quad (2.57)$$

Vapor separation factor:

$$\zeta = \frac{V}{F} \quad (2.58)$$

Liquid separation factor:

$$\beta = \frac{L_o}{L_o + L_w} \quad (2.59)$$

where the symbols ζ and β are the vapor and liquid separation factors, respectively. K_i , x_i , and y_i are, respectively, the equilibrium constant, liquid molar fraction, and the vapor molar fraction of component i .

The literature details all the steps to connect the mass balances, molar fractions, separations factors, and equilibrium constants (ANDRADE, 1991, GUEDES, 2023). The final equations are shown below:

Oil-phase mole fraction:

$$x_i^o = \frac{z_i}{\beta(1 - \zeta) + \frac{K_i^o}{K_i^w}(1 - \beta)(1 - \zeta) + K_i^o \zeta} \quad (2.60)$$

Aqueous-phase mole fraction:

$$x_i^w = \frac{z_i}{\frac{K_i^w}{K_i^o}\beta(1-\zeta) + (1-\beta)(1-\zeta) + K_i^w\zeta} \quad (2.61)$$

Vapor-phase mole fraction:

$$y_i = \frac{z_i}{\frac{\beta(1-\zeta)}{K_i^o} + \frac{(1-\beta)(1-\zeta)}{K_i^w} + \zeta} \quad (2.62)$$

From Eq. (2.60), Eq. (2.61), and Eq. (2.62) were possible to write the following Rachford-Rice equations:

$$f_1(\zeta, \beta) = \sum_{i=1}^n (x_i^o - y_i) = \sum_{i=1}^n \frac{z_i(1 - K_i^o)}{\beta(1-\zeta) + \frac{K_i^o}{K_i^w}(1-\beta)(1-\zeta) + K_i^o\zeta} = 0 \quad (2.63)$$

$$f_2(\zeta, \beta) = \sum_{i=1}^n (x_i^o - x_i^w) = \sum_{i=1}^n \frac{z_i \left(1 - \frac{K_i^o}{K_i^w}\right)}{\beta(1-\zeta) + \frac{K_i^o}{K_i^w}(1-\beta)(1-\zeta) + K_i^o\zeta} = 0 \quad (2.64)$$

$$f_3(\zeta, \beta) = \sum_{i=1}^n (x_i^w - y_i) = \sum_{i=1}^n \frac{z_i \left(\frac{K_i^o}{K_i^w} - K_i^o\right)}{\beta(1-\zeta) + \frac{K_i^o}{K_i^w}(1-\beta)(1-\zeta) + K_i^o\zeta} = 0 \quad (2.65)$$

Therefore, Eq. (2.60), Eq. (2.61), Eq. (2.63), Eq. (2.64), and Eq. (2.65) obtain the separation fraction using the Newton-Raphson method, then calculate the component's equilibrium composition. However, the number of equilibrium phases must be determined before applying the algorithm (NELSON, 1987).

The number of phases could be obtained from bubble and dew point applied in equations Eq. (2.63), Eq. (2.64), and Eq. (2.65) (NELSON, 1987). For a single-phase (V, L_o, or L_w), the equilibrium criteria summarized below inform the necessary and sufficient conditions:

1. Vapor-phase (V):

$$\sum_{i=1}^n \frac{z_i}{K_i^o} - 1 < 0 \text{ and } \frac{z_i}{K_i^w} - 1 < 0 \quad (2.66)$$

2. Liquid oil-phase (L_o):

$$\sum_{i=1}^n z_i K_i^o - 1 < 0 \text{ and } \sum_{i=1}^n z_i \frac{K_i^o}{K_i^w} - 1 < 0 \quad (2.67)$$

3. Liquid aqueous-phase (L_w):

$$\sum_{i=1}^n z_i K_i^w - 1 < 0 \text{ and } \sum_{i=1}^n z_i \frac{K_i^w}{K_i^o} - 1 < 0 \quad (2.68)$$

The test for the existence of a single liquid or vapor phase should be performed before the two-phase test since it does not require iterative calculation. However, dew and bubble point provides only the necessary conditions for two-phase equilibrium. To obtain sufficient conditions, separation factors for the liquid oil- and aqueous phases were defined by Eq. (2.69) and Eq. (2.70), respectively:

$$\psi_1 = \frac{L^o}{F} \quad (2.69)$$

$$\psi_2 = \frac{L^w}{F} \quad (2.70)$$

The literature details each step that links the overall mass balances, molar fractions, new separation factors, and equilibrium constants (ANDRADE, 1991, NELSON, 1987). Then, the equations are reformulated as Rachford-Rice functions in Eq. (2.71) and Eq. (2.72), suitable for numerical solutions (NELSON, 1987):

$$Q_1(\psi_1, \psi_2) = \sum_{i=1}^n \frac{z_i K_i^w (1 - K_i^o)}{K_i^o K_i^w + \psi_1 K_i^w (1 - K_i^o) + \psi_2 K_i^o (1 - K_i^w)} \quad (2.71)$$

$$Q_2(\psi_1, \psi_2) = \sum_{i=1}^n \frac{z_i K_i^o (1 - K_i^w)}{K_i^o K_i^w + \psi_1 K_i^w (1 - K_i^o) + \psi_2 K_i^o (1 - K_i^w)} \quad (2.72)$$

The functions above describe the lateral of a three-phase triangular diagram. The internal part was evaluated using the functions P given by Eq. (2.73), Eq. (2.74), and Eq. (2.75). Functions P are combinations of Eq. (2.71), Eq. (2.72), and separation factor (ψ_1 and ψ_2) (NELSON, 1987).

$$P_1(\psi_1, \psi_2) = -\psi_1 Q_1(\psi_1, \psi_2) - \psi_2 Q_2(\psi_1, \psi_2) \quad (2.73)$$

$$P_2(\psi_1, \psi_2) = (1 - \psi_1) Q_1(\psi_1, \psi_2) - \psi_2 Q_2(\psi_1, \psi_2) \quad (2.74)$$

$$P_3(\psi_1, \psi_2) = -\psi_1 Q_1(\psi_1, \psi_2) + (1 - \psi_2) Q_2(\psi_1, \psi_2) \quad (2.75)$$

Finally, the necessary and sufficient criteria for two-phase are summarized below:

1. Vapor and liquid oil-phases (EL_oV):

$$\sum_{i=1}^n \frac{z_i}{K_i^o} - 1 > 0 \text{ and } \sum_{i=1}^n z_i K_i^o - 1 > 0 \quad (2.76)$$

$$Q_2(\psi_1, 0) < 0 \text{ at the root of } Q_1(\psi_1, 0)$$

2. Vapor and liquid aqueous-phases (EL_wV):

$$\sum_{i=1}^n \frac{z_i}{K_i^w} - 1 > 0 \text{ and } \sum_{i=1}^n z_i K_i^w - 1 > 0 \quad (2.77)$$

$$Q_1(0, \psi_2) < 0 \text{ at the root of } Q_2(0, \psi_2)$$

3. Liquid oil and liquid aqueous-phases (EL_oL_w):

$$\sum_{i=1}^n z_i \frac{K_i^o}{K_i^w} - 1 > 0 \text{ and } \sum_{i=1}^n z_i \frac{K_i^w}{K_i^o} - 1 > 0 \quad (2.78)$$

$$Q_1(\psi_1, 1 - \psi_1) > 0 \text{ at the root of}$$

$$Q_1(\psi_1, 1 - \psi_1) - Q_2(\psi_1, 1 - \psi_1) = 0$$

ANDRADE (1991) suggests the following procedure to perform the three-phase flash algorithm :

- (a) Estimate initial guess values for the equilibrium constants. Methods to estimate these values can be found in the literature depending on the level of information about mixture equilibrium composition. More details are found in GUEDES (2023) and ANDRADE (1991).
- (b) Determine the number of equilibrium phases:
 - 1) test single phase conditions from Eq. (2.66), Eq. (2.67), and Eq. (2.68),
 - 2) test two-phase conditions from Eq. (2.76), Eq. (2.77), and Eq. (2.78),
 - 3) calculate three-phase equilibrium from Eq. (2.63), Eq. (2.64), and Eq. (2.65).
- (c) Obtain the separation factors from Eq. (2.58) and Eq. (2.59),
- (d) Calculate the component's equilibrium fractions from Eq. (2.60), Eq. (2.61), and Eq. (2.62),
- (e) Evaluate a convergence test by comparing the old and new values for the components' equilibrium fractions.

In ANDRADE (1991), the three-phase flash methodology was applied in separation processes to obtain the equilibrium compositions of systems involving water and organic molecules. Additionally, GUEDES (2023) combined the bi-phase flash (EL_oV) with the

vdW-P model to predict the equilibrium temperature of hydrate formation. Subsequently, the authors calculated the temperature difference between the hydrate equilibrium and the corresponding pipeline section in order to propose strategies to avoid hydrate formation.

As previously discussed, thermodynamics software employed in fluid flow analyses typically organizes fluid properties into tables for a range of pressure and temperature. This information is then incorporated into a separate software program that simulates multi-phase flow within pipelines, either dynamically or under steady state conditions.

Similarly, GUEDES (2023) utilized a three-phase flash algorithm to compile x_i^o , x_i^w , y_i , ζ , and β into tables for a range of pressure and temperature. This information was then incorporated into a steady-state multi-phase flow model to evaluate operating conditions in production lines favorable to hydrates formation (GUEDES, 2023).

For a specific pressure and temperature condition in production pipelines, fluid properties were calculated utilizing suitable methodologies (API, 1997, GUEDES, 2015, LOHRENZ *et al.*, 1964, RAIZI, 2005, WHITSON e BRULE, 2000). This was achieved by interpolating fluid compositions and phase fractions that satisfied the multi-phase model solution.

The results regarding flow and fluid characterization, for a light oil and low WC, agreed with well-known commercial software programs used for FA purposes (GUEDES, 2023). However, a disadvantage of this approach is its dependence on commercial software to obtain pure component properties and binary interaction parameters.

In a different approach, GUPTA *et al.* (1991) employed free Gibbs energy to determine equilibrium compositions and phase fractions for multi-phase reacting and non-reacting systems.

Additionally, other work in the literature has combined multi-phase flash calculations with simultaneous stability analysis related to gas hydrates (BALLARD e SLOAN, 2004a, SEGTOVICH *et al.*, 2016). This method provided a comprehensive phase diagram – including hydrate formation within the ice phase – and computed the composition of the hydrate phase (SEGTOVICH *et al.*, 2016).

In the context of steady-state flow simulation, the equilibrium temperature of hydrate formation was the only necessary parameter. Consequently, the methodology described by GUEDES (2023) was well-suited to the objectives of this work.

The phase stability analysis using free Gibbs energy was not required for the preliminary goals of this work. However, it could serve as an alternative approach for generating a complete phase diagram without the need for commercial software support.

Chapter 3

Methodology

The focus of this work was to simulate steady-state multi-phase flow in offshore pipelines prone to natural gas hydrates formation in oil-dominated systems without inhibitors. This chapter presents the methodology employed in this work, which is divided into thermodynamic and kinetic aspects.

The thermodynamic aspect, presented in Section 3.1, describes the methods used to obtain the hydrate stability curve, fluid properties, and three-phase flash data fed in the hydrodynamic model. The kinetic aspect, presented in Section 3.2, details the modifications implemented in the DFM to incorporate the hydrate phase. In addition, each section proposed case studies to evaluate the methodology of this work in both aspects.

3.1 Thermodynamic aspects

3.1.1 Methodology for calculating hydrate stability curve

The hydrate stability curve is derived using a *MATLAB*[®] algorithm, which calculates the equilibrium temperature for hydrate formation by considering the fluid composition and the system pressure throughout the pipeline.

This algorithm determines the temperature that minimizes Eq. (2.2), shown in Section 2.2, which represents the equilibrium of hydrate formation derived from the equality of the chemical potential of water between hydrate and pure water phases. The equality of the chemical potential of water and hydrate phase was obtained from the liquid or vapor component's fugacity and the fugacity of the empty lattice using the vdW-P model.

To minimize the chemical potential – represented by the difference of Eq. (2.3) and Eq. (2.6) – the algorithm applies the *f_{zero}* function in *MATLAB*[®]. This work utilized the modified vdW-P model for mixtures proposed by PARRISH e PRAUSNITZ (1972). The fugacity of the components was calculated using the PR EoS in combination with the van der Waals one-fluid rule for mixtures.

To calculate the Langmuir coefficient, required to solve the vdW-P model, parameters

from MUNCK *et al.* (1988) were applied in Eq. (2.5) (see Table A.1, in Appendix A). The subscript ω in Eq. (2.6) indicates the liquid or ice phase of pure water, which determines the parameters applied for the chemical potential, enthalpy, molar volume, and heat capacity at the reference state (see Table A.2 in Appendix A).

Only values for liquid water were used in this research, valid for temperatures from 250K to 305K and pressures from 0 to 50.7MPa. The reference state in Eq. (2.6) is the triple point of pure water, characterized by a pressure of 612.619Pa and a temperature of 273.19K.

According to MUNCK *et al.* (1988), the water fraction in the vapor and liquid oil phases are negligible. As a result, the algorithm calculating the hydrate stability curve assumes an absence of water in the overall composition for flash calculations. Therefore, the three-phase flash mass balance equations were simplified to the two-phase flash equations as shown in Eq. (3.1) – Eq. (3.3):

Oil-phase mole fraction:

$$x_i^o = \frac{z_i}{1 - \zeta + \zeta K_i^o} \quad (3.1)$$

Vapor-phase mole fraction:

$$y_i = \frac{K_i^o z_i}{1 - \zeta + \zeta K_i^o} \quad (3.2)$$

Sum of overall composition:

$$\sum_{i=1}^c z_i = 1 \quad (3.3)$$

From Eq. (3.1) – Eq. (3.3) were possible to write the Rachford-Rice equation given by Eq. (3.4). To solve this equation and obtain new values for ζ , the Newton-Raphson method was applied.

$$Res(\zeta) = \sum_{i=1}^n \frac{z_i(K_i^o - 1)}{1 - \zeta + \zeta K_i^o} \quad (3.4)$$

The initial guess values in this algorithm used Eq. (3.5) to calculate the initial equilibrium constants.

$$K_i^o = \frac{\exp(5.37(1 + w_i)(1 - T_r^{-1}))}{P_{ri}} \quad (3.5)$$

where, w_i is the acentric factor of component i , $P_{ri} = (P/P_{ci})$ is the reduced pressure, $T_{ri} = (T/T_{ci})$ is the reduced temperature, P_c and T_c are the critical pressure and temperature of component i . All the pure component properties are shown in Table 3.1.

The bi-phase flash, which involves oil in liquid and vapor phases, was applied to determine the separation factor and fluid composition given a known temperature, pressure, and overall composition, as illustrated in Figure 3.1. The dashed arrow – connecting the Rachford-Rice step and the second flowsheet – indicates the interactive internal algorithm to solve Rachford-Rice for ζ .

The separation factor, ζ , indicates the phase with the highest concentration of guest molecules. In the case of a single liquid phase, x_i^o is used to calculate the fugacity of the component in Eq. (2.4). Otherwise, for the single vapor phase or bi-phase, y_i is used in the calculations. A tolerance equal to 10^{-9} was applied to both decision steps illustrated in Figure 3.1, and set a maximum value of 100 iterations for j and k loops.

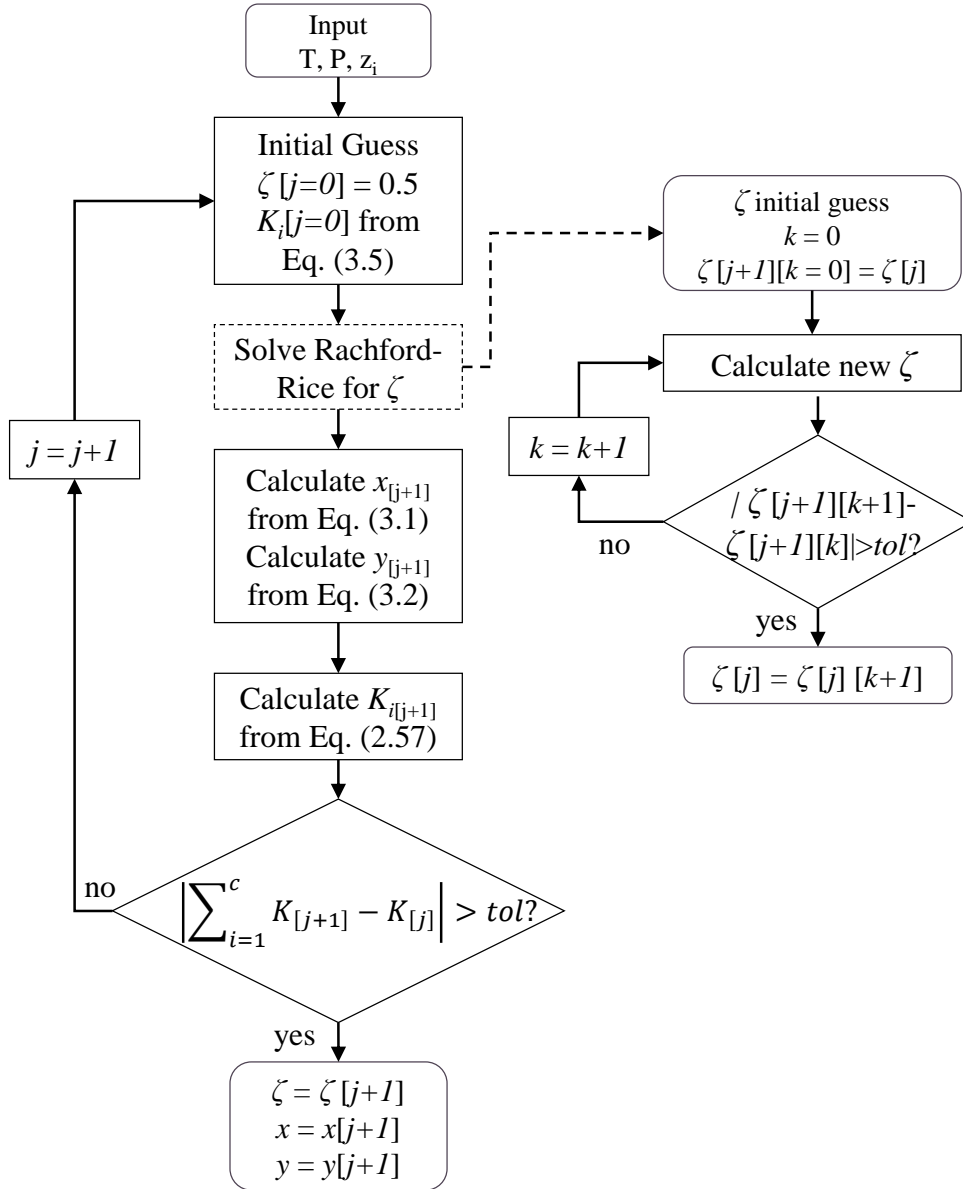


Figure 3.1: Bi-phase flash flowsheet for a known temperature, pressure, and overall composition. The dashed arrow indicates the interactive internal algorithm to solve Rachford-Rice for ζ .

In summary, the algorithm implemented in *MATLAB*[®] for obtaining the hydrate formation curve requires the following inputs:

1. The type of hydrate structure (sI or sII) to be predicted.
2. A guess temperature, T_{guess} , used in the bi-phase flash.

3. A pressure value, which is assumed to be the equilibrium pressure for hydrate formation.

In addition, the algorithm requires access to the following data to perform the calculations:

1. The overall fluid composition, excluding water.
2. Pure components properties data. Table 3.1 contains pure component properties used in this work.
3. A_{ki} and B_{ki} parameters from MUNCK *et al.* (1988) for Eq. (2.5), shown in Table A.1 (see Appendix A).
4. Reference values of a physical constant from MUNCK *et al.* (1988) for Eq. (2.6), shown in Table A.2 (see Appendix A).
5. The reference state used in Eq. (2.6), were $P_0 = 612.619Pa$ and $T_0 = 273.19K$.

Table 3.1: Composition of light oil fluid and pure component properties data obtained from *Multiflash*TM. Reproduced from GUEDES (2023).

Component	Molar fraction (adm)	Critical pressure (Pa)	Critical temperature (K)	Critical volume (m ³ /kg)	Acentric factor (adm)	Molar weight (kg/kgmol)
CO ₂	0.84	7377300	304.12	0.0021	0.223	0.044
N ₂	0.19	3395800	126.19	0.0031	0.0372	0.028
CH ₄	52.89	4599200	190.56	0.0061	0.0104	0.016
C ₂ H ₆	6.81	4871800	305.33	0.0048	0.0991	0.030
C ₃ H ₈	3.68	4247660	369.85	0.0045	0.152	0.044
i-C ₄ H ₁₀	0.82	3640000	407.85	0.0044	0.1844	0.058
n-C ₄ H ₁₀	1.88	3796000	425.16	0.0043	0.1985	0.058
i-C ₅ H ₁₂	0.9	3377000	460.45	0.0042	0.227	0.072
n-C ₅ H ₁₂	1.04	3366500	469.70	0.0043	0.2513	0.072
C ₆ H ₁₄	1.58	3018100	507.82	0.0042	0.2979	0.086
C ₇₊	19.58	1668193	732.07	0.0039	0.6739	0.228
H ₂ O	10	22120000	647.30	0.0031	0.344	0.018

adm: dimensionless

3.1.2 Methodology for calculating fluid properties

In the case studies planned in Sections 3.1.3 and 3.1.4, the initial fluid composition is known. In such circumstances, WHITSON e BRULE (2000) suggests employing compositional simulation. That approach defines the vapor fraction in the mixture and phase

composition through balance calculations based on the properties of pure components (WHITSON e BRULE, 2000).

The properties of the fluid (*i.e.*, density, viscosity, surface tension, enthalpy, heat capacity, and thermal conductivity) can be calculated from suitable methods (RAIZI, 2005). The enthalpies of the liquid and vapor phases were determined via the residual properties using the PR EoS, as recommended by API (1997).

The PR EoS was employed to obtain the densities of the liquid and vapor phases (RAIZI, 2005), while the viscosities of the liquid and vapor phases were determined using the method proposed by LOHRENTZ *et al.* (1964). The PR EoS was extended for mixtures, utilizing a quadratic mixing rule.

The binary interaction component required for the mixing rule was obtained from MEKALA e SANGWAI (2014) or using data from *Multiflash*TM (see Table C.1, in Appendix C). More comprehensive details about the correlations and equations employed for the calculation of fluid properties can be found in GUEDES (2015).

3.1.3 Case studies for hydrate stability curve

The following case studies were proposed to evaluate the applicability and performance of the methodology, described in Section 3.1.1, to obtain the hydrate stability curve:

- a) Case Study 1: This case study aims to reproduce the hydrate formation curve for a system containing a small amount of CO₂, available in GUEDES (2023). The results are then compared with those generated by the software *Multiflash*TM, which is recognized for providing accurate predictions for uninhibited multi-component hydrate systems (BALLARD e SLOAN, 2004b).
- b) Case Study 2: The goal of this case study is to evaluate the limitations of the vdWP model prediction by comparing it with another thermodynamic model used to obtain the hydrate stability curve. This study also aims to evaluate complexities caused by components such as of CO₂, H₂S, and H₂.

The methodology presented in Section 3.1.1 is similar to the one applied by GUEDES (2023) for the management of hydrate formation conditions. GUEDES (2023) evaluated multi-phase flow in pipelines under thermodynamic conditions susceptible to hydrate formation. The prediction was in agreement with those generated by *Multiflash*TM.

The gas hydrate prediction in *Multiflash*TM employs the vdW-P model combined with CPA EoS to describe the fluid phases. Langmuir coefficients are estimated as functions of temperature and adjustable parameters, similar to the method shown in Eq. (2.5). However, in *Multiflash*TM, these parameters are regressed from experimental hydrate dissociation data, and these values are not accessible to the user.

The fluid composition in Case Study 1 contains a mixture of hydrates formers (*i.e.*, methane, ethane, propane, i-butane, n-butane, and carbon dioxide). Table 3.1 provides details on the light oil molar composition used in Case Study 1, as well as the pure component properties employed in both case studies.

However, the fluid utilized in GUEDES (2023) contained a low concentration of CO₂. Consequently, Case Study 2 investigated the accuracy of the methodology when applied to sour natural gas with different concentrations of CO₂, H₂S, and H₂, as detailed in Table 3.2. Additionally, the results are compared with those obtained using the C-G model approach, available in MEKALA e SANGWAI (2014).

Table 3.2: Molar composition of sour natural gas used in Case Study 2, containing varying amounts of CO₂, H₂S, and H₂. Adapted from MEKALA e SANGWAI (2014).

GAS	N ₂	CO ₂	H ₂ S	C ₁	C ₂	C ₃	<i>i</i> -C ₄	<i>n</i> -C ₄	<i>i</i> -C ₅	<i>n</i> -C ₅	C ₆₊
1	–	31.4	–	52.5	8.12	4.74	1.31	1.88	–	–	–
2	0.84	1.74	–	84.19	8.76	3.35	0.32	0.6	0.08	0.08	0.02
3	0.43	0.51	–	593.2	4.25	1.61	–	–	–	–	–
4	9.59	3.19	–	86.32	0.78	0.03	0.01	0.018	0.01	0.01	0.07
5	–	12.6	5.4	82	–	–	–	–	–	–	–
6	–	12	8	80	–	–	–	–	–	–	–

– not applicable

MEKALA e SANGWAI (2014) evaluated the performance of the C-G model in predicting hydrate formation conditions by comparing its results with experimental data derived from sour natural gas. The authors employed the PR EoS to calculate the fugacity of each component and utilized the Kihara potential to determine the Langmuir coefficients.

In summary, the objective of Case Study 1 was to replicate the results presented in GUEDES (2023) and *Multiflash*TM for a light oil system, and to subsequently discuss any similarities or discrepancies. On the other hand, the objective of Case Study 2 was to investigate the limitations of the proposed methodology by contrasting it with an alternative approach that suggested improve the accuracy in the presence of complexities caused by components such as CO₂, H₂S, and H₂.

In both case studies, the sII structure was used as input and the guess temperature was equal to 300K. The verification of *MATLAB*[®] result was measured using the relative error (*REP*) given by Eq. (3.6). The superscript *ref* refers to reference hydrate equilibrium temperature data obtained from *Multiflash*TM, GUEDES (2023), or MEKALA e SANGWAI (2014). The superscript *MTLB* refers to *MATLAB*[®] result obtained in this work.

$$REP = \frac{|T_{hyd,eq}^{ref} - T_{hyd,eq}^{MTLB}|}{T_{hyd,eq}^{ref}} \quad (3.6)$$

3.1.4 Case study for fluid properties

As mentioned in Chapter 2, there is a lack of fluid characterization in research dedicated to hydrate formation simulations. This work proposed the following case study to evaluate the applicability and performance of the three-phase flash calculations implemented in *MATLAB*[®]. This analysis will focus on obtaining phase composition, separation factors, and fluid properties.

- a) Case Study 3: This study aims to obtain fluid properties profile along the pipeline using real fluid data from the literature, applicable to oil-dominated systems (RAO, 2013, SJÖBLOM *et al.*, 2010, ZERPA, 2013).

The SARA analysis, shown in Table 3.3, characterized the crude oil from the Caratinga field. This method quantifies the fluid's hydrocarbon fractions according to the following groups: saturates, aromatics, asphaltenes, and resins. The details of the SARA analysis and information of the components present in the Caratinga fluid are available in SJÖBLOM *et al.* (2010) and RAO (2013), respectively.

Table 3.3 indicates that the original fluid contains resins, a component not supported in the methodology of this work for obtaining fluid properties. Furthermore, the hydrodynamic model assumes a Newtonian fluid; a hypothesis valid for fluid with a maximum molecular weight of 5000kg/kgmol (TEIXEIRA, 2016).

Table 3.3: Saturates, aromatics, asphaltenes, and resins fractions from the SARA analysis and density of Caratinga crude oil. Adapted from SJÖBLOM *et al.* (2010).

Property	Value
Density (kg/m^3)	914.0
Asphaltene content (%)	6.2
Saturates content (%)	39.8
Aromatic content (%)	39.8
Resin content (%)	14.3

The crude fluid documented in the literature consists of 36 hydrocarbon components (RAO, 2013). The thermodynamic model employed in this work uses the pure component properties and mixing rules to characterize the fluid. However, managing such a large number of parameters for each component is impractical, especially as some of them are not readily available. In such cases, commercial software represents minor heavy fractions using a pseudo-component.

Originally, the pseudo-component was generated by separating the distillation curve according to the boiling point, with each subinterval representing a mixture of hydrocarbons included in that set. An alternative approach is to generate the pseudo-component

based on SARA analysis and density information. In this study, SARA analysis, density, and original fluid composition data were employed in *Multiflash*TM to generate the pseudo-component, C₁₁₊, which comprise the remaining twenty-five heavy fractions of the original fluid.

This work adapted the pseudo-fluid composition by removing the resin fraction, as detailed in Table 3.4. This reformulation is suitable for three-phase flash calculations and the fluid characterization methods employed. The algorithm utilized for the three-phase flash is described in Section 2.5.1, and the pure components data are shown in Table 3.4.

Table 3.4: Pure component properties and composition of the pseudo-fluid based on crude oil from Caratinga field without resins. Data obtained from *Multiflash*TM.

Component	WC 0%	WC 30%	Molecular weight (kg/kg mol)	Critical temperature (k)	Critical pressure (Pa)	Acentric factor (adm)	Critical volume (m ³ /kgmol)
CH ₄	29.648	20.7536	16.0428	190.5640	4599200	0.0104	162.6600
C ₃	0.403	0.2821	44.0956	369.8500	4247660	0.1520	220.4780
i-C ₄	0.541	0.3787	58.1222	407.8500	3640000	0.1844	224.3520
n-C ₄	1.646	1.1522	58.1222	425.1600	3796000	0.1985	227.8391
i-C ₅	1.345	0.9415	72.1488	460.4500	3377000	0.2270	235.7803
n-C ₅	1.799	1.2593	72.1488	469.7000	3366500	0.2513	232.0001
C ₆	3.345	2.3415	80.7112	512.8682	3145284	0.2822	246.3140
C ₇	7.941	5.5587	93.5069	541.8461	3125247	0.3112	251.1573
C ₈	6.117	4.2819	105.3183	567.2513	2958243	0.3455	252.3766
C ₉	5.871	4.1097	119.0982	593.9460	2740094	0.3885	252.4134
C ₁₀	5.007	3.5049	133.8625	619.6445	2524469	0.4354	251.9252
C ₁₁₊	36.337	25.4359	227.1037	737.0574	1664200	0.6992	248.7055
H ₂ O	0	30	18.0152	647.3000	22120000	0.3440	322.0001

adm: dimensionless

The method for estimating the equilibrium constants follows recommendations from ANDRADE (1991). An initial vapor-phase mole fraction was obtained by assuming a bi-phase flash without water, following the same steps illustrated in Figure 3.1. To obtain the initial oil-phase mole fractions and water-phase mole fractions, each phase was assumed to be rich in methane and water, respectively.

Subsequently, the methodology suggested by ANDRADE (1991) was employed to compute the component mole fractions in the raffinate and extract phases. Finally, the phases' mole fractions were used in Eq. (2.57) to obtain the guess equilibrium constants required in the three-phase flash algorithm.

This procedure to obtain the initial guess was applied at the lower pressure in each temperature to ensure the method's applicability. For subsequent pressures, the previous x_i^o , x_i^w , and y_i were used as the initial guess to initiate the three-phase flash algorithm.

The three-phase flash results were compiled into a table containing x_i^o , x_i^w , y_i , ζ , and β for a range of pressure and temperature between $1 \times 10^5 Pa$ to $1.2 \times 10^7 Pa$ and $270K$ to $340K$ respectively. In this table, each row is associated with a fixed temperature, and every n -th column corresponds to a specific pressure, where n is the number of components in the fluid.

The constructed table was then fed into the steady-state DFM to evaluate the operational conditions in production lines favorable for hydrate formation. Similarly, *Multi-flash*TM generated the fluid properties table which was input into *OLGA*[®].

In summary, Case Study 3 aimed to compare the fluid properties and phase fractions obtained from the methodology proposed in this work with those derived from commercial software dedicated to multi-phase flow and multi-component fluid characterization. Consequently, this study investigated whether the flash calculations and correlations used to determine fluid properties were adequate to characterize fluids similar to those encountered in real operations.

3.2 Kinetic aspects

3.2.1 Modifications to include hydrates in the DFM

The present work proposed to include the effects of hydrates formation in the DFM under steady-state conditions. The objective was to analyze whether this approach could reproduce the behavior observed in the literature regarding hydrate formation in oil-dominated systems.

The following hypotheses were applied to simplify the addition of the hydrate phase into the DFM:

- (i) Steady-state and unidimensional flow;
- (ii) Newtonian fluid;
- (iii) Liquid and gas are compressible and described by PR EoS;
- (iv) A first-order rate kinetic model, shown in Eq. (2.10), was applied. It does not prevent the application of other models in future works. As mentioned in Section 2.3, this model is usually a starting point for introducing hydrate formation prediction into multi-phase flow models;
- (v) Only gas methane is consumed to form hydrates. Consequently, all hydrates parameter refers to sI structure and methane gas properties;
- (vi) The deposition phenomenon is neglected. It is assumed that hydrate particles are suspended in the liquid phase (*i.e.*, water and oil) forming a homogeneous dispersion.

(vii) No-slip condition exists between the hydrate-liquid and hydrate-gas phases. The hydrates velocity is equal to the liquid phase velocity (see Eq. B.17, in Appendix B);

(viii) Hydrate formation does not occur in the single-phase liquid flow.

Section 2.3 provides an introduction to the kinetic models used to predict hydrate formation and dissociation rates. The gas consumption rate described in Eq. (2.10) was denoted as R_{gas} in the modified DFM, as shown in Eq. (3.7):

$$\frac{dm_{gas}}{dt} = -uk_1 \exp\left(\frac{k_2}{T_{sys}}\right) A_s (T_{eq}^{hyd} - T_{sys}) = -R_{gas} \quad (3.7)$$

Eq. (3.8) corresponds to the rate of hydrate formation. The subscript g refers to the consumption of gas hydrate (*i.e.*, methane). The terms preceding the gas consumption rate, $\frac{dm_{gas}}{dt}$, refer to the mass of hydrates formed. For methane hydrates, we apply the following pseudo-stoichiometric equation: $\text{CH}_4 + n_H \text{H}_2\text{O} \longrightarrow 1 + n_H \text{Hyd}$.

$$\frac{dm_{hyd}}{dt} = -(1 + n_H) \frac{M_w}{M_g} \frac{dm_{gas}}{dt} = R_{hyd} \quad (3.8)$$

where R_{hyd} represents the hydrate formation rate. The conservation equations of the DFM were modified to incorporate the terms for hydrate mass and energy generation. Eq. (3.9) integrates the gas consumption rate into the vapor phase mass balance:

$$\frac{d(\alpha_v \rho_v U_m)}{dx} = \Gamma_v - \frac{d}{dx} \left(\frac{\alpha_v \rho_v \rho_l}{\rho_m} \hat{v}_v^{dft} \right) - R_{gas} \quad (3.9)$$

Eq. (3.10) presents the hydrate continuity equation, which incorporates Eq. (3.8) and assumes that the hydrate velocity equals the liquid velocity. To integrate Eq. (3.10) into the DFM, Eq. (B.17) was rewritten in terms of the mixture velocity. The liquid velocity in Eq. (3.10) was replaced with the mixture velocity. The resulting equation is shown in Eq. (3.11):

$$\frac{d(\alpha_{hyd} \rho_{hyd} U_l)}{dx} = R_{hyd} \quad (3.10)$$

$$\begin{aligned} -\alpha_{hyd} \rho_{hyd} \frac{dU_m}{dx} - \alpha_{hyd} U_m \frac{d\rho_{hyd}}{dx} - \rho_{hyd} U_m \frac{d\alpha_{hyd}}{dx} - R_{hyd} \\ + \frac{1}{(1 - \alpha_v)} \frac{dG_2}{dx} + \frac{G_2}{(1 - \alpha_v)^2} \frac{d\alpha_v}{dx} = 0 \end{aligned} \quad (3.11)$$

Where G_2 is described by Eq. (3.12):

$$G_2 = \frac{\alpha_{hyd} \rho_{hyd} \alpha_v \rho_v}{\rho_m} \hat{v}_v^{dft} \quad (3.12)$$

The energy source term associated with hydrate formation, denoted as Q_{hyd} , is given by Eq. (3.13). This heat, added to the system, is incorporated into the mixture energy

balance, as shown in Eq. (3.14):

$$Q_{hyd} = -\Delta h_{hyd} R_{gas} \quad (3.13)$$

$$\begin{aligned} \frac{d(\rho_m U_m h_m)}{dx} = & Q_{fn} - \frac{d}{dx} \left[\frac{\alpha_v \rho_v \rho_l}{\rho_m} (h_v - h_l) \hat{v}_v^{dft} \right] \\ & + \frac{dP}{dx} \left[U_m + \frac{\alpha_v (\rho_l - \rho_v)}{\rho_m} \hat{v}_v^{dft} \right] + Q_{hyd} \end{aligned} \quad (3.14)$$

The mixture properties have been revised to incorporate the hydrate void fraction, as represented in Eq. (3.15) – Eq. (3.17). In the absence of hydrates, the mixture properties return in terms of liquid and gas phase fractions.

$$\rho_m = \alpha_v (\rho_v - \rho_l) + \alpha_{hyd} (\rho_{hyd} - \rho_l) + \rho_l \quad (3.15)$$

$$U_m = \frac{1}{\rho_m} [\alpha_v (\rho_v U_g - \rho_l U_l) + \alpha_{hyd} U_l (\rho_{hyd} - \rho_l) + \rho_l U_l] \quad (3.16)$$

$$h_m = \frac{1}{\rho_m} [\alpha_v (\rho_v h_g - \rho_l h_l) + \alpha_{hyd} (\rho_{hyd} h_{hyd} - \rho_l h_l) + \rho_l h_l] \quad (3.17)$$

The agglomeration model, given by Eq. (2.25) and discussed in Section 2.3.3, was employed to evaluate the pressure loss due to hydrate particles. The hydrate slurry influences friction loss and results in an increased pressure drop.

There is no explicit equation denoting water consumption. The impact of hydrate formation is evidenced in the reduction of the liquid phase fraction. This represents a limitation that could be explored in future studies. In this work simulation, the quantity of water was not completely consumed. The reaction was constrained by the availability of the gas phase from the vaporization process.

3.2.2 DAE system used in DASSLC

The modified DFM outlined in Section 3.2.1 was written into a DAE system and solved using the DASSLC numerical integrator (SECCHI, 2012) in *MATLAB*[®]. In the absence of hydrates, the DAE system used is identical to the one described by GUEDES (2023). However, in the presence of hydrates, the model is configured to account for the variables and their derivatives as follows:

- $y(1) = P; yp(1) = \frac{dP}{dx}$
- $y(2) = \alpha_v; yp(2) = \frac{d\alpha_v}{dx}$
- $y(3) = U_m; yp(3) = \frac{dU_m}{dx}$

- $y(4) = \rho_m; yp(4) = \frac{d\rho_m}{dx}$
- $y(5) = \rho_v; yp(5) = \frac{d\rho_v}{dx}$
- $y(6) = G_1; yp(6) = \frac{dG_1}{dx}$
- $y(7) = \hat{v}_v^{dft}; yp(7) = \frac{d\hat{v}_v^{dft}}{dx}$
- $y(8) = T; yp(8) = \frac{dT}{dx}$
- $y(9) = h_m; yp(9) = \frac{dh_m}{dx}$
- $y(10) = h_v; yp(10) = \frac{dh_v}{dx}$
- $y(11) = h_l; yp(11) = \frac{dh_l}{dx}$
- $y(12) = \beta_w; yp(12) = \frac{d\beta_w}{dx}$
- $y(13) = m_{gas}; yp(13) = \frac{dm_{gas}}{dx}$
- $y(14) = \alpha_{hyd}; yp(14) = \frac{d\alpha_{hyd}}{dx}$
- $y(15) = \rho_{hyd}; yp(15) = \frac{d\rho_{hyd}}{dx}$
- $y(16) = G_2; yp(16) = \frac{dG_2}{dx}$

Where G_1 is given in terms of spatial derivative, as shown in Eq. (3.18):

$$G_1 = \frac{\alpha_v \rho_v \rho_l}{\rho_m} \hat{v}_v^{dft} \quad (3.18)$$

- $res(1) = -y(3)yp(4) - y(4)yp(3)$
- $res(2) = \Gamma_v - R_{gas} - y(2)y(5)yp(3) - y(2)y(3)yp(5) - y(5)y(3)yp(2) - yp(6)$

- $res(3) = -y(4)g \sin(\theta) - F_{mv} - \frac{y(7)}{1-y(2)}yp(6) - \frac{y(6)}{1-y(2)}yp(7) - \frac{y(6)y(7)}{[1-y(2)]^2}yp(2) - y(3)^2yp(4) - 2y(4)y(3)yp(3) - yp(1)$
- $res(4) = y(4) - \rho_m^{calc}$
- $res(5) = y(5) - \rho_v^{calc}$
- $res(6) = y(6) - G_1^{calc}$
- $res(7) = y(7) - \hat{v}_v^{dft}$
- $res(8) = Q_{mv} + Q_{hyd} + [y(10) - y(11)]yp(6) - y(6)yp(10) + y(6)yp(11) + yp(1) \left[y(3) \frac{y(2)[\rho_l^{calc} - y(5)]y(7)}{y(4)} \right] - y(9)y(3)yp(4) - y(9)y(4)yp(3) - y(4)y(3)yp(9)$
- $res(9) = y(9) - h_m^{calc}$
- $res(10) = y(10) - h_v^{calc}$
- $res(11) = y(11) - h_l^{calc}$
- $res(12) = y(12) - \beta_w^{calc}$
- $res(13) = U_l yp(13) + R_{gas}$
- $res(14) = -y(14)y(15)yp(4) - y(14)y(4)yp(15) - y(15)y(4)yp(14) - R_{hyd} + \frac{1}{1-y(2)}yp(16) + \frac{y(16)}{[1-y(2)]^2}yp(14)$
- $res(15) = y(15) - \rho_{calc}$
- $res(16) = y(16) - G_2^{calc}$

3.2.3 Modification in gas consumption equation

The term $\frac{dm_{gas}}{dx}$, used in the gas consumption residue, was obtained by modifying the gas consumption rate, R_{gas} , in terms of the liquid phase velocity. This adjustment allows the model to monitor the movement of particles along the pipeline, as shown in Eq. (3.19):

$$\frac{dm_{gas}}{dx} = \frac{1}{U_l} \frac{dm_{gas}}{dt} = -\frac{1}{U_l} R_{gas} = -\frac{1}{U_l} \left[\frac{M_g}{M_w(1+n_H)} \right] R_{hyd} \quad (3.19)$$

Table 3.5 presents the values of the intrinsic kinetic formation and dissociation constants employed in Eq. (3.19).

Table 3.5: Intrinsic formation and dissociation kinetic constants for the first-order rate kinetic model used in Eq. (3.19). Adapted from (RAO, 2013).

	k_1 (kg/m ² /K/s)	k_2 (K)
Formation	exp(41.1393)	-13616.2288
Dissociation	exp(57.9886)	-16695.4770

The nucleation subcooling temperature was assumed to be 3.5K, which means the reaction is activated when subcooling achieves a value above this threshold (TURNER *et al.*, 2005, ZERPA *et al.*, 2012). When the hydrate nucleation subcooling condition is met ($\Delta T_{sub} > 3.5K$), the hydrate formation reaction is activated. However, if the nucleation subcooling condition was previously met and the subcooling subsequently becomes negative, the hydrate dissociation reaction is initiated.

3.2.4 Hydrates properties

As discussed in Chapter 2, hydrate formation is non-stoichiometric, leading to variable properties. The molecular weight of gas hydrates was calculated based on the degree of saturation within the crystal structure (CARROL, 2009), as shown in Eq. (3.20):

$$M_{hyd} = \frac{(N_w M_w + \sum_{j=1}^c \sum_{i=1}^N Y_{ij} v_i M_j)}{N_w + \sum_{i=1}^N Y_{ij} v_i} \quad (3.20)$$

The density can be calculated from the relation between the degree of saturation and the crystal volume (CARROL, 2009) given by Eq. (3.22):

$$\rho_{hyd} = \frac{(N_w M_w + \sum_{j=1}^c \sum_{i=1}^N Y_{ij} v_i M_j)}{N_{ava} V_{cell}} \quad (3.21)$$

where M_w is the water average molar mass, ρ_{hyd} is the hydrate density, Y_{ij} is the fractional occupation of cavity i by component j (see Section 2.2), N_w is the number of water molecules per unit cell (see Table 2.1), v_i is the number of type i cavities per water molecule in the unit cell (see Table 2.1), V_{cell} is the volume of the unit cell (see Table 2.1), N_{ava} is the Avogadro's number (6.023×10^{23} molecules/mol). The subscripts N and c represent, respectively, the number of cavity types in the unit cell (2 for both sI and sII) and the number of components in the hydrate phase.

The enthalpy of the hydrate is expressed as a function of the heat of the reaction and the component's enthalpy at the system's temperature and pressure (ZERPA, 2013), as shown in Eq. (3.22) :

$$h_{hyd} = \frac{h_g + n_H h_w + \Delta h_{hyd}}{1 + n_H} \quad (3.22)$$

where h is the specific enthalpy, n_H is the hydration number (assumed 5.85 for sI struc-

ture), and Δh_{hyd} is the heat of reaction of hydrate formation (equal to $-4175.4 \times 10^3 \text{ J/kg}$ of gas). The subscripts g , w , and hyd correspond to gas, water, and hydrate. In the proposed methodology, the hydrate particles are composed of water and methane molecules, so the enthalpies of these components were used.

3.2.5 Agglomeration model

To simplify the solution of Eq. (2.25), the original equation was rewritten into two algebraic equations, as demonstrated in Eq. (3.23) and Eq. (3.24):

$$d_A = - \frac{F_a \left[1 - (\alpha_{hyd}^{eff} / \alpha_{hyd}^{max}) \right]^2}{d_P \mu_0 \delta \left(1 - \alpha_{hyd}^{eff} \right) \left(\alpha_{hyd}^{eff} / \alpha_{hyd} \right)} \quad (3.23)$$

$$\alpha_{hyd}^{eff} = \alpha_{hyd} (d_A / d_P)^{(1/2)} \quad (3.24)$$

Figure 3.2 provides a summary of the algorithm used to obtain the particle agglomerate diameter and effective hydrate volume fraction using the equations above.

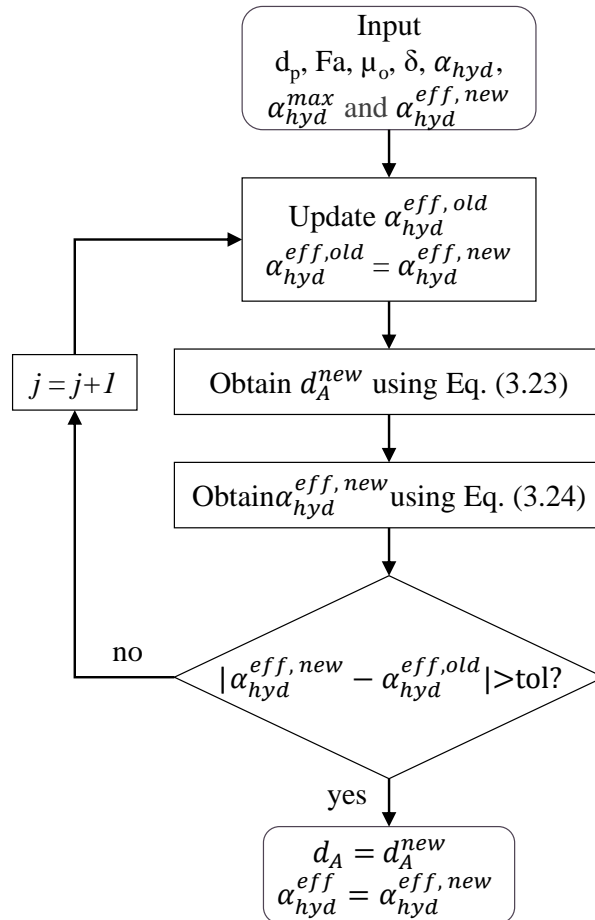


Figure 3.2: Flowsheet to obtain agglomeration diameter and effective hydrate volume fraction from agglomeration model proposed by CAMARGO e PALERMO (2002).

The value of α_{hyd}^{max} is equal to 4/7 and f is equal to 2.5 (ZERPA *et al.*, 2012). The initial guess for α_{hyd}^{eff} assumes a value 30% bigger than α_{hyd} obtained from the mass balance in the DFM. The hydrate particle diameter is obtained from Eq. (2.24). The shear rate is calculated using the shear stress and viscosity relation, assuming Newtonian fluid in the oil phase. Finally, the cohesion force is calculated using Eq. (2.26).

3.2.6 Flow regimes

As mentioned in Chapter 2, most of the works in the literature to predict hydrate formation in pipelines were limited to a specific flow pattern and pipe inclination. For the DFM, BHAGWAT e GHAJAR (2014) suggested a method independent of flow map regimes to obtain the drift-flux parameters $\langle v_v^{dft} \rangle_\alpha$ and C_0 (GUEDES, 2023, GÓES *et al.*, 2023).

The drift-flux distribution parameter, C_0 , is given by Eq. (3.25):

$$C_0 = \frac{2 - (\rho_v/\rho_l^2)}{1 + (Re_{tp}/1000)^2} + \frac{\left[\left(\sqrt{\frac{1 + (\rho_v/\rho_l)^2}{1 + \cos \theta}} \right)^{(1-\alpha_v)} + C_{0.1} \right]^{2/5}}{1 + (1000/Re_{tp})^2} \quad (3.25)$$

where Re_{sg} is the two-phase Reynolds number, given by Eq. (3.26), and θ is the pipe orientation term.

$$Re_{tp} = \frac{U_m \rho_l D}{\mu_l} \quad (3.26)$$

$C_{0.1}$ is defined by Eq. (3.27) in terms of gas-to-liquid phase density ratio, the gas volumetric flow fraction (ϑ , given by Eq. (3.28)), the two-phase flow quality (χ , provided by Eq. (3.29)), the Froude number (Fr_{sg} , provided by Eq. (3.30)), C_l which is determined by the pipe geometry, given by Eq. (3.31), and the two-phase flow friction factor (f_{sg} , given by Eq. (3.32)),

$$C_{0.1} = \begin{cases} 0, & 0^\circ \geq \theta \geq -50^\circ \\ & \text{and } Fr_{sg} \leq 0.1 \\ (C_l - C_1 \sqrt{\rho_v \rho_l})[(2.6 - \vartheta)^{0.15} - \sqrt{f_{tp}}](1 - \chi)^{1.5}, & \text{otherwise} \end{cases} \quad (3.27)$$

$$\vartheta = \frac{U_{sv}}{U_{sv} + U_{lv}} \quad (3.28)$$

$$\chi = \frac{\rho_v U_{sv}}{\rho_v U_{sv} + \rho_l U_{lv}} \quad (3.29)$$

$$Fr_{sv} = \sqrt{\frac{\rho_v}{\rho_l - \rho_v} \frac{U_{sv}}{g D \cos \theta}} \quad (3.30)$$

$$C_1 = \begin{cases} 0.2, & \text{for circular pipes} \\ 0.4, & \text{for square ducts} \end{cases} \quad (3.31)$$

For turbulent flows, the Fanning friction factor can be calculated from Eq. (3.32) and Eq. (3.33) (CHEN, 1979):

$$f_{tp} = \frac{1}{f_n^2} \quad (3.32)$$

$$f_n = -2 \log_{10} \left\{ \frac{e}{3.7065D} - \frac{5.0452}{Re_{tp}} \log_{10} \left[\frac{(e/D_p)^{1.1098}}{2.8257} + \left(\frac{7.149}{Re_{tp}} \right)^{0.8981} \right] \right\} \quad (3.33)$$

The drift velocity parameter, $\langle \hat{v}_v^{dft} \rangle_\alpha$, was obtained using a function dependent on pipe diameter, inclination angle, fluid properties, vapor flow rates, and vapor void fraction, as shown in Eq. (3.34):

$$\langle \hat{v}_v^{dft} \rangle_\alpha = (0.35 \sin \theta + 0.45 \cos \theta) \sqrt{\frac{gD(\rho_l - \rho_v)}{\rho_l}} (1 - \alpha_v)^{0.5} C_2 C_3 C_4 \quad (3.34)$$

where C_2 , C_3 , and C_4 are defined by Eq. (3.35) – Eq. (3.37). The variables account, respectively, for the effects of liquid phase dynamic viscosity on the drift velocity, a correction factor in the drift velocity related to pipe diameter, and a correction to assure positive value for drift velocity.

$$C_2 = \begin{cases} \frac{0.434}{\log_{10}(\mu_l/0.001)}, & (\mu_l/0.001) > 10 \\ 1, & (\mu_l/0.001) \leq 10 \end{cases} \quad (3.35)$$

$$C_3 = \begin{cases} (La/0.025)^{0.9}, & La > 0.025 \\ 1, & La \leq 0.025 \end{cases} \quad (3.36)$$

$$C_4 = \begin{cases} -1, & 0^\circ \geq \theta \geq -50^\circ \text{ and } Fr_{sg} \leq 0.1 \\ 1, & \text{otherwise} \end{cases} \quad (3.37)$$

The term La is the Laplace variable, given by Eq. (3.38):

$$La = \sqrt{\frac{\sigma}{g(\rho_l - \rho_v)}} \frac{1}{D} \quad (3.38)$$

3.2.7 Case studies for kinetics of hydrate formation

This work proposed a modification into the steady-state DFM to predict hydrates formation in pipelines. The following case studies are designed to investigate the applicability and performance of the modified DFM implemented in *MATLAB*®:

- a) Case Study 4: This study aims to evaluate the steady-state simulation without hydrates. The objective is to compare the agreement between operational conditions obtained from the DFM in *MATLAB*[®], TFM in *OLGA*[®], and the data in the literature for an oil-dominated system favorable to hydrate formation (ZERPA, 2013).
- b) Case Study 5: This case study aims to analyze the risk of pipeline plugging using the agglomeration model. The impact of hydrate formation is assessed by changes in the effective hydrate volume fraction and relative viscosity.

Case Studies 4 and 5 were based on the Caratinga well geometry, material, and inputs available in ZERPA (2013). Table 3.6 presents the geometry of a Brazilian well in the Caratinga field located in Campos Basin. Table 3.7 shows pipeline material properties required to perform the simulation in *OLGA*[®] and in *MATLAB*[®].

Table 3.6: Caratinga well geometry (ZERPA, 2013).

Pipe section	x (m)	y (m)	Angle (°)	Roughness* (m)	Diameter (m)
Start	2000	-1166.51	0		
Flowline 01	10866.60	-1155.74	0.07		
Flowline 02	13876.43	-1136.71	0.36	2x10 ⁻⁵	0.1524
Flowline 03	15482.07	-1080.11	2.02		
Riser 01	16064.54	-915.643	15.76		
Riser 02	16890.73	0	47.94		

* value reported in GÓES *et al.* (2023).

Table 3.7: Pipeline material properties.

	Density* (kg/m ³)	Specific heat* (J/kg/K)	Thermal conductivity* (W/m/K)
Flowline and riser	7850	500	50

* value reported in GÓES *et al.* (2023).

The simulation considered a non-insulated flowline and riser. The pipeline roughness follows the data available in the literature for similar study conditions (GÓES *et al.*, 2023). Table 3.8 summarizes the inputs used in the steady-state multi-phase flow models. The overall heat transfer coefficient, shown in Table 3.8, fitted the temperature profile, as suggested by ZERPA (2013) and RAO (2013).

Table 3.8: Caratinga case study description.

WC (%)	T _{in} (K)	P _{in} (bar)	P _{out} (bar)	W _v (kg/s)	W _o (kg/s)	W _w (kg/s)	U _{heat} (W/m ² /K)
30	56.53	87.72	19.14	0.014323	0.07083	0.48588	20

The objective of Case Study 4 was to investigate if the predictions made by the DFM and the TFM were similar concerning the temperature, pressure, and velocity profiles. It also aimed to identify pipeline sections that are favorable for hydrate formation according to the methodology shown in Section 3.2. Case Study 5 aimed to measure hydrate formation and dissociation in risk areas and evaluate whether these behaviors align with observations reported in the literature.

Chapter 4

Result and discussion

4.1 Case Study 1

Case Study 1 analyzed the methodology detailed in Section 3.1.1 for obtaining the hydrate equilibrium temperature. The objective was to replicate the results observed in GUEDES (2023) and discuss any similarities or discrepancies with results from the commercial software *Multiflash*TM.

Figure 4.1 illustrate the comparison of hydrate equilibrium curves derived from GUEDES (2023), *Multiflash*TM, and the algorithm developed for this study, implemented in *MATLAB*[®]. The fluid that was evaluated contained a mixture of natural gas hydrates with a small concentration of CO₂. For this study, the equilibrium for hydrate formation assumed sII structure.

In Figure 4.1, the solid and dash-dotted black lines symbolize, respectively, the hydrate formation curve and the bubble point curve predicted by software *Multiflash*TM. The black asterisk and circle present the results obtained, respectively, from GUEDES (2023) and this work, both implemented in *MATLAB*[®].

The average relative error presented less than a 0.3% divergence between this work and GUEDES (2023) results, given the identical methodology utilized to derive a hydrate stability curve. Furthermore, the algorithm implemented in *MATLAB*[®] indicated less than a 1% discrepancy with the *Multiflash*TM predictions, paralleling the results reported in GUEDES (2023).

The minor discrepancy between the results of this study and those obtained from GUEDES (2023) was considered negligible. The error was attributed to potential imprecision in extracting data from the original source figures. The aligned results validate the successful replication of the previous methodology, implemented in *MATLAB*[®], for predicting the thermodynamic conditions favorable for hydrate formation.

Regarding the comparison with *Multiflash*TM, the observed discrepancies could be associated with two methodological differences: (1) the commercial software employs

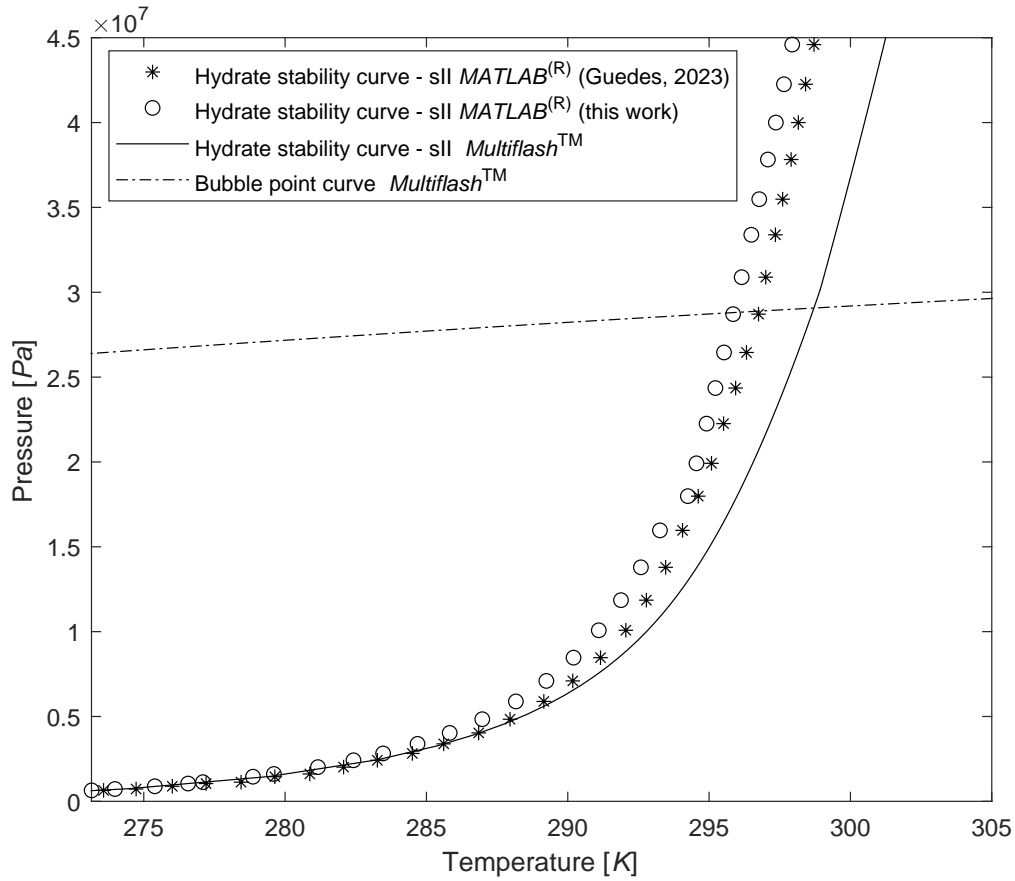


Figure 4.1: Study Case 1 Result: A comparison of hydrate formation curves obtained from previous studies and the present work, using an algorithm implemented in *MATLAB*[®]. The fluid considered contained a low concentration of CO_2 and was suitable for sII structure. The solid black line represents the prediction from *Multiflash*TM, the black asterisks denote the results of GUEDES (2023), and the black circles show the results obtained from this work. The dash-dotted line represents the bubble point curve predicted by *Multiflash*TM, corresponding to the transition between the liquid and biphasic regions.

the CPA EoS, while this work methodology utilizes the PR EoS and (2) Langmuir parameters in the commercial software are regressed from experimental data and are not user-accessible.

The fluid under consideration does not exhibit a significant effect of hydrogen bonding or association of components. This implies that the observed discrepancy between *Multiflash*TM and *MATLAB*[®] results arises due to the updated parameters used to obtain the Langmuir coefficient, which likely enhanced prediction accuracy in the commercial software.

4.2 Case Study 2

Case Study 1 successfully demonstrated the reproduction of the methodology used to determine the thermodynamic conditions favorable for hydrate formation in production

lines. Case Study 2 aimed to explore the limitations of the current approach in addressing complexities introduced by certain guest molecules. In addition, this case study compared the discrepancies between this approach and another thermodynamic model available in the literature.

As detailed in Section 3.1.3, MEKALA e SANGWAI (2014) evaluated the performance of the C-G model against experimental data. The researcher employed the PR EoS and Kihara's potential to predict the hydrate stability curve for sII structure in different sour natural gas compositions.

Table 4.1 summarizes the relative error between the experimental data (second row) and the predictions of the C-G model (third row) for the gases listed in Table 3.2. Figures 4.2 to 4.7 illustrate the comparison among experimental data, predictions from the C-G model, and those from the vdW-P model for each sour natural gas composition.

Table 4.1: Summary of relative error for the hydrate equilibrium curve in Case Study 2, comparing the result from this work, C-G model, and the experimental data reported in MEKALA e SANGWAI (2014).

GAS	1	2	3	4	5	6
REP 1 (%)	0.0845	0.2373	0.2007	1.0911	1.1623	1.3139
REP 2 (%)	0.2614	0.3535	0.2933	1.0376	1.1650	1.3133

REP 1: relative error between experimental data and vdW-P model results.

REP 2: relative error between predictions of the vdW-P model and the C-G model.

In all the figures, the circles represent the corresponding experimental data reported by MEKALA e SANGWAI (2014), while the black and red solid lines respectively represent the predictions for the hydrate stability curve obtained from the C-G model and the vdW-P model.

Figure 4.2 and Figure 4.3 display the predictions for GAS 2 and GAS 3, respectively. In both cases, the natural gas mixture contains fractions of CO₂ and N₂ lower than 2% and 1%, respectively. The goal of this investigation was to confirm that the methodology employed in this work could accurately predict thermodynamic conditions in scenarios similar to Case Study 1.

The results for both GAS 2 and GAS 3 were satisfactory, showing good agreement with experimental data and the C-G model. The REP for the experimental data in GAS 2 and GAS 3 were 0.2373% and 0.2007%, respectively. When the C-G model was used as a reference, the REP were 0.3535% for GAS 2 and 0.2933% for GAS 3.

This result implies that the C-G model and the vdW-P model exhibit similar performances when dealing with natural gas with a low fraction of CO₂ and N₂ at lower pressures (below 2MPa) and temperatures (between 273K and 296K).

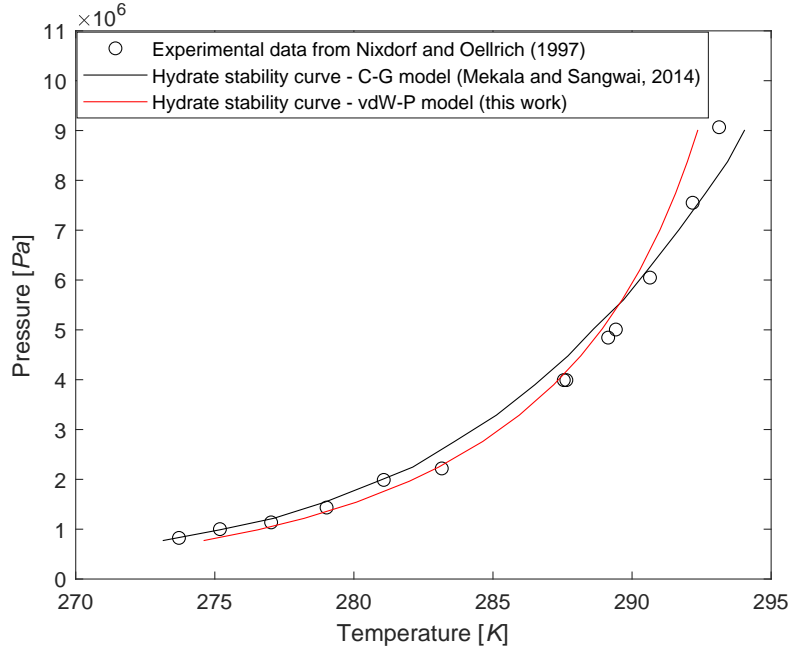


Figure 4.2: Case Study 2 Result: Sour natural gas containing 1.74% of CO_2 and 0.84% of N_2 . The black and red solid lines respectively represent the hydrate stability curves predicted by the C-G model (MEKALA e SANGWAI, 2014) and the vdW-P model (this work). The circles indicate the experimental data reported in MEKALA e SANGWAI (2014).

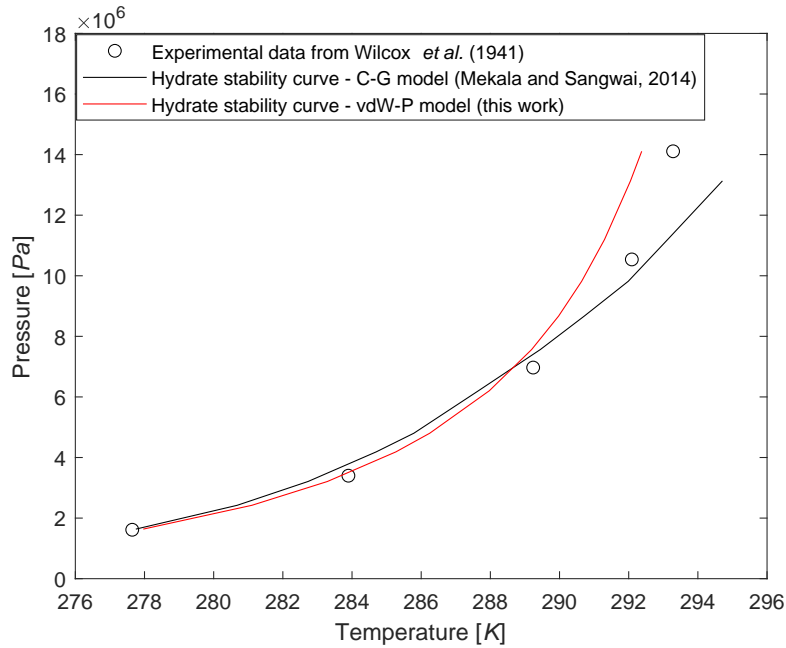


Figure 4.3: Case Study 2 Result: Sour natural gas containing 0.51% of CO_2 and 0.43% of N_2 . The black and red solid lines respectively represent the hydrate stability curves predicted by the C-G model (MEKALA e SANGWAI, 2014) and the vdW-P model (this work). The circles indicate the experimental data reported in MEKALA e SANGWAI (2014).

The subsequent investigations aimed to explore the impacts of increasing the composition of N_2 , CO_2 , and H_2S , separately. Figure 4.4 illustrates the predictions for GAS 1, which contains a higher fraction of CO_2 with the absence of N_2 and H_2S . The average relative errors compared to experimental data and the C-G model were 0.0845% and 0.2614%, respectively.

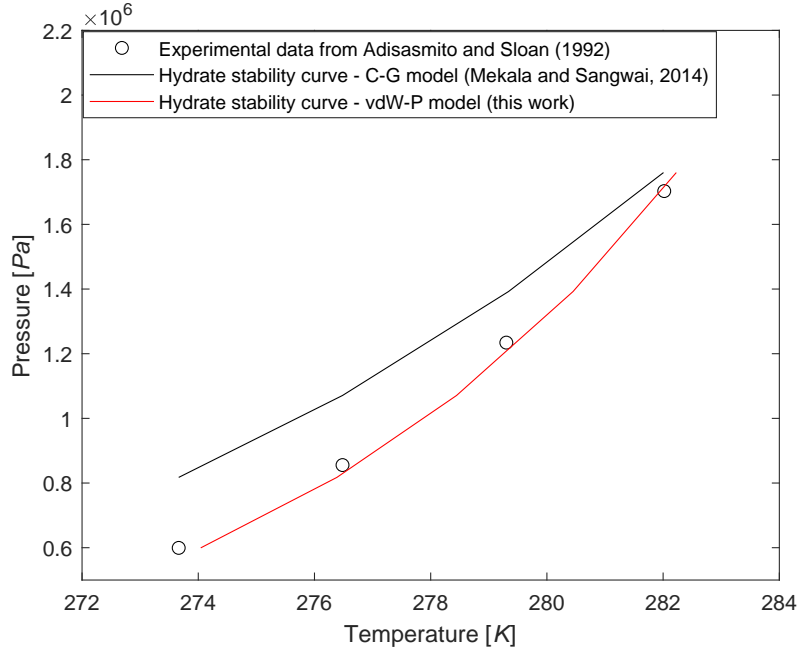


Figure 4.4: Case Study 2 Result: Sour natural gas containing 31.4% of CO_2 . The black and red solid lines respectively represent the hydrate stability curves predicted by the C-G model (MEKALA e SANGWAI, 2014) and the vdW-P model (this work). The circles indicate the experimental data reported in MEKALA e SANGWAI (2014).

The result suggests that the proposed methodology is suitable for natural gases with higher CO_2 content within the indicated temperature and pressure range. This is relevant given that the fluid composition bears similarities to that found in Brazilian fields. However, the experimental pressure range was relatively low compared to common operational conditions in offshore pipelines.

The objective of the following comparison was to evaluate the inaccuracies related to multiple occupancies when increasing the content of N_2 . Figure 4.5 depicts the predictions for GAS 4, which contains a higher fraction of N_2 , a low fraction of CO_2 , and no H_2S . The REP values, when compared to experimental data and the C-G model, were 1.0911% and 1.0376%, respectively.

The observed errors were larger than in previous examples; however, they remained below 1.1% for both references. These errors suggest that inaccuracies due to multiple occupancies become more pronounced in the vdW-P model with an increase in both temperature and pressure. As observed in Figure 4.5, the C-G model aligns with the experimental data, which implies that the use of the Kihara potential may improve prediction

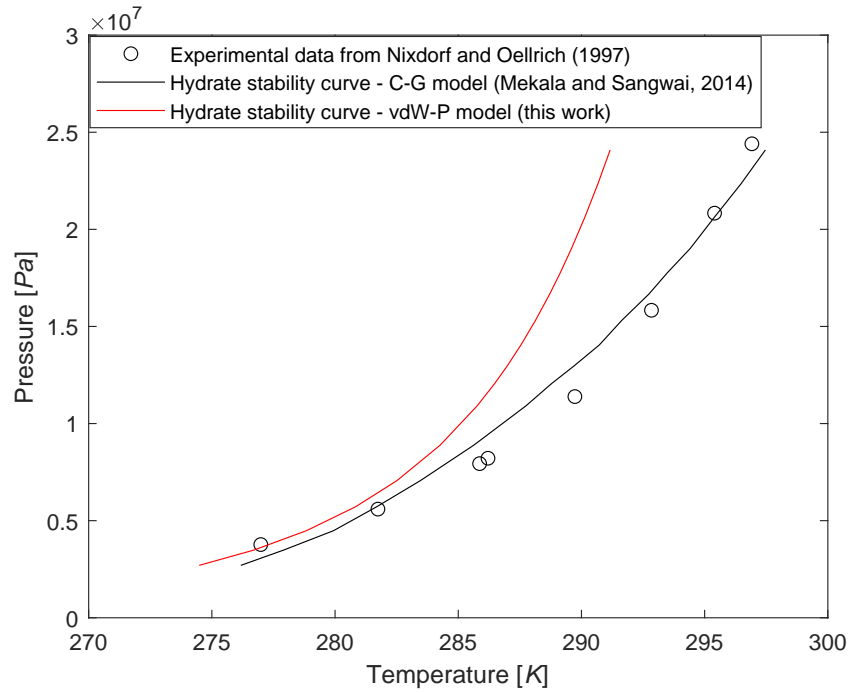


Figure 4.5: Case Study 2 Result: Sour natural gas containing 3.19% of CO₂ and 9.59% of N₂. The black and red solid lines respectively represent the hydrate stability curves predicted by the C-G model (MEKALA e SANGWAI, 2014) and the vdW-P model (this work). The circles indicate the experimental data reported in MEKALA e SANGWAI (2014).

accuracy in scenarios with larger amount of N₂.

Finally, the last investigation aimed to evaluate the impact of an increased concentration of H₂S, which is a polar molecule and can act as an acid in solution. Figures 4.6 and 4.7 present the predictions for GAS 5 and GAS 6, which contain CO₂ and H₂S. The average relative errors when compared with experimental data and the C-G model were less than 1.16% and 1.31% in each reference, respectively.

Once again, the C-G model aligned with the experimental data, reinforcing the advantage of employing the Kihara potential in these scenarios. Another approach is to use the CPA EoS to predict the interaction between polar molecules and the impact of ions.

The available experimental data were characterized by a pressure range lower than that typically observed in offshore reservoirs; however, the objective of analyzing model performance was effectively achieved. Inaccuracies mentioned in the literature caused by the presence of CO₂, N₂, and H₂S guest molecules when predicting the hydrate stability curve using the vdW-P model could be observed.

Upon analyzing the relative error between experimental data, predictions from the C-G model employed by MEKALA e SANGWAI (2014), and predictions generated in this work using the vdW-P model implemented in *MATLAB*[®], it becomes apparent that the approach of this work demonstrated a larger error when handling higher quantities of N₂ and H₂S.

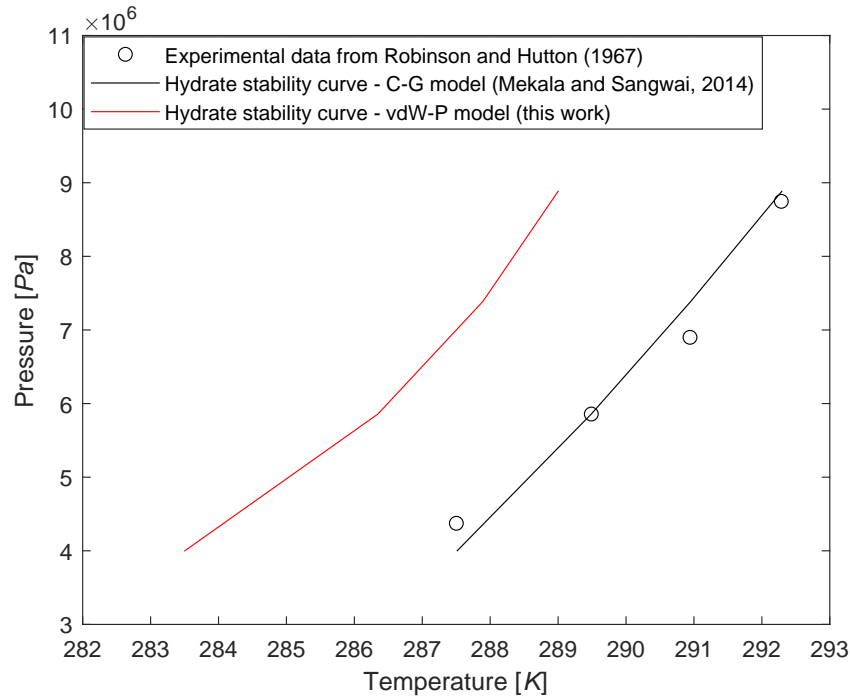


Figure 4.6: Case Study 2 Result: Sour natural gas containing 12.6% of CO₂ and 5.4% of H₂S. The black and red solid lines respectively represent the hydrate stability curves predicted by the C-G model (MEKALA e SANGWAI, 2014) and the vdW-P model (this work). The circles indicate the experimental data reported in MEKALA e SANGWAI (2014).

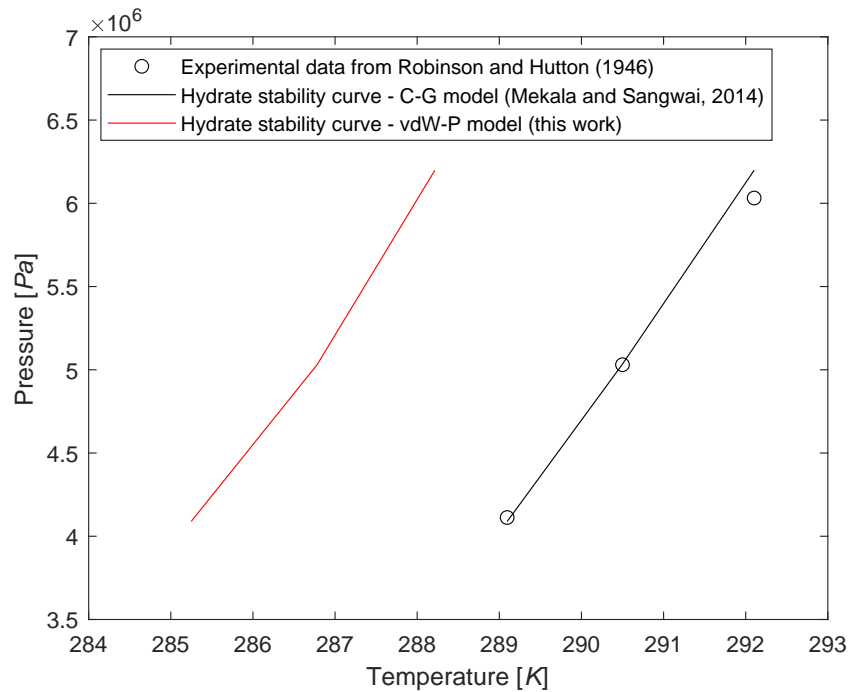


Figure 4.7: Case Study 2 Result: Sour natural gas containing 12% of CO₂ and 8% of H₂S. The black and red solid lines respectively represent the hydrate stability curves predicted by the C-G model (MEKALA e SANGWAI, 2014) and the vdW-P model (this work). The circles indicate the experimental data reported in MEKALA e SANGWAI (2014).

On the other hand, the C-G model presented better results, reinforcing the potential of Kihara potential in predicting the Langmuir coefficients in such scenarios. Further research could address these limitations by utilizing the same Kihara potential and expand the methodology to other flow assurance scenarios.

This advancement would enable the prediction of the hydrate stability curve for typical oil found in the Santos Basin, which contains a significant amount of CO₂ and impurities. The fluid utilized in Case Studies 3, 4, and 5 does not contain any significant content of these guest components, which often introduce inaccuracies and complex scenarios. Therefore, the chosen methodology appears suitable for the objectives of this work.

4.3 Case Study 3

Most of the works in the literature dedicated to predicting hydrate formation use simplified models to obtain fluid properties, which often deviate significantly from real-world scenarios. To contribute to prediction closer to real-world operations, this work suggests applying the thermodynamic models used by GUEDES (2015) and the three-phase flash proposed by GUEDES (2023) to obtain the fluid properties used as input in the hydrodynamic model.

The fluids used in Case Studies 3, 4, and 5 were based on Caratinga field data available in SJÖBLOM *et al.* (2010) and RAO (2013). The original fluid was adapted with a pseudo-component that comprised twenty-five heavy fractions. Moreover, the resin fraction presented in the original fluid was neglected to fit the correlations used in this work's methodology. The code implemented in *MATLAB*[®] for this work and the commercial software *Multiflash*[™] applied the same thermodynamic model according to the recommendation in Section 3.1.2.

The methodology of this work generated a table containing the compositions and fractions of the three phases for a range of temperatures and pressure suitable for further hydrodynamic simulation. These table values were interpolated to calculate the fluid properties corresponding to the multi-phase flow pressure and temperature along the pipeline.

Similarly, *Multiflash*[™] generated the fluid properties table for a range of temperature and pressure that was input into *OLGA*[®]. The software *OLGA*[®] employs the TFM to determine the operating condition in the steady-state simulation, while this work utilizes the DFM, implemented in *MATLAB*[®].

Figure 4.8 presents a comparison of the vapor void fraction profiles along the pipeline, obtained from *OLGA*[®] (black solid lines) and *MATLAB*[®] (red solid lines). This figure clearly illustrates that in the flowline section (prior to the 14km mark), the vapor fraction profile predicted by *MATLAB*[®] initially begins as non-zero but subsequently reduces to zero, while the results from *OLGA*[®] remain non-zero, but less than 0.05.

In Case Study 4, it will be shown that the temperature and pressure profiles along

the flowlines section from *OLGA*[®] and *MATLAB*[®] are almost identical. However, when considering the results derived from the thermodynamic methodology to obtain the fluid properties, the vapor void fraction profile along the pipeline becomes important for the comprehension of subsequent results.

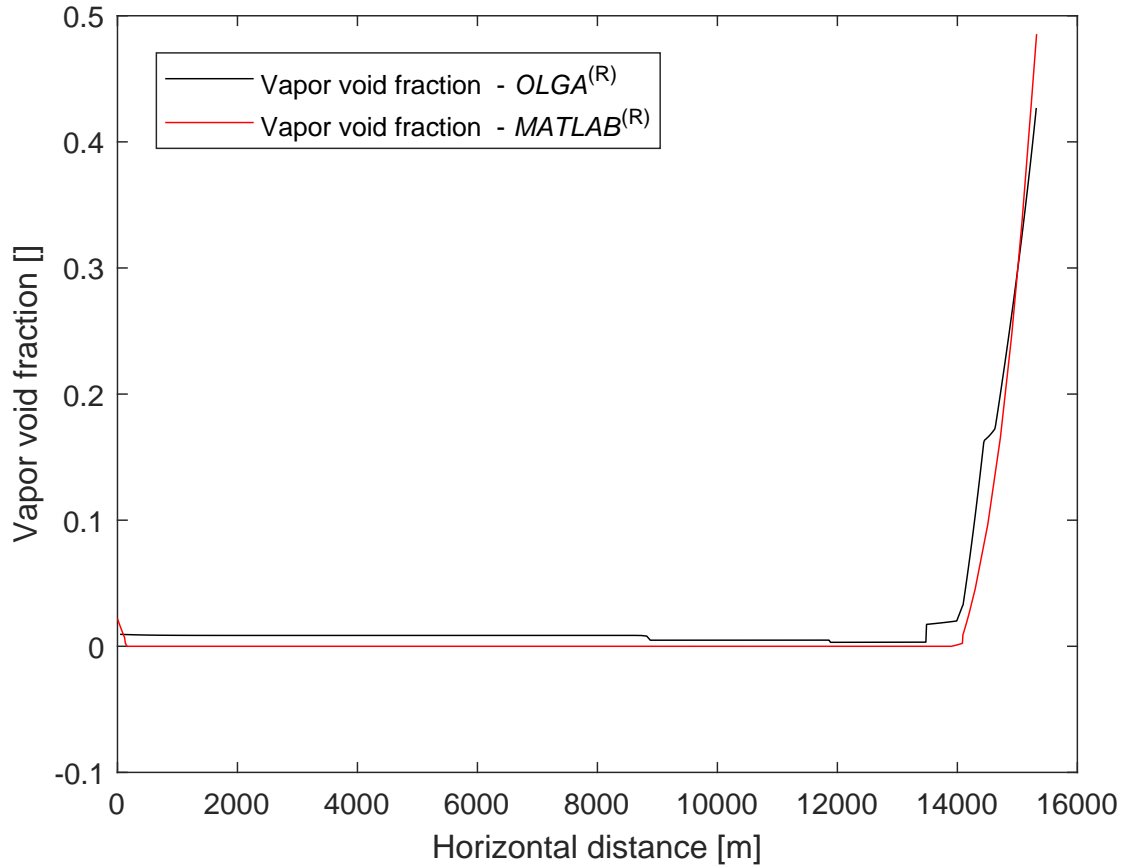


Figure 4.8: Comparison of the vapor void fraction profile along the pipeline for the steady-state flow simulation based on Caratinga field well geometry and fluid properties. The solid black line represents the gas phase fraction obtained from *OLGA*[®] using fluid properties data from *Multiflash*TM. The solid red line shows the result obtained from this work implementing the proposed methodology in *MATLAB*[®].

Typically, for young wells, the fluid is saturated at reservoir conditions. However, due to the simplifications employed in this work, the starting conditions predicted in *Multiflash*TM were multiphasic. This observation suggests that, for similar temperature and pressure, the three-phase flash calculation in *Multiflash*TM was more sensitive to vapor phase appearance, even in the flowline. Conversely, the methodology of this work for three-phase flash calculations was unable to predict this low amount of gas.

Figure 4.9 – Figure 4.11 show the phase properties profile (*i.e.*, fraction, viscosity, density, and enthalpy) for vapor, liquid oil, and liquid water, respectively. In all the figures the results for properties profile obtained from *OLGA*[®] and *MATLAB*[®] are represented by the solid black and red lines, respectively.

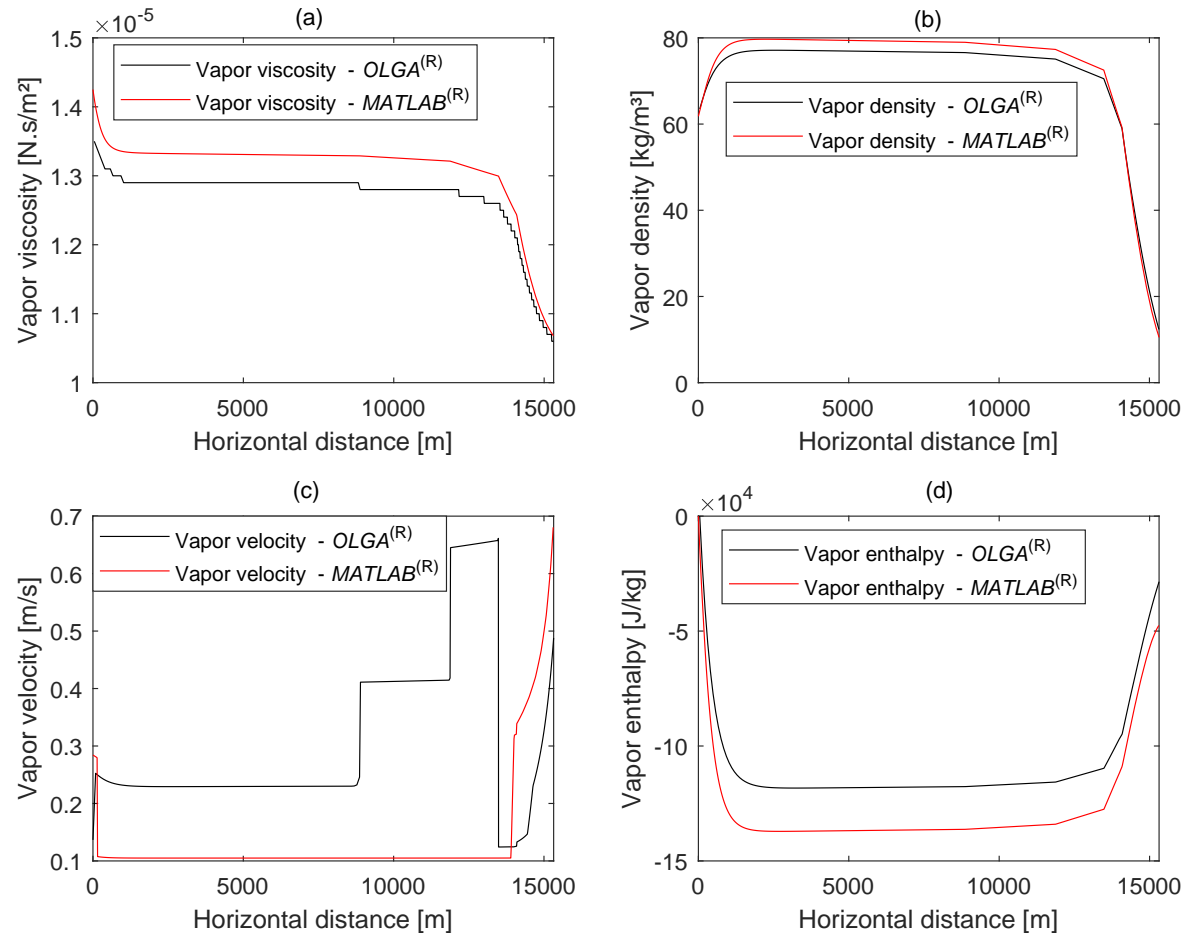


Figure 4.9: Comparison of vapor phase (a) viscosity profile, (b) density profile, (c) velocity profile, and (d) enthalpy profile along the pipeline for the steady-state flow simulation based on Caratinga field well geometry and fluid properties. The solid black line represents the results obtained from *OLGA*[®] using fluid properties data from *Multiflash*[™]. The solid red line shows the results obtained from this work implementing the proposed methodology in *MATLAB*[®].

The vapor phase results presented in Figure 4.9 suggest that the property profiles obtained using the EoS PR in *MATLAB*[®] and *Multiflash*TM were consistent and exhibited similar behavior in response to changes in temperature and pressure along the pipeline.

This consistency implies that the parameters used in the correlations for gas phase properties were similar. The most notable divergence was observed in the vapor velocity, as displayed in Figure 4.9 (c). This behavior is a consequence of the high sensitivity of *OLGA*[®] simulation to small changes in gas fraction observed in Figure 4.8.

The sensitivity to flow pattern and vapor fraction in *OLGA*[®] simulation can also be discerned in the liquid oil and aqueous phase as demonstrated in Figure 4.10 (a) and Figure 4.11 (a), respectively.

Furthermore, when using *Multiflash*TM as a reference, Figures 4.10 (a) and 4.11 (a) imply that liquid fractions could be under-predicted by up to 15% in the three-phase flash. This discrepancy was observed due to the difference between the predicted aqueous and oil fractions from *OLGA*[®] and *MATLAB*[®]. This degree of imprecision in the three-phase flash prediction can directly affect the mixture properties utilized in the DFM.

With regard to density calculated using the PR EoS show in Figure 4.9 (b), Figure 4.10 (c) and Figure 4.11 (c), the results obtained from *MATLAB*[®] and *Multiflash*TM were consistent considering the response to changes in temperature and pressure. The discrepancy in the vapor, oil, and water enthalpy results, show in Figure 4.9 (d), Figure 4.10 (d) and Figure 4.11 (d), was likely attributable to differences in their reference states.

In Figure 4.11 (b), the water viscosity correlation implemented in *MATLAB*[®] exhibited significant sensitivity to temperature changes, predominantly seen in the riser sections. Further investigation is recommended to assure its applicability to the aqueous phase.

The higher WC applied in this work, compared to the one used in GUEDES (2023), allowed for the identification of this limitation in the three-phase flash algorithm methodology, which also impacts mixture properties in the hydrodynamic methodology. A suggestion for future work, building on observations made in Case Study 2, involves the utilization of a different EoS to enhance the accuracy of the three-phase flash model.

A recommendation for future work is to implement the CPA EoS in flash calculations. This could potentially enhance the accuracy of hydrate stability curve predictions in systems containing higher amounts of H₂S, as well as account for complexities associated with a larger water cut, such as water-hydrocarbon interactions and polar effects.

In accordance with the objectives of this case study, the results were satisfactory. However, the three-phase flash model methodology employed requires further refinement. While phase compositions corresponded to the values observed in *Multiflash*TM, the separation factors were consistently under-predicted.

Moreover, from a practical perspective, there is room for improvement to reduce the time required for generating the table with the fluid properties. While *Multiflash*TM required a few minutes the *MATLAB*[®] approach necessitated several hours.

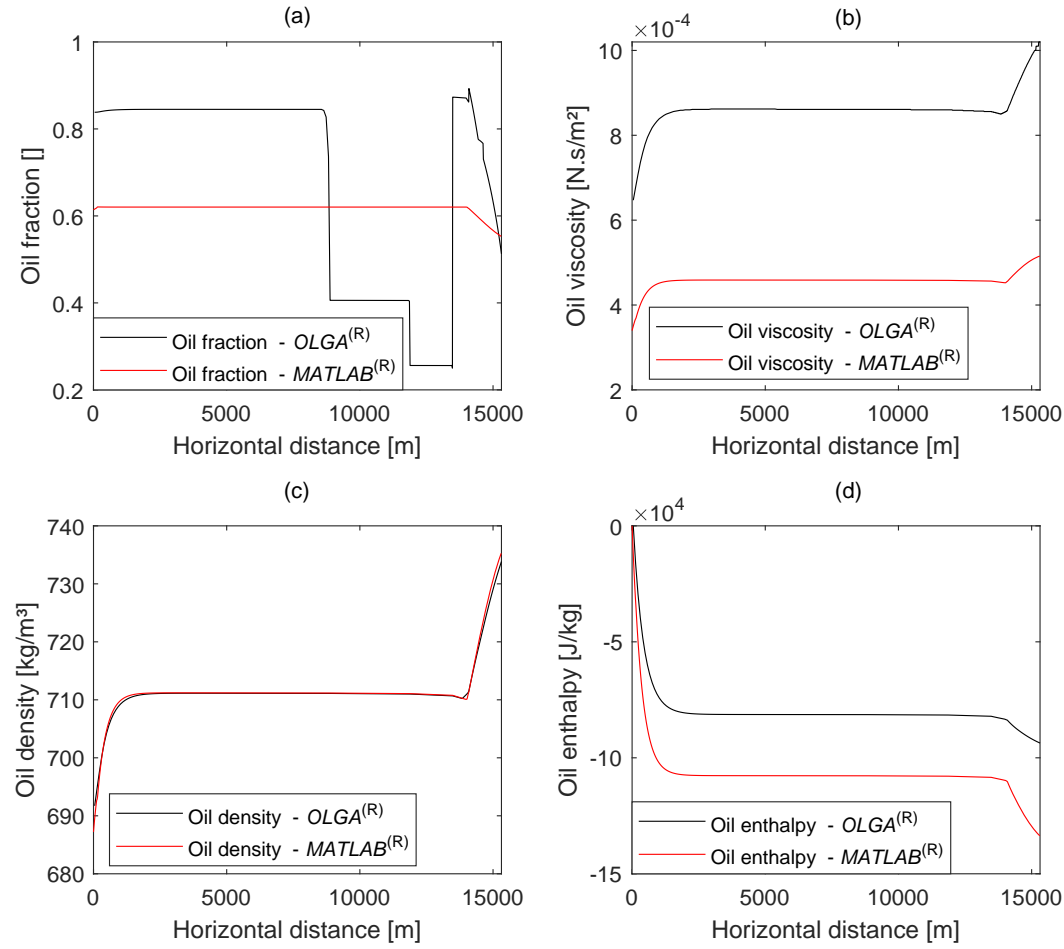


Figure 4.10: Comparison of oil phase (a) fraction, (b) viscosity profile, (c) density profile, and (d) enthalpy profile along the pipeline for the steady-state flow simulation based on Caratinga field well geometry and fluid properties. The solid black line represents the results obtained from *OLGA*[®] using fluid properties data from *Multiflash*[™]. The solid red line shows the results obtained from this work implementing the proposed methodology in *MATLAB*[®].

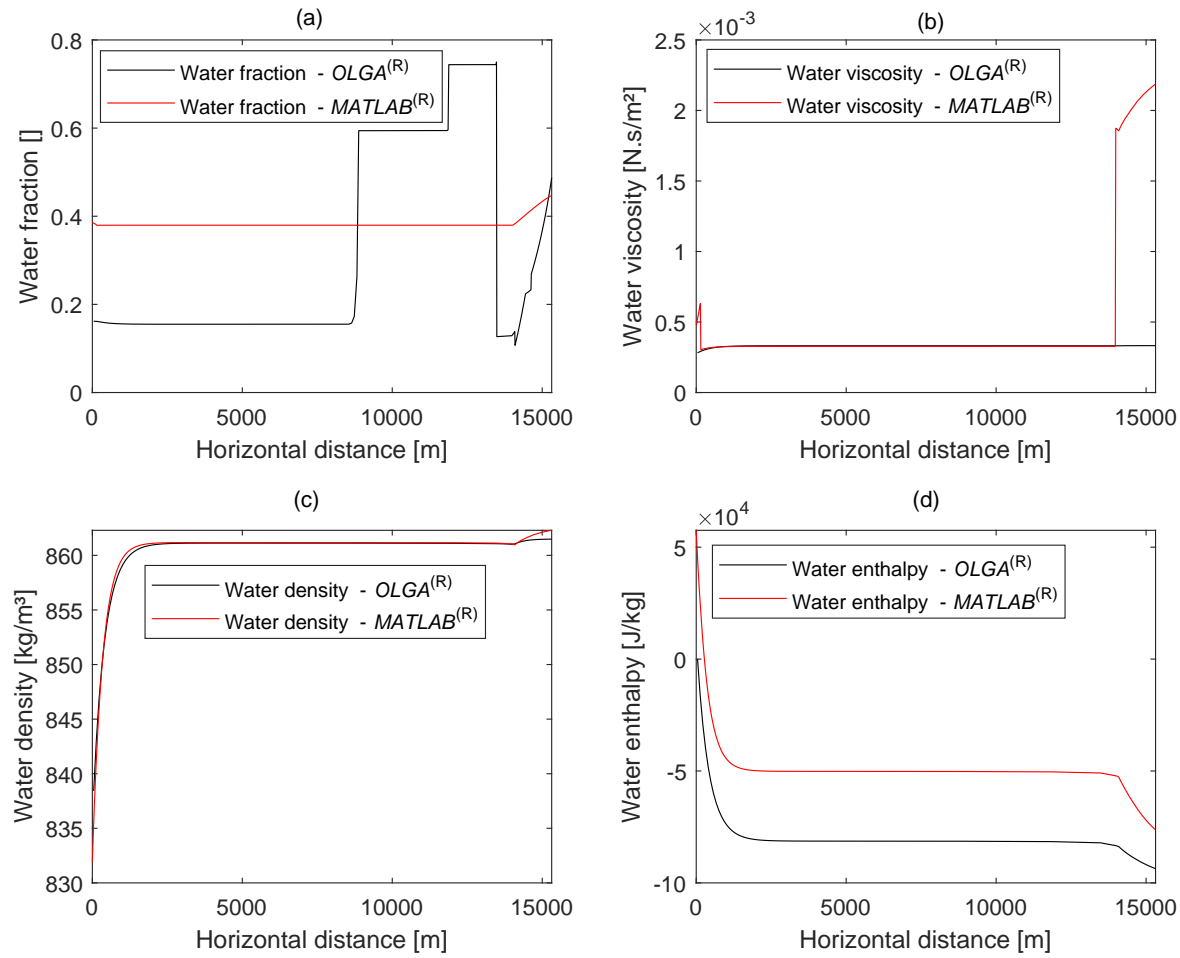


Figure 4.11: Comparison of aqueous phase ((a) fraction, (b) viscosity profile, (c) density profile, and (d) enthalpy profile along the pipeline for the steady-state flow simulation based on Caratinga field well geometry and fluid properties. The solid black line represents the results obtained from *OLGA*[®] using fluid properties data from *Multiflash*[™]. The solid red line shows the results obtained from this work implementing the proposed methodology in *MATLAB*[®].

4.4 Case Study 4

Case Study 4 evaluated the performance of the DFM implemented in *MATLAB*[®], with a focus on (1) reproducing the operational conditions reported in ZERPA (2013) and (2) measuring the agreement with *OLGA*[®] using the same steady-state inputs described in Section 3.2.7. Whereas ZERPA (2013) used the original Caratinga fluid, both this study and the comparison in *OLGA*[®] applied the modified fluid detailed in Section 3.1.4.

Figure 4.12 illustrates the comparison between operational conditions reported in ZERPA (2013) and the results obtained from both *OLGA*[®] and *MATLAB*[®], according to the inputs described in Section 3.2.7. The illustration also includes the hydrate stability curves for the modified fluid obtained from *Multiflash*[™] and *MATLAB*[®].

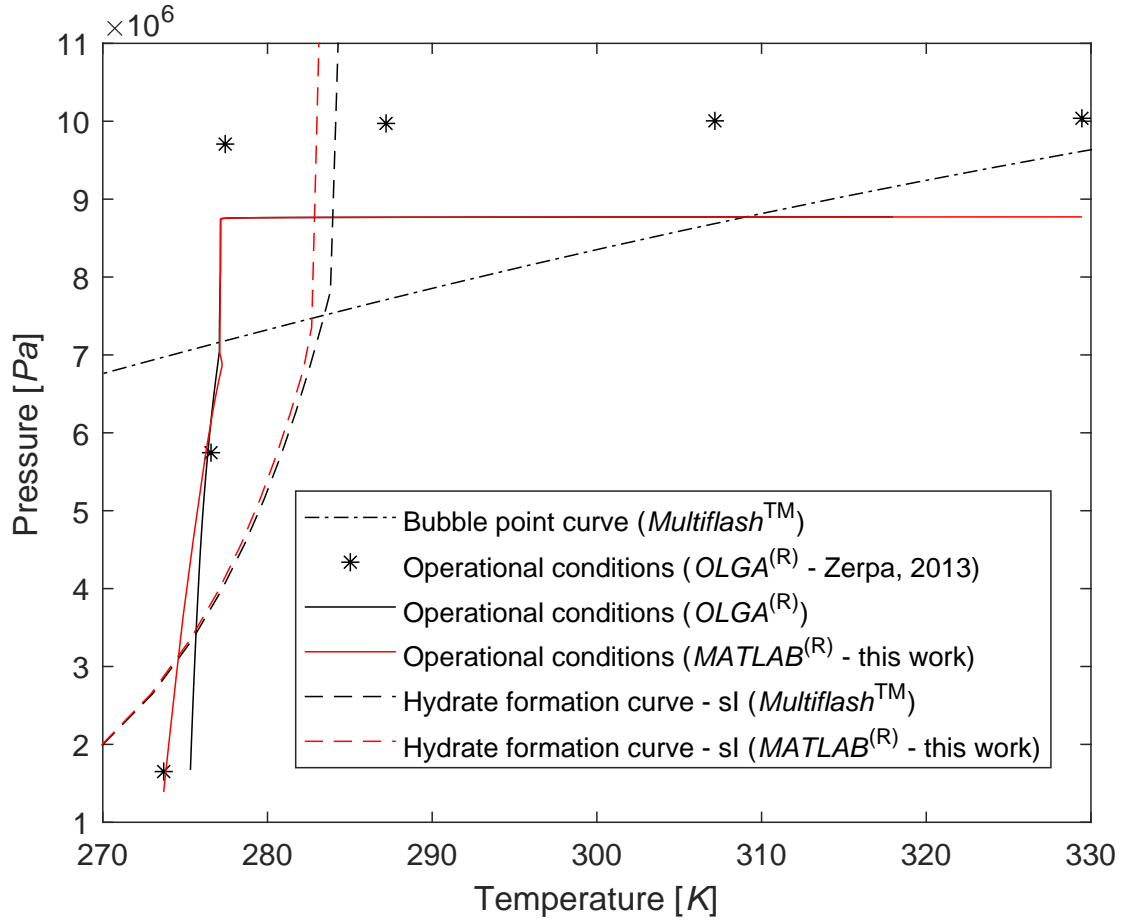


Figure 4.12: Comparison between the steady-state operational conditions of Caratinga field reported in ZERPA (2013) and the pressure vs. temperature profile for the modified fluid obtained from *OLGA*[®] and *MATLAB*[®]. The dash-dotted line represents bubble point curve obtained from *Multiflash*[™] for the modified fluid. The asterisk indicates the operational conditions reported in ZERPA (2013) for the original Caratinga fluid using the software *OLGA*[®]. The black and red solid lines represent the operational conditions of the modified fluid obtained, respectively, from *OLGA*[®] and *MATLAB*[®]. The black and red dashed lines represent the hydrate stability obtained, respectively, from *Multiflash*[™] and *MATLAB*[®].

In Figure 4.12, the dash-dotted line intersecting the operational conditions represents the bubble point curve for the modified fluid, obtained from *Multiflash*TM. Additionally, the hydrate stability curves for the modified fluid, derived from *Multiflash*TM and *MATLAB*[®], are shown by the black and red dashed lines, respectively.

The prediction of hydrate stability assumes methane as the guest molecule, forming sI structure. The results align with those of Case Study 1, indicating an average error of less than 0.64% between the commercial software and the approach taken in this work.

In Figure 4.12, the asterisk indicates the operational conditions reported in ZERPA (2013) for the original Caratinga fluid using the software *OLGA*[®]. The black and red solid lines represent the operational conditions of the modified fluid obtained, respectively, from *OLGA*[®] and *MATLAB*[®].

Taking the results from ZERPA (2013) (represented by the asterisks) as the reference, the original fluid started in a saturated state and transitioned to a multi-phase state near the riser region. This behavior aligns with the characteristics of oil-dominated systems discussed in Section 2.3.1.

On the other hand, the modified fluid initially exhibited multi-phase flow, subsequently transitioning to a saturated state due to the temperature drop in the high-pressure flowline. Approaching the riser, the depressurization conditions facilitated vaporization, resulting in the multi-phase flow.

The observed 10% discrepancy in pressure for the original fluid, shown in Figure 4.12, may be a consequence of the modification applied to the fluid. Despite this difference, it did not have a significant impact on the study since the gas remained outside the area where hydrate formation occurs.

In Figure 4.12, the discrepancy in temperature drop between *MATLAB*[®] and *OLGA*[®] observed in the riser section likely originates from the under-prediction of phase fractions observed in Case Study 3. Typically, liquids possess a higher heat capacity and are less susceptible to temperature variations. Considering that the methodology of this study consistently under-predicted the liquid phase fraction in the pipeline, it is plausible that the overall heat capacity of the mixture was lower in comparison to the one in *OLGA*[®] combined with *Multiflash*TM data.

With regard to the impact of the vapor phase noted in Case Study 3, TFM in combination with *Multiflash*TM demonstrated higher fluctuation in the prediction of oil and liquid phase fractions. Conversely, the DFM approach employed in *MATLAB*[®] delivered stable results across the entirety of the pipeline geometry, as illustrated in Figure 4.10 (a) and Figure 4.11 (a).

These fluctuations could be attributed to the flow pattern predicted by *OLGA*[®] for this pipeline segment. In the proposed methodology, the slip drift velocity, presented in Section 3.2.6, is not dependent on flow patterns but takes into account pipe geometry and fluid properties.

Despite these observations, the temperature and pressure profiles obtained from *OLGA*[®] via TFM and from *MATLAB*[®] via DFM were congruent. This preliminary comparison demonstrated the ability of DFM to achieve results comparable to those derived from TFM in *OLGA*[®], as corroborated by previous studies (GUEDES, 2023, GÓES *et al.*, 2023, TEIXEIRA, 2016). The following investigation aimed to verify the sections favorable for hydrate formation, taking into consideration the criteria specified in Sections 3.1.1 and 3.2.3.

Figure 4.13 shows the temperature profile along the pipeline for the steady-state simulation based on Caratinga field data. The asterisks refer to the temperature profile along the pipeline reported in ZERPA (2013). The red solid line represents the temperature profile, while the red dashed line refers to the hydrates equilibrium temperature, both obtained from *MATLAB*[®].

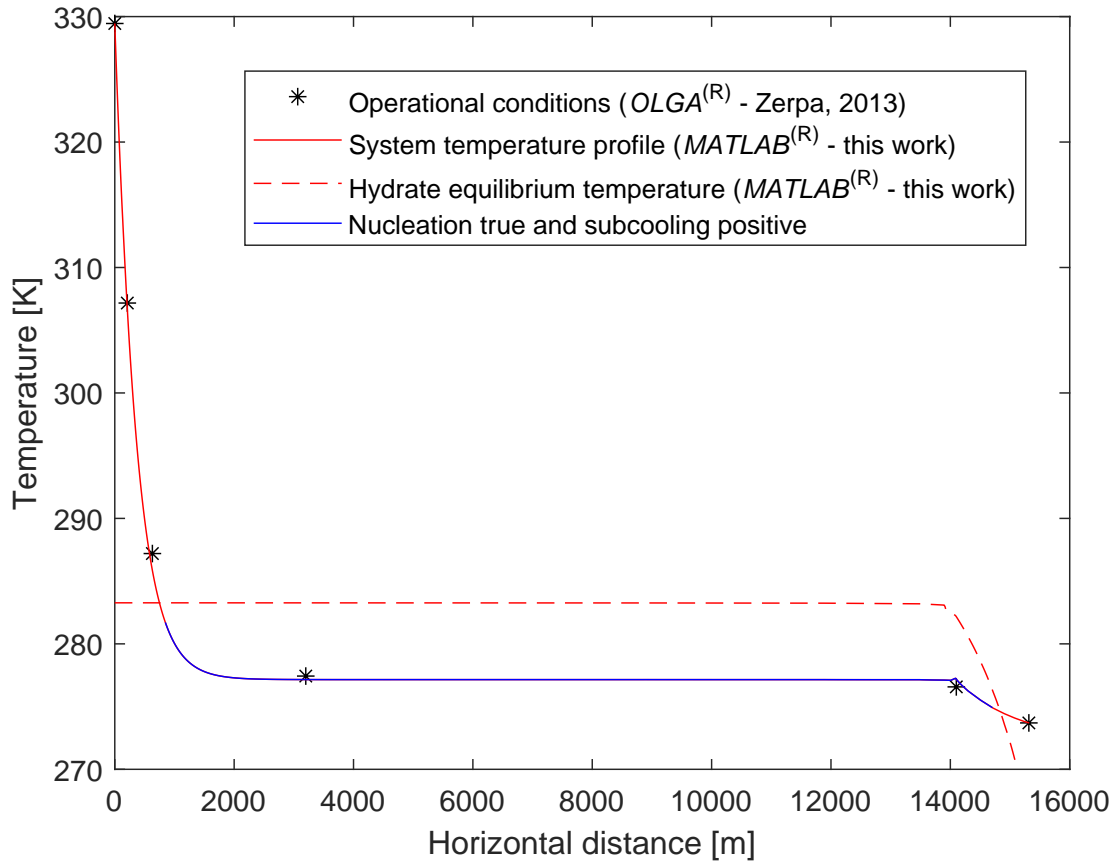


Figure 4.13: Temperature profile along the pipeline obtained for steady-state simulation. The asterisk indicates the temperature along the pipeline reported in ZERPA (2013) for the original Caratinga fluid using the software *OLGA*[®]. The red solid and dashed lines represent, respectively, the fluid temperature profile and the equilibrium temperature for hydrate formation, both obtained from this work using *MATLAB*[®]. The blue solid curve highlights the section where the nucleation exceeds 3.5K and where positive subcooling is observed.

The blue solid line on the temperature profile delineates the pipeline section where the

subcooling exceeds $3.5K$, meeting the criterion to activate the hydrate formation kinetic model. However, the activation of the kinetic model should be confined to regions where the thermodynamic conditions are also satisfied.

Figure 4.14 presents the operational conditions in a steady-state predicted by this work methodology, implemented in *MATLAB*[®]. The dash-dotted line intersecting the operational conditions corresponds to the bubble point curve obtained from *Multiflash*[™]. The red solid and dashed lines represent the pressure vs. temperature profile along the pipeline and the hydrate formation curve, respectively.

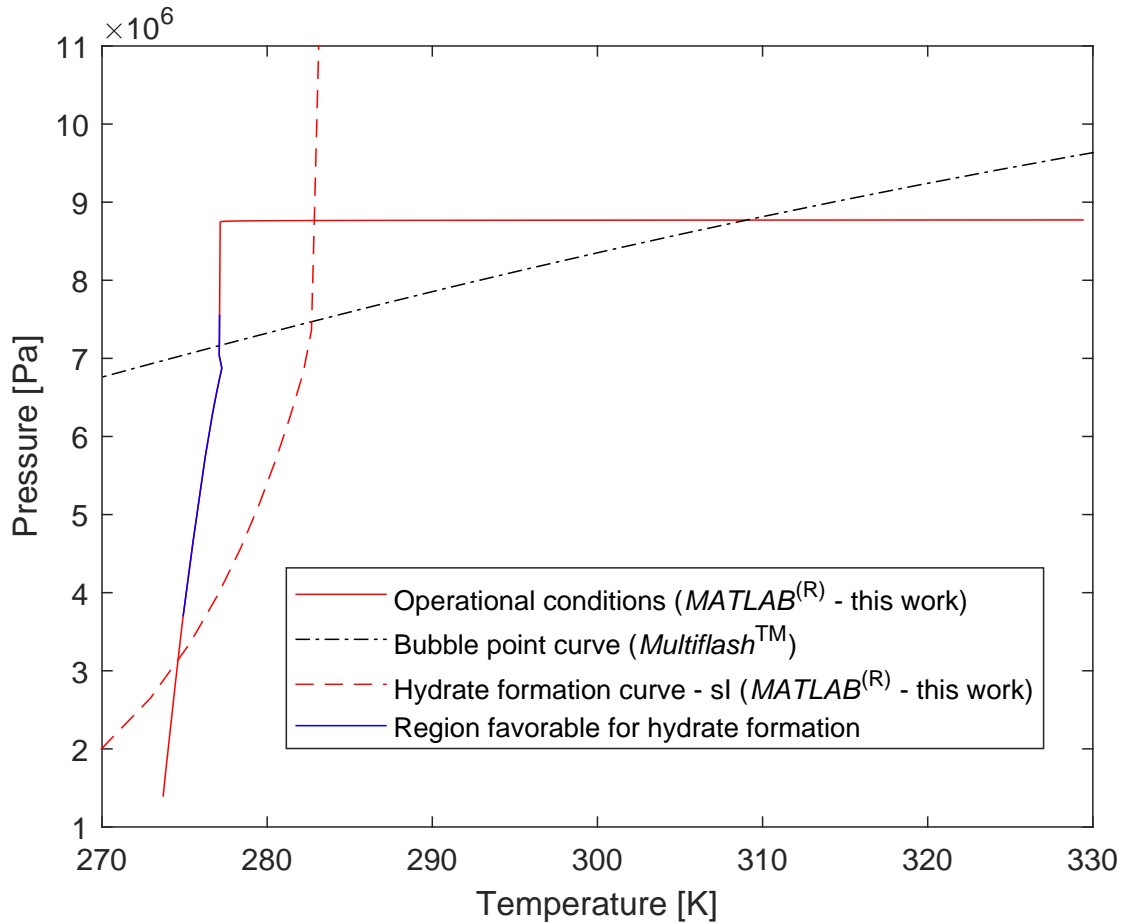


Figure 4.14: Operational conditions and the hydrate stability curve were obtained from this work, implemented in *MATLAB*[®], for the modified fluid and Caratinga field geometry. The red solid and dashed lines represent the pressure vs. temperature profile along the pipeline and the hydrate formation curve, respectively. The dash-dotted line indicates the bubble point curve for the modified fluid obtained from *Multiflash*[™]. The blue line highlights the pipeline section where the kinetics of hydrate formation satisfy the activation criteria.

The highlighted blue solid line represents the section where the following criteria are met: (1) the operational conditions are within the hydrate formation zone, (2) the critical subcooling was reached, and (3) there are free gas and water phases. The sequential application of these criteria prevents the erroneous activation of the hydrate kinetic model

in the flowline section that satisfies the second and third criteria.

As illustrated in Figure 4.14, it is apparent that near the bubble curve, the phase transition predicted by our methodology is overestimated in comparison to *Multiflash*TM. This observation reinforces the recommendations made in Case Study 3 to improve the three-phase flash accuracy. Given that the steady-state DFM can predict the regions favorable for hydrate formation, the final case study aims to quantify the mass of hydrates formed and dissociated, as well as evaluate the risk of pipeline plugging.

4.5 Case Study 5

In this case study, the kinetic model described in Section 3.2.3 was applied to analyze the risk of plugging in the riser section. Figure 4.15 compared the temperature profiles for the steady-state simulation, both with and without hydrate formation in the riser section. In addition, the figure includes the curve for the hydrate volumetric fraction obtained from the hydrodynamic model, as well as comments to guide understanding of the co-occurring phenomena.

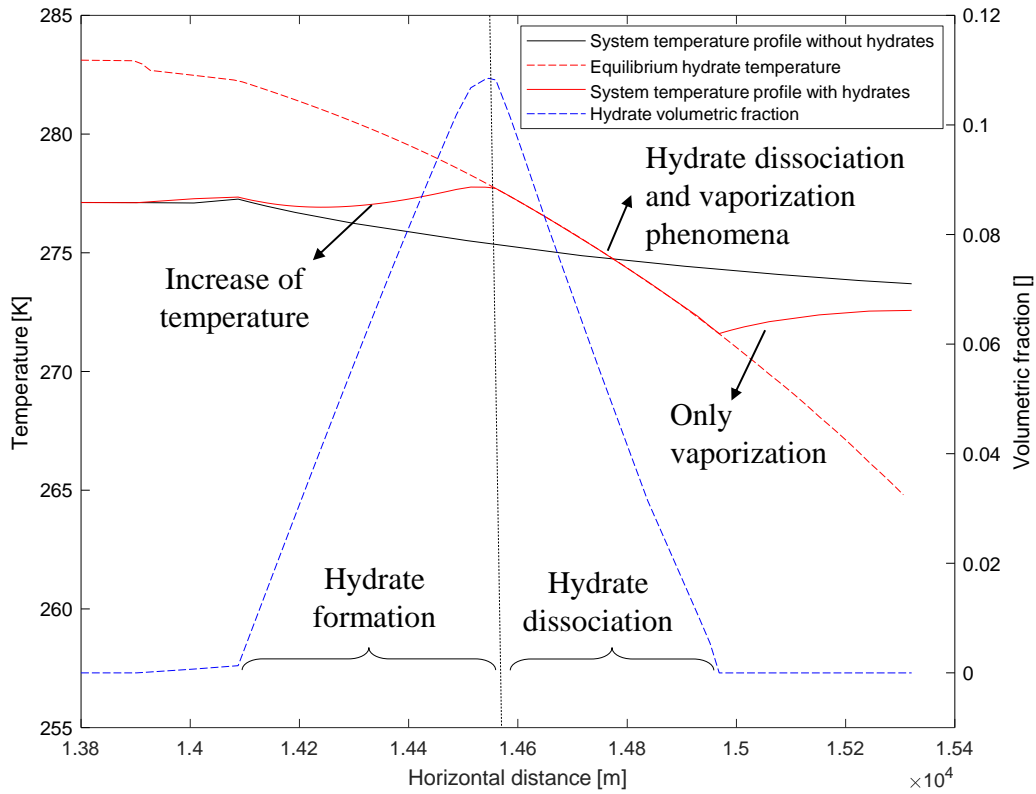


Figure 4.15: Comparison between temperature profiles in steady-state simulations with and without hydrate formation in the riser section, obtained from this work using the methodology implemented in *MATLAB*[®]. The black and red solid lines represent the temperature profiles along the riser, respectively, without and with hydrate formation. The red dashed line shows the hydrate formation equilibrium temperature and the blue dashed line refers to the hydrate volumetric fraction.

The vertical black dashed lines delineate the boundary where hydrate formation ends and hydrate dissociation begins. The temperature profiles obtained from the steady-state energy conservative equation with and without hydrates formation are shown as the black and red solid lines, respectively. The red and blue dashed lines show, respectively, the hydrate formation equilibrium temperature and the hydrate volumetric fraction.

On the left side of the boundary, upon activation of the kinetic model, it is possible to observe an increase in hydrate volumetric fraction obtained from the hydrate continuity equation in DFM. In the riser section, energy is released due to hydrate formation, while energy is absorbed due to oil vaporization.

The mixture energy balance equation in the DFM accounts for the energy released post hydrate formation and the energy consumed during vaporization. The difference in magnitude between the temperatures represented by the red and black solid lines illustrates this phenomenon during hydrate formation.

The rate of gas consumption decreases as the subcooling in the riser section drops due to (1) the decrease in hydrate equilibrium temperature and (2) the reduction in system temperature caused by vaporization.

Conversely, on the right side, when the subcooling becomes negative and the operational conditions shift outside the hydrate formation curve, the dissociation model is activated by the change in intrinsic kinetic constants, as outlined in Section 3.2.3. During the dissociation process, the hydrates melt, absorbing system energy proportional to the subcooling and particle diameter. A rapid decrease in temperature is noticeable due to the simultaneous phenomena of vaporization and hydrate dissociation in the riser.

Once all the hydrates have melted, the hydrate volumetric fraction returns to zero, and the DFM describes the multi-phase flow containing liquid and gas. This study indicates a low risk of plugging because the hydrates that formed were dissociated in the riser before plugging could occur.

The kinetic model successfully accounts for the phenomena of hydrate formation and dissociation. Consequently, the subsequent analysis evaluated the impact of the agglomeration model detailed in Section 3.2.5. Figure 4.16 contrasts the hydrate volumetric fraction derived from DFM with the effective hydrate volumetric fraction established by Eq. (2.28).

This comparison indicated identical values, likely attributed to the sensitivity of the agglomeration model to the ratio between the agglomerate diameter and particle diameter. As a result, there was no adjustment to the effective hydrate volume fraction using the methodology outlined in Section 2.3.5.

Additionally, Figure 4.17 demonstrates the influence of the effective hydrate volumetric fraction on the relative viscosity. The relative viscosity, a dimensionless number, represents the ratio of oil viscosity to dispersion viscosity. When the hydrate volumetric fraction reached its peak, the relative viscosity was approximately 1.4.

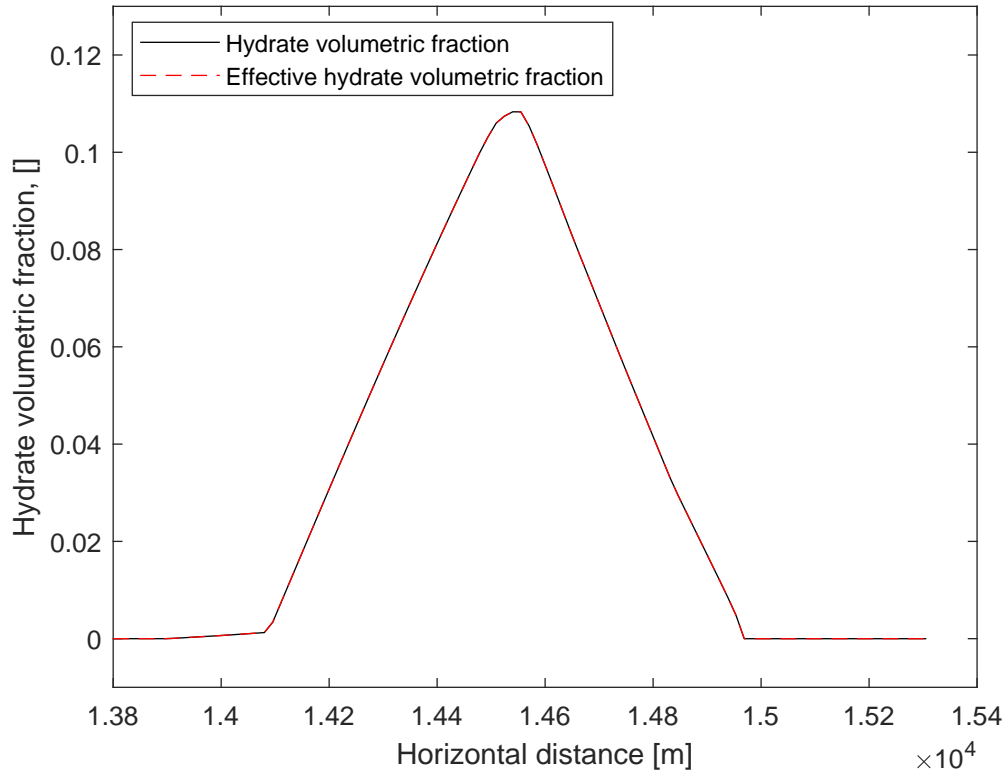


Figure 4.16: Comparison between the hydrate volumetric fraction derived from the mass conservation equations (black solid line) and the effective hydrate volume fraction obtained from the agglomerate model (red dashed line) in the riser section.

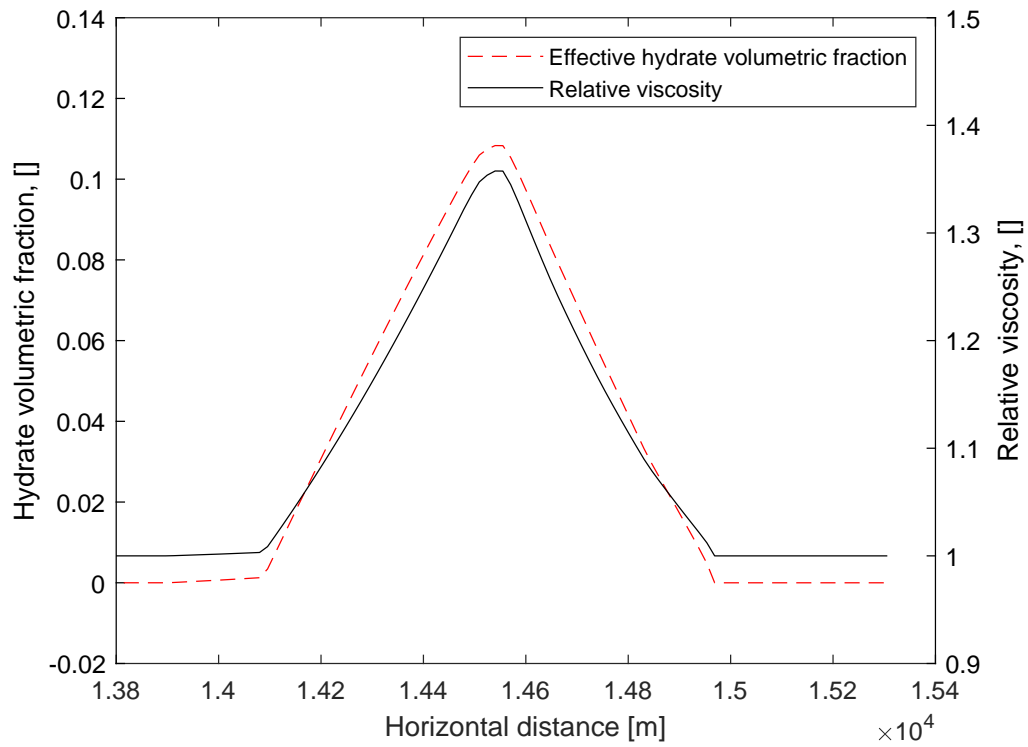


Figure 4.17: Effects of hydrate volumetric fraction in relative viscosity observed in the riser section. The solid black line show the relative viscosity and the dashed red line refer to the effective hydrate volumetric fraction.

Consequently, the pressure drop due to hydrate formation was not expressive because the impact in relative viscosity was not significant. This observation agrees with the literature observation, which suggests developing an agglomeration model that includes the effect of particle shape and roughness to estimate the effective volume fraction. This case presented a low-risk plugging, which could be solved using insulation – the standard avoidance management in pipelines.

The kinetic model applied in this work accounts for methane hydrate consumption and used properties of the sI structure. In addition, the intrinsic kinetic model did not comprise other mechanisms involved in hydrate formation was used. Furthermore, the hydrodynamic model used was in a steady state, which limits the applicability of remediation strategies that require a time-dependent aspect of hydrates formation.

Nevertheless, it was demonstrated that for a homogeneous dispersion, the DFM in the steady state, when coupled with a simple kinetic model, is capable of replicating hydrate formation and dissociation phenomena, corresponding with observations reported in the literature.

Given the simultaneous simulation of kinetic and thermodynamic aspects, some suggestions for improvement in future works include: (1) calculating the hydrate number from the fractional occupancies provided by the vdW-P model instead of using the constant value reported in the literature, (2) expanding the model for dynamic simulations, and (3) applying the kinetic model proposed by BASSANI *et al.* (2019) to perform remediation strategies in oil-dominated systems.

Chapter 5

Conclusion

This work aligns with the trend of research groups developing their own flow assurance tools. Concerning this statement, the Drift-Flux Model was formulated as a differential-algebraic system solved by numerical integration. It was then applied to perform steady-state simulations to predict operational conditions, pipeline design, and management strategies that agreed with the well-known multi-phase flow simulator in the O&G industry.

The thermodynamic models applied to predict hydrate formation curves and fluid characterization were suitable for the proposed case studies. However, the results suggested that the three-phase flash underestimated the liquid fractions by around 15%. There is a need to improve the time efficiency in generating the table with equilibrium data to make this tool competitive with others available in the literature.

Despite this, the thermodynamic contributions of this work open the possibility of studying fluids with compositions similar to those found in oil fields, a limitation prevalent in most previous works. Furthermore, improving the three-phase flash for liquids allows for the characterization of fluids with larger water cut, providing an opportunity to study the influence of these conditions on hydrate formation using the kinetic model.

The Drift-Flux Model enabled the observation of hydrate formation and dissociation in the riser section. The behavior of hydrate growth, aggregation, and dissociation corresponded to observations in the literature, with the addition of mass transfer due to vaporization, a factor often neglected.

This study also successfully combined thermodynamic and kinetic aspects, which are typically studied separately due to their complexity, and achieved results in line with those obtained from commercial software.

Future work could incorporate the slip velocity between hydrate-liquid phases and model heterogeneous dispersion to evaluate its effects on pressure drop. Furthermore, the kinetic model could be extended to include other mechanisms involved in hydrate formation in oil-dominated systems, as outlined in the literature.

Appendix A

vdW-P model parameters

Table A.1: A_{ki} and B_{ki} parameters from MUNCK *et al.* (1988) for Eq. (2.5).

Component	Structure I				Structure II			
	Small cavity		Large cavity		Small cavity		Large cavity	
	$A_{ki} \times 10^{-8}$	$B_{ki} \times 10^3$	$A_{ki} \times 10^{-8}$	$B_{ki} \times 10^3$	$A_{ki} \times 10^{-8}$	$B_{ki} \times 10^3$	$A_{ki} \times 10^{-8}$	$B_{ki} \times 10^3$
N ₂	1.617	2.905	6.078	2.431	0.1742	3.082	18.00	1.728
CO ₂	0.2474	3.410	42.46	2.813	0.0845	3.615	851.0	2.025
H ₂ S	0.0250	4.568	16.34	3.737	0.0298	4.878	87.2	2.633
CH ₄	0.7228	3.187	23.35	2.653	0.2207	3.453	100.0	1.916
C ₂ H ₆	0	0	3.039	3.861	0	0	240.0	2.967
C ₃ H ₈	0	0	0	0	0	0	5.455	4.638
i-C ₄ H ₁₀	0	0	0	0	0	0	189.3	3.80
n-C ₄ H ₁₀	0	0	0	0	0	0	30.51	3.699

A_{ij} has dimension of $[K/Pa]$ and B_{ij} of $[K]$.

Table A.2: Reference values of a physical constant from MUNCK *et al.* (1988) to Eq. (2.6).

Property	Unit	Structure I	Structure II
$u^{liq,0}$	J/mol	1.264	883
$\Delta h^{liq,0}$	J/mol	-4.858	-5.201
$\Delta h^{ice,0}$	J/mol	1.151	808
$\Delta V^{liq,0}$	cm^3/mol	4.6	5.0
$\Delta V^{ice,0}$	cm^3/mol	3.0	3.4
$\Delta c_p^{liq,0}$	$J/mol/K$	39.16	39.16

Appendix B

Complementary equations

B.1 Frictional loss

$$F_{mv} = \phi_v^2 \left(\frac{dP}{dx} \right)_{f(v)} \quad (\text{B.1})$$

$$\phi_v^2 = \chi^2 + C\chi + 1 \quad (\text{B.2})$$

$$\chi^2 = \frac{\left(\frac{dP}{dx} \right)_{f(l)}}{\left(\frac{dP}{dx} \right)_{f(v)}} \quad (\text{B.3})$$

$$C = -2 + (28 - 0.3\sqrt{G}) \exp \left[-\frac{(\log_{10}(\rho_v \rho_l^{-1} \mu_l^{0.2} \mu_v^{-0.2} + 2.5))^2}{2.4 - 10^{-4}G} \right] \quad (\text{B.4})$$

$$G = \sum G_k = \sum \alpha_k \rho_k U_k \quad (\text{B.5})$$

$$\left(\frac{dP}{dx} \right)_{f(l)} = \frac{f_l m_l^2}{2D \rho_l A^2} \quad (\text{B.6})$$

$$\left(\frac{dP}{dx} \right)_{f(v)} = \frac{f_v m_v^2}{2D \rho_v A^2} \quad (\text{B.7})$$

$$m_l = (1 - \alpha_v) \rho_l U_l A \quad (\text{B.8})$$

$$m_v = (1 - \alpha_v) \rho_v U_v A \quad (\text{B.9})$$

$$Re_l = \frac{m_l D}{\mu_l A} \quad (\text{B.10})$$

$$f_l = \begin{cases} \frac{64}{Re_l}, & Re_l \leq 2100 \\ \frac{1}{f_{nl}^2}, & Re_l > 2100 \end{cases} \quad (\text{B.11})$$

$$f_{nl} = -2 \log_{10} \left\{ \frac{e}{3.7065D} - \frac{5.0452}{Re_l} \log_{10} \left[\frac{(e/D)^{1.1098}}{2.8257} + \left(\frac{7.149}{Re_l} \right)^{0.8981} \right] \right\} \quad (\text{B.12})$$

$$Re_v = \frac{m_v D}{\mu_v A} \quad (\text{B.13})$$

$$f_v = \begin{cases} \frac{64}{Re_v}, & Re_v \leq 2100 \\ \frac{1}{f_{nv}^2}, & Re_v > 2100 \end{cases} \quad (\text{B.14})$$

$$f_{nv} = -2 \log_{10} \left\{ \frac{e}{3.7065D} - \frac{5.0452}{Re_v} \log_{10} \left[\frac{(e/D)^{1.1098}}{2.8257} + \left(\frac{7.149}{Re_v} \right)^{0.8981} \right] \right\} \quad (\text{B.15})$$

B.2 Phase velocities

$$U_v = U_m + \frac{\rho_l}{\rho_m} \hat{v}_v^{dft} \quad (\text{B.16})$$

$$U_l = U_m - \frac{\alpha_v \rho_v}{(1 - \alpha_v) \rho_m} \hat{v}_v^{dft} \quad (\text{B.17})$$

Appendix C

Modified fluid complementary data

Table C.1: Binary interaction parameters obtained from *Multiflash*TM library.

	CH ₄	C ₃ H ₁₂	i-C ₄ H ₁₆	n-C ₄ H ₁₆	i-C ₅ H ₂₀	n-C ₅ H ₂₀	C ₆	C ₇	C ₈	C ₉	C ₁₀	C ₁₁ +	H ₂ O
CH ₄	0	0.0204	0.0247	0.0247	0.028	0.0286	0.0307	0.0337	0.0361	0.0386	0.0410	0.0512	0.5000
C ₃ H ₁₂		0	0	0	0.0272	0.0272	0.0293	0.0322	0.0347	0.0372	0.0396	0.0498	0.5140
i-C ₄ H ₁₆			0	0	0	0	0.0265	0.0295	0.0319	0.0344	0.0369	0.0470	0.5149
n-C ₄ H ₁₆				0	0	0	0.0265	0.0295	0.0319	0.0344	0.0369	0.0470	0.5152
i-C ₅ H ₂₀					0	0	0	0.0145	0.0169	0.0194	0.0219	0.0320	0.5156
n-C ₅ H ₂₀						0	0	0.0145	0.0169	0.0194	0.0219	0.0320	0.5160
C ₆							0	0	0	0	0	0	0.5164
C ₇								0	0	0	0	0	0.5167
C ₈									0	0	0	0	0.5170
C ₉										0	0	0	0.5173
C ₁₀											0	0	0.5175
C ₁₁ +												0	0.5184
H ₂ O													0

References

- AL-OTAIBI, F., CLARKE, M. A., MAINI, B., BISHNOI, P. R., 2010, “Formation kinetics of structures I clathrates of methane and ethane using an in situ particle analyzer”, *Energy Fuels*, v. 24, pp. 5012–5022.
- ANDRADE, M. H. C., 1991, *Equilíbrio líquido-líquido-vapor de misturas ternárias: algoritmo de cálculo e aspectos termodinâmicos*. Tese de Doutorado, UNICAMP.
- ANKLAN, M. R., FIROOZABADI, A., 2004, “Driving force and composition for multicomponent gas hydrate nucleation from supersaturated aqueous solutions”, *Journal of Chemical Physics*, v. 121, pp. 11867–11875.
- ANP, 2021. “ANP - National Agency of Petroleum, Natural Gas and Biofuels”. Accessed on March 20, 2023. <https://www.gov.br/anp/pt-br>.
- API, 1997, *Technical Data Book - Petroleum Refining*. 6 ed. Washington, United States, American Petroleum Institute.
- ARJMANDI, M., TOHIDI, B., DANESH, A., TODD, A. C., 2005, “Is subcooling the right driving force for testing low-dosage hydrate inhibitors?” *Chemical Engineering Science*, v. 60, pp. 1313–1321.
- BALLARD, A. L., SLOAN, E. D., 2004a, “The next generation of hydrate prediction Part III. Gibbs energy minimization formalism”, *Fluid Phase Equilibria*, v. 218, pp. 15–31.
- BALLARD, L., SLOAN, E., 2004b, “The next generation of hydrate prediction IV: A comparison of available hydrate prediction programs”, *Fluid Phase Equilibria*, v. 216, n. 2, pp. 257–270.
- BASSANI, C. L., 2017, *Modelagem do escoamento trifásico sólido-líquido-gás em golfegas acoplado transferência de calor e massa com a formação de hidratos*. Tese de Doutorado, UTFPR.

- BASSANI, C. L., MELCHUNA, A. M., CAMEIRAO, A., HERRI, J., MORALES, R. E. M., SUM, A. K., 2019, “A multiscale approach for gas hydrates considering structure, agglomeration, and transportability under multiphase flow conditions: I. Phenomenological Model”, *Industrial & Engineering Chemistry Research*, v. 58, pp. 14446–14461.
- BASSANI, C. L., SUM, A. K., HERRI, J., MORALES, R. E. M., CAMEIRAO, A., 2020, “A multiscale approach for gas hydrates considering structure, agglomeration, and transportability under multiphase flow conditions: II. Growth kinetic model”, *Industrial & Engineering Chemistry Research*, v. 59, pp. 2123–2144.
- BHAGWAT, S. M., GHAJAR, A. J., 2014, “A flow pattern independent drift flux model based void fraction correlation for a wide range of gas–liquid two phase flow”, *International Journal of Multiphase Flow*, v. 59, pp. 186–205.
- BOMBA, J., CHIN, D., KAK, A., MENG, W., 2018, “Flow assurance engineering in deepwater offshore - past, present, and future”. In: *Proceedings of the Annual Offshore Technology Conference*, v. 5, pp. 3608–3634.
- BOXALL, J., DAVIES, S., KOH, C. A., SLOAN, E. D., 2009, “Predicting when and where hydrate plugs form in oil-dominated flowlines”. In: *SPE Projects, Facilities and Construction*, v. 4, pp. 80–86.
- BOXALL, J. A., KOH, C. A., SLOAN, E. D., SUM, A. K., WU, D. T., 2012, “Droplet Size Scaling of Water-in-Oil Emulsions under Turbulent Flow”, *Langmuir*, v. 28, n. 1, pp. 104–110.
- CAMARGO, R., PALERMO, T., 2002, “Rheological properties of hydrate suspensions in an asphaltenic crude oil”. In: *Proceedings of the 4th International Conference on Gas Hydrates*, v. 1, pp. 880–885.
- CARDOSO, C. A. B. R., GONÇALVES, M. A. L., CAMARGO, R. M. T., 2015, “Design options for avoiding hydrates in deep offshore production”, *Journal of Chemical & Engineering Data*, v. 60, n. 2, pp. 330–335.
- CARROL, J., 2009, *Natural Gas Hydrates: A Guide for Engineers*. Gulf Professional Publishing.
- CHEN, N. H., 1979, “An explicit equation for friction factor in pipe”, *Industrial & Engineering Chemistry Fundamentals*, v. 18, n. 3, pp. 296–297.
- CHIN, H., HSIEH, M., CHEN, Y., CHEN, P., LIN, S., CHEN, L., 2013, “Prediction of phase equilibrium for gas hydrate in the presence of organic inhibitors and

- electrolytes by using an explicit pressure-dependent Langmuir adsorption constant in the van der Waals–Platteeuw model”, *The Journal of Chemical Thermodynamics*, v. 66, pp. 34–43.
- CLARKE, M. A., BISHNOI, P. R., 2005, “Determination of the intrinsic kinetic of CO₂ gas hydrate formation in situ particle size analysis”, *Chemical Engineering Science*, v. 60, pp. 695–709.
- CUI, J., SUN, Z., WANG, X., YU, B., LENG, S., CHEN, G. AND SUN, C., 2019, “Fundamental mechanisms and phenomena of clathrate hydrate nucleation”, *Chinese Journal of Chemical Engineering*, v. 27, pp. 2014–2025.
- DUAN, X., SHI, B., WANG, J., et al., 2021, “Simulation of the hydrate blockage process in a water-dominated system via the CFD-DEM method”, *Journal of Natural Gas Science and Engineering*, v. 96, pp. 104241.
- ENGLEZOS, P., KALOGERAKIS, N., DHOLABHAI, P. D., BISHNOI, P. R., 1987a, “Kinetic of formation of methane and ethane gas hydrates”, *Chemical Engineering Science*, v. 42, pp. 2647–2658.
- ENGLEZOS, P., KALOGERAKIS, N., DHOLABHAI, P. D., BISHNOI, P. R., 1987b, “Kinetic of gas hydrate formation from mixtures of methane and ethane”, *Chemical Engineering Science*, v. 42, pp. 2699–2666.
- FERREIRA, G. G. S., 2018, *Desenvolvimento de metodologias para simulação de escoamento multifásicos com a formação de hidratos*. Tese de Doutorado, COPPEUFRJ.
- GONG, J., SHI, B., ZHAO, J., 2010, “Natural gas hydrate shell model in gas-slurry pipeline flow”, *Journal of Natural Gas Chemistry*, v. 19, n. 3, pp. 261–266.
- GUEDES, T. A. L., 2015, *Modelagem do escoamento em linhas de produção Offshore com garantia de escoamento*. Tese de Mestrado, COPPE/UFRJ.
- GUEDES, T. A. L., 2023, *Análise de garantia de escoamento em linhas de produção offshore: modelagem matemática e gerenciamento das condições de formação de hidratos*. Tese de Doutorado, COPPE/UFRJ.
- GUEDES, T. A. L., R.G.D., SECCHI, MELO, P. A., TEIXEIRA, R., 2020, “Pipeline design with flow assurance constraints in offshore production lines”, *Brazilian Journal of Chemical Engineering*, v. 37, pp. 555.
- GUPTA, A. K., BISHNOI, P. R., KALOGERAKIS, N., 1991, “A method for the simultaneous phase equilibria and stability calculations for multiphase reacting and non-reacting systems”, *Fluid Phase Equilibria*, v. 63, pp. 65–89.

- GÓES, M. R. R., GUEDES, T. A., TEIXEIRA, R. G., MELO, P. A., TAVARES, F. W., SECCHI, A. R., 2023, “Multiphase flow simulation in offshore pipelines: An accurate and fast algorithm applied to real-field data”, *Chemical Engineering Science*, v. 268, pp. 118438.
- KASHCHIEV, D., FIROOZABADI, A., 2002, “Driving force for crystallization of gas hydrates”, *Journal of Crystal Growth*, v. 243, pp. 220–230.
- KE, W., SVARTAAS, T. M., CHEN, D., 2019, “A review of gas hydrates nucleation theories and growth models”, *Journal of Natural Gas Science and Engineering*, v. 61, pp. 169–196.
- KHAN, M. N., WARRIER, P., PETERS, C. J., KOH, C. A., 2018, “Advancements in hydrate phase equilibria and modeling of gas hydrates systems”, *Fluid Phase Equilibria*, v. 463, pp. 48–61.
- KINNARI, K., HUNDSEID, J., LI, X., ASKVIK, K. M., 2014, “Hydrate management in practice”, *Journal of the American Chemical Society*, v. 60, pp. 437–446.
- KLAUDA, J. B., SANDLER, S. I., 2000, “A fugacity model for gas hydrate phase equilibria”, *Industrial & Engineering Chemistry Research*, v. 39, n. 9, pp. 3377–3386.
- KOH, C. A., SLOAN, E. D., SUM, A. K., 2011a, *Natural Gas Hydrates in Flow Assurance*. 1 ed. , Gulf Professional Publishing is an imprint of Elsevier.
- KOH, C. A., SLOAN, E. D., SUM, A. K., T., W. D., 2011b, “Fundamentals and applications of gas hydrates”, *The Annual Review of Chemical and Biomolecular Engineering*, v. 2, pp. 237–257.
- LEKVAM, K., RUOFF, P., 1993, “A reaction kinetic mechanism for methane hydrate formation in liquid water”, *Journal of the American Chemical Society*, v. 115, pp. 8565–8569.
- LI, S., LI, Y., YANG, L., HAN, Y., JIANG, Z., 2021, “Prediction of equilibrium conditions for gas hydrates in the organic inhibitor aqueous solutions using a thermodynamic consistency-based model”, *Fluid Phase Equilibria*, v. 544-545, pp. 113118.
- LOHRENZ, J., BRAY, B. G., CLARK, C. R., 1964, “Calculating viscosities of reservoir fluids from their compositions”, *Journal of Petroleum Technology*, v. 16, n. 10 (10), pp. 1171–1176.
- MAJID, A. A. A., WU, D., KOH, C. A., 2018, “A perspective on rheological studies of gas hydrate slurry properties”, *Engineering*, v. 4, n. 3, pp. 321–329.

- MAKOGON, Y. F., 2010, “Natural gas hydrate - a promising source of energy”, *Journal of Natural Gas Science and Engineering*, v. 2, pp. 49–59.
- MEDEIROS, F. A., SEGTOVICH, I. S. V., TAVARES, F. W., SUM, A. K., 2020, “Sixty years of the van der Waals and Platteeuw Model for clathrate Hydrates – A critical review from its statistical thermodynamic basis to its extension and applications”, *Chemical Reviews*, v. 120, pp. 13349–13381.
- MEKALA, P., SANGWAI, J., 2014, “Prediction of phase equilibrium of clathrate hydrate of multicomponent natural gases containing CO_2 and H_2S ”, *Journal of Petroleum Science and Engineering*, v. 116, pp. 81–89.
- MUNCK, J., SKJOLD-JØRGENSEN, S., RASMUSSEN, P., 1988, “Computations of the formation of gas hydrates”, *Chemical Engineering Science*, v. 43, n. 10, pp. 2661–2672.
- NELSON, P. A., 1987, “Rapid phase determination in multiple-phase flash calculations”, *Computational Chemical Engineering*, v. 11, pp. 581–591.
- PARRISH, W. R., PRAUSNITZ, J. M., 1972, “Dissociation Pressures of Gas Hydrates Formed by Gas Mixtures”, *Industrial & Engineering Chemistry Process Design and Development*, v. 11, n. 1, pp. 26–35.
- PLATTEEUW, J. C., VAN DER WAALS, J. H., 1958, “Thermodynamic properties of gas hydrates”, *Molecular Physics*, v. 1, n. 1, pp. 91–96.
- RAIZI, M. R., 2005, *Characterization and Properties of Petroleum Fractions*. ASTM.
- RAO, I., 2013, *Multiphase flow modeling and deposition of hydrates in oil and gas pipelines*. Tese de Doutorado, Colorado School of Mines.
- SAKURAI, S., HOSKIN, B., CHOI, J., MAY, E. F., AMAN, M., NORRIS, B. W. E., 2022, “Dynamics of methane hydrate particles in water-dominant systems during transient flow”, *Fuel*, v. 324, pp. 124772.
- SANZ, E., VEGA, C., ESPINOSA, J. R., CABALLERO-BERNAL, R., ABASCAL, J. L. F., VALERIANI, C., 2013, “Homogeneous ice nucleation at moderate supercooling from molecular simulation”, *Journal of the American Chemical Society*, v. 135, pp. 15008–15017.
- SECCHI, A. R., 2012. “Differential-Algebraic System Solver in C”. Disponível em: <<https://www.ufrgs.br/dequi-app/enqlib/numeric/>>.

- SEGTOVICH, I. S. V., BARRETO, A. G., TAVARES, F. W., 2016, “Simultaneous multi-phase flash and stability analysis calculations including hydrates”, *Fluid Phase Equilibria*, v. 413, pp. 196–208.
- SHI, B., GONG, J., SU, C., ZHAO, J., DING, Y., CHEN, G., 2011, “An inward and outward natural gas hydrates growth shell model considering intrinsic kinetics, mass and heat transfer”, *Chemical Engineering Journal*, v. 171, n. 3, pp. 1308–1316.
- SJÖBLOM, J., ØVREVOLL, B., JENTOFT, G., et al., 2010, “Investigation of the hydrate plugging and non-plugging properties of oils”, *Journal of Dispersion Science and Technology*, v. 31 (07), pp. 1100–1119.
- SLOAN, E. D., KOH, C. A., 2008, *Clathrate Hydrates of Natural Gas*. 3 ed. , CRC Press.
- TEIXEIRA, R. G. D., 2016, *Abordagem algébrico-diferencial na simulação unidimensional do escoamento bifásico em dutos*. Tese de Doutorado, COPPE/UFRJ.
- TEIXEIRA, R., SECCHI, A. R., BISCAIA, E. C., 2015, “Two-phase flow in pipes: numerical improvements and qualitative analysis for a refining process”, *Oil Gas Sci. Technol. - Rev. IFP Energies nouvelles*, v. 70, n. 3, pp. 497.
- TURNER, D., BOXALL, J., YANG, D., et al., 2005, “Development of a hydrate kinetic model and its incorporation into the OLGA2000[®] transient multi-phase flow simulator”. In: *Proceedings of the 5th International Conference on Gas Hydrates*.
- VYSNIAUSKAS, A., BISHNOI, P. R., 1983, “A kinetic study of methane hydrate formation”, *Chemical Engineering Science*, v. 38, pp. 1061–1072.
- VYSNIAUSKAS, A., BISHNOI, P. R., 1985, “Kinetics of ethane hydrate formation”, *Chemical Engineering Science*, v. 40, pp. 299–303.
- WANG, L., CUI, J., SUN, C., MA, Q., FAN, S., WANG, X., CHEN, G., 2021, “Review on the applications and modifications of the Chen–Guo Model for hydrate formation and dissociation”, *Energy & Fuels*, v. 35, n. 4, pp. 2936–2964.
- WANG, Y., KOH, C. A., DAPENA, J. A., ZERPA, L. E., 2018a, “A transient simulation model to predict formation rate in both oil- and water-dominated systems in pipelines”, *Journal of Natural Gas Science and Engineering*, v. 58, pp. 126–134.

- WANG, Z., ZHANG, J., CHEN, L., ZHAO, Y., FU, W., YU, J., SUN, B., 2018b, “Modeling of hydrate layer growth in horizontal gas-dominated pipelines with free water”, *Journal of Natural Gas Science and Engineering*, v. 50, pp. 364–373.
- WHITSON, C. H., BRULE, M. R., 2000, *Phase Behavior*. Society of Petroleum Engineers.
- ZARENEZHAD, B., ZIAEE, M., 2013, “Accurate prediction of H₂S and CO₂ containing sour gas hydrates formation conditions considering hydrolytic and hydrogen bonding association effects”, *Fluid Phase Equilibria*, v. 356, pp. 321–328.
- ZERPA, L. E., SLOAN, E. D., SUM, A. K., KOH, C. A., 2012, “Overview of CSMHyK: a transient hydrate formation model”, *Journal of Petroleum Science and Engineering*, v. 98-99, pp. 122–129.
- ZERPA, L., 2013, *A practical model to predict gas hydrate formation, dissociation and transportability in oil and gas flowlines*. Tese de Doutorado, Colorado School of Mines.
- ZHANG, J., LI, C., SHI, L., XIA, X., YANG, F., SUN, G., 2022, “The formation and aggregation of hydrate in W/O emulsion containing different compositions: A review”, *Chemical Engineering Journal*, v. 445.